

# Compton Cameras for Nuclear Medical Imaging

W. L. ROGERS,\* N. H. CLINTHORNE,\* and A. BOLOZDYNIA†

\*Division of Nuclear Medicine, University of Michigan, Ann Arbor, Michigan

†Constellation Technology Corp., Largo, Florida

- I. Introduction
- II. Factors Governing System Performance
- III. Analytical Prediction of System Performance
- IV. Image Reconstruction
- V. Hardware and Experimental Results
- VI. Future Prospects for Compton Imaging
- VII. Discussion and Summary

## I. INTRODUCTION

### A. Method and Motivation

At present, virtually all single-photon imaging in nuclear medicine relies on mechanical apertures of some sort to form projection images of the spatial distribution of gamma-ray-emitting radiolabeled compounds. The simplest aperture is a pinhole or pinhole array in a lead or tungsten sheet used to form pinhole images on a gamma camera. Gunter (Chapter 8) describes a variety of other apertures including parallel and converging-channel collimators. With the exception of coded aperture techniques, all these methods exhibit a limiting detection sensitivity that is inversely proportional to the spatial resolution. For single-photon emission computed tomography (SPECT) imaging, sensitivity is inversely proportional to the number of resolution elements in the object projection, that is, the reciprocal of the projection-space bandwidth (Rogers and

Ackermann, 1992). Doubling either the object size or collimator resolution decreases sensitivity by a factor of four. This assumes that multiple projections of the object do not overlap, as they do for coded apertures. Performance of mechanical apertures also suffers with increasing gamma-ray energy. They perform well for  $^{99m}\text{Tc}$  at 140 keV, but to image  $^{131}\text{I}$ , septal thickness must be substantially increased to reduce gamma-ray penetration with a sacrifice in sensitivity and increase in weight. Despite the thicker septa, there remains considerable penetration background both from the principal 360-keV gamma rays and from the group of higher-energy emissions that extend to 723 keV and comprise about 8% of the emitted photons.

In contrast, the Compton camera provides information about the incoming photon direction electronically without restricting the detection solid angle in the way that mechanical apertures do. The method is illustrated in Figure 1.

The incoming gamma-ray Compton-scatters from an electron in the position-sensitive first detector and is subsequently absorbed by the second position-sensitive detector. The recorded data consist of the interaction coordinates,  $X_1, Y_1, X_2, Y_2$  and deposited energies for the two events that occur essentially simultaneously in the first and second detectors. The sum of the two energies provides an estimate of the incoming gamma-ray energy, and the energy deposited in the first detector,  $E_1$ , gives an estimate of the scattering angle,  $\hat{\Phi}$ . However, without knowledge of the recoil electron momentum vector, the azimuthal angle is undetermined and the actual point source location is only constrained to lie on

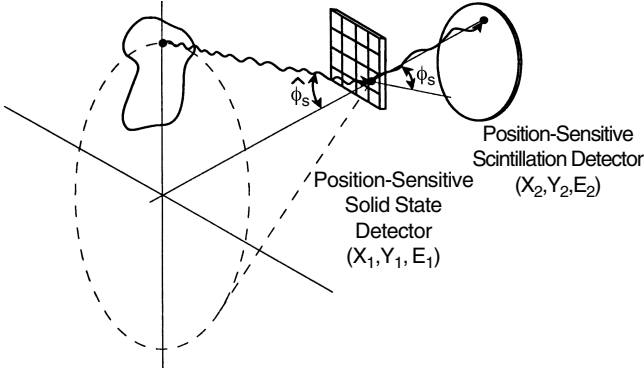


FIGURE 1 Principle of the Compton camera.

a conical shell with angular thickness  $\hat{\Phi}$ . This angular uncertainty is related to uncertainty in the recoil electron energy measurement and the electron's initial momentum. There is also uncertainty in the determination of the cone axis introduced by uncertainty in the estimates of the interaction points in the first and second detectors.

If the struck electron is assumed to be at rest, the relation between the incoming gamma-ray energy,  $E_{\gamma 0}$ ,  $E_1$ , and  $\hat{\Phi}$  is given by:

$$\cos \hat{\Phi} = 1 - \frac{E_1}{\alpha E_2} = 1 - \frac{E_1}{\alpha(E_{\gamma 0} - E_1)} \text{ where } \alpha = \frac{E_{\gamma 0}}{m_0 c^2} \quad (1)$$

Because the detection efficiency depends on the joint probability of an interaction in detector 1 followed by an interaction in detector 2, sensitivity depends on the size, type, and geometry of the two detectors. Angular resolution, on the other hand, depends on the noise characteristics of detector 1 and spatial resolution of the two detectors. We see that the direct relationship between spatial resolution and sensitivity that is the property of mechanical collimation does not exist for Compton cameras. Further, if the principal uncertainty in estimating  $\Phi$  is the uncertainty in  $E_1$  due to additive detector noise, we see from Eq. (2) that angular resolution improves with increasing gamma-ray energy,  $E_{\gamma 0}$ .

$$d\Phi = \frac{m_0 c^2}{\sin \Phi (E_{\gamma 0} - E_1)^2} dE_1 \quad (2)$$

These topics will be pursued more rigorously later, but from these two observations it is evident why Compton cameras have such an attraction for researchers in nuclear medicine and other fields in which gamma-ray imaging is a focus.

In this chapter we summarize the present status of Compton imaging in the nuclear medicine application. Following a brief history of the technique, we review the physical factors that influence system performance. In Section III, we discuss analytical predictions of Compton camera performance for quantification and detection tasks in comparison to collimated cameras and also show calculated values of detection sensitivity for two different system geometries.

Methods of image reconstruction are discussed in Section IV, and prototype hardware implementations are described in Section V. We conclude with a discussion of future possibilities for Compton imaging in nuclear medicine and outstanding questions.

## B. Brief History

The Compton imaging technique was proposed independently by Pinkau (1966) and White (1968) for imaging solar neutrons. Pinkau employed spark chambers, and White described a method using scintillation detectors.

Schönfelder *et al.* (1973) described the application to gamma-ray astronomy, and over the next several years several groups flew Compton imagers on balloon flights. COMPTEL was described in 1984 (Schönfelder *et al.*, 1984), and in 1992 the first satellite measurements from the Gamma-Ray Observatory made by COMPTEL were reported by Winkler *et al.* (1992). A number of groups are developing different versions of a second-generation Compton telescope. Most of these introduce tracking of the recoil electron as a means to reduce the conical ambiguity to a limited arc of the conical surface. MEGA is under development by the group at the Max Planck Institute for Extraterrestrial Physics in Munich (Schopper *et al.*, 2000), TIGRE is under development at the University of California, Riverside (O'Neill *et al.*, 1996; Bhattacharya *et al.*, 1999), and similar work is under way at the Naval Research Laboratory (Kroeger *et al.*, 1999).<sup>1</sup>

The possible application of the Compton imaging method to nuclear medicine was first described by Todd and Nightingale in 1974 (Todd, 1975; Todd *et al.*, 1974; Everett *et al.*, 1976). Singh and his colleagues published a number of seminal papers beginning in 1981 that described analytical and experimental results for a Compton camera composed of a pixelated germanium first detector and a standard Anger camera second detector (Singh, 1983; Singh and Doria, 1981, 1983, 1985; Singh *et al.*, 1986, 1988; Doria and Singh, 1982; Hebert *et al.*, 1987, 1988, 1990; Brechner and Singh, 1988, 1990). Their system geometry corresponded closely to that illustrated in Figure 1. The Compton scattering detector was designed and fabricated by R. H. Pehl and his colleagues at Lawrence Berkeley Laboratory and exhibited an energy resolution of 850 eV FWHM (Pehl *et al.*, 1985). This detector was subsequently lent to the University of Michigan by Singh to investigate a ring geometry Compton camera and evaluate its potential for imaging radioactive spills, monitoring nuclear waste, and medical imaging. The results of this work have been reported by Martin and Gormley (Martin, 1994; Martin *et al.*, 1993, 1994; Gormley, 1997; Gormley *et al.*, 1997).

<sup>1</sup>For additional information, see <http://www.gamma.mpe-garching.mpg.de/MEGA/mega.html>, <http://osse-www.nrl.navy.mil/>, and <http://tigre.ucr.edu/>.

In the remainder of this chapter we summarize ongoing research at the University of Michigan and elsewhere relating to the application of Compton cameras to nuclear medical imaging.

## II. FACTORS GOVERNING SYSTEM PERFORMANCE

The important attributes of an imaging system for nuclear medicine are spatial resolution and detection sensitivity for gamma rays in the energy range extending from 70 keV for  $^{201}\text{TI}$  to 511 keV, the positron annihilation energy. The factors governing resolution can be grouped into geometric effects, including the intrinsic resolution of the first and second detectors, electronic effects principally related to noise in the scattering detector and its readout electronics, and the physics of Compton scattering. This section examines the issue of spatial resolution. Sensitivity issues are discussed in later sections.

### A. Geometric Effects

To rapidly evaluate various detector candidates and system geometries, it is necessary to have an approximate analytical model of system resolution. The propagation of the effects of first- and second-detector spatial resolution has been addressed by several authors, each with respect to their particular system design (Singh, 1983; Martin, 1994; Martin *et al.*, 1993; Gormley, 1997; LeBlanc *et al.*, 1998). More recently, Ordóñez *et al.* (1999) have described a more generalized approach that can be used to predict geometric resolution for the planar geometry of Figure 1, the cylindrical geometry of C-SPRINT, and the conical geometry of the ring Compton camera. Results can be obtained for both isotropic and anisotropic detector response functions.

The independent effects of scatter-detector and absorption-detector resolution are illustrated in Figure 2.  $R_a$  represents the resolution of the absorption detector, which introduces uncertainty in the angular orientation of the backprojected cone. The first-detector resolution,  $R_s$ , causes uncertainty both in the position of the vertex and orientation of the cone. These effects are usually combined in quadrature under the assumption that they have Gaussian distributions.

The expression derived by Ordóñez for cylindrical geometry was evaluated for an on-axis point source 10 cm from an on-axis scatter detector with isotropic 1-mm resolution and a long cylindrical second detector with 3-mm resolution on the surface of the cylinder (Hua, 2000). Results are shown in Figure 3 for two values of second-detector radius and two values of depth resolution. The effects of depth of interaction uncertainty in the second detector are very prominent in the neighborhood of 45° scattering for this geometry. Because the absorption detector is generally

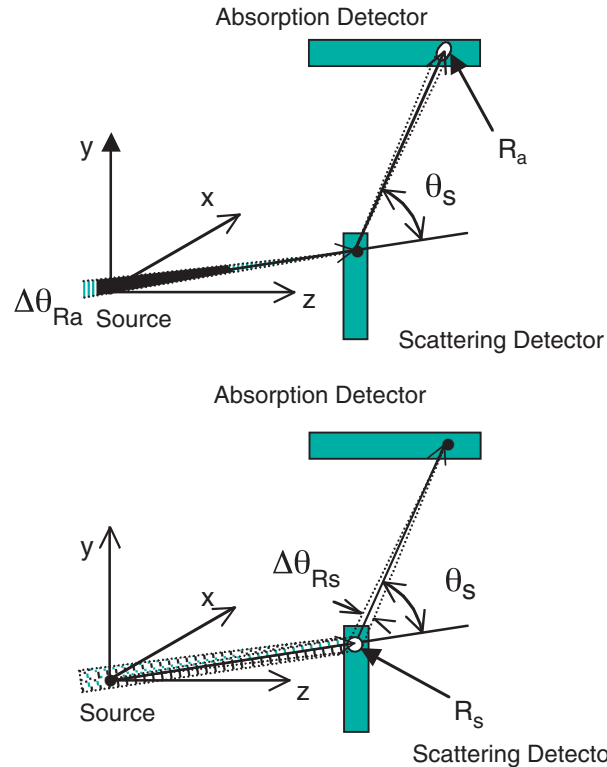


FIGURE 2 Illustration of individual scattering and absorption detector spatial resolution effects on the backprojected ray assuming no uncertainty in the scattering angle  $\theta_s$ .

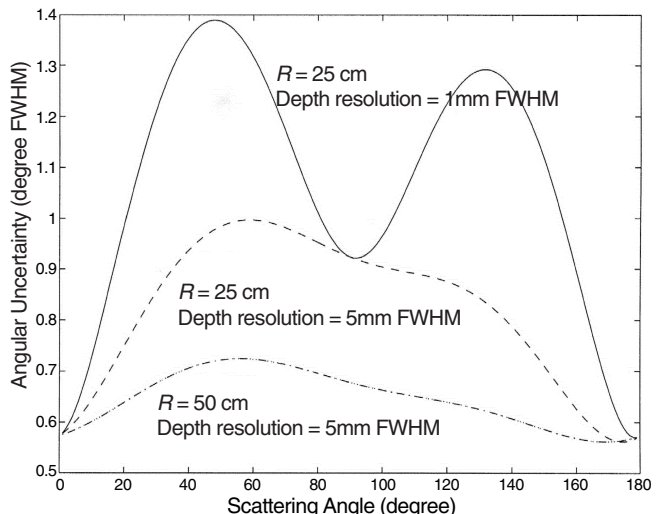


FIGURE 3 Angular uncertainty due to 3D detector resolution and system geometry for a small on-axis first detector with isotropic resolution of 1 mm and a long cylindrical second detector with 3-mm resolution on the cylindrical surface and depth resolution of 5 and 10 mm full width at half maximum (FWHM). Results are illustrated for cylindrical radii of 25 and 50 cm. (From Hua, 2000, © 2000 C-H Hua).

a thick detector, depth of interaction uncertainty will play an important role as gamma-ray energy increases and, as we see later, can dominate other effects. Increasing the distance

between first and second detectors improves angular resolution in almost a linear fashion, as might be expected from Figure 2, but maintaining the same solid angle requires that the second-detector area increase as the square of the distance, and this has important cost implications.

### B. Statistical and Electronic Effects

The ability to estimate the scattering angle from Eq. (1) depends strongly on the noise in the measurement of  $E_1$  as shown in Eq. (2). The statistical noise component is related to the uncertainty in the number of electron–hole pairs produced by the recoil electron and subsequently collected. This imposes a physical limit on energy resolution. If the number of carriers,  $N$ , is proportional to the deposited energy and described by a Poisson process, then the energy resolution is given by

$$RES \equiv \frac{FWHM}{E} = \frac{2.35k\sqrt{N}}{kN} = \frac{2.35}{\sqrt{N}} \quad (3)$$

Here,  $k$  is the proportionality constant and it is assumed that  $N$  is sufficiently large that the Poisson distribution is approximately Gaussian. In fact, the process is not Poisson, and if all the deposited energy were converted to charge carriers, the limiting energy resolution would approach zero. The departure from Poisson statistics depends in a complex fashion on the sequence of interactions by which initial recoil electron energy is split up between production of electron–hole pairs and other energy-loss mechanisms. The ratio of observed variance in  $N$  to that predicted by the Poisson model is termed the Fano factor. Measurements of the Fano factor for germanium detectors at 77 K ranges from 0.057 to 0.129 and for silicon detectors from 0.084 to 0.143 (Sansen and Chang, 1990), so solid-state detector performance is substantially better than one would predict from a Poisson model. For silicon, at 77 K, it requires 3.76 eV to create an electron–hole pair as opposed to 2.96 eV for germanium. A Poisson model predicts 14.4% and 12.8% full width at half maximum (FWHM) energy resolution for 1-keV gamma rays for silicon and germanium, respectively. Using the lowest measured Fano factors yields 1.2% and 0.73% FWHM energy resolution. At 140 keV, the limiting energy resolution for silicon is approximately 230 eV. As we see below, at the energies of interest statistical uncertainties are overwhelmed by electronic noise.

Electronic noise in sensor readout is usually expressed as the equivalent noise charge (ENC) at the input of a charge-sensitive preamplifier. The input stage in CMOS charge-sensitive devices is a field effect transistor (FET), and the noise is generally separated into series and parallel components. The series noise consists of a temperature-dependent channel noise and 1/f noise. The equivalent noise charge for the series component depends on the integration time constant and is proportional to the sum of the internal

and external capacitance. As a specific example, consider the VA32C, a CMOS LSI preamplifier manufactured by Integrated Detector Electronics<sup>2</sup>:

$$\sqrt{\langle q_{\text{series}}^2 \rangle} = 45e^- + 12e^- / pf_{\text{ext}} \quad (4)$$

The parallel equivalent noise charge is determined by the detector leakage current, the bias and feedback resistors, and the integration time constant. Again, for the VA32C with a 2  $\mu$ s peaking time, this is approximately:

$$\langle q_{\text{parallel}}^2 \rangle = \langle q_{\text{leakage}}^2 \rangle + \langle q_{\text{res}}^2 \rangle \approx 150^2 I_D + 1070^2 \frac{1}{R(M\Omega)} \quad (5)$$

Where  $I_D$  is the detector leakage current in nanoamps and  $R$  is the sum of the bias and feedback resistances in parallel. To see the relative importance of these various components, consider a pixelated silicon detector designed to have a 1.4-mm spatial resolution with a possible wafer thickness from .3 to 1.5 mm. The capacitance for 1 pixel including the traces and wire bond will be 3–4 pf. Most of the contribution comes from the traces and wire bond. Leakage current at room temperature can vary widely from manufacturer to manufacturer, and we have seen values ranging from 0.05 nA/pixel up to 0.4 nA/pixel for “good” devices. The feedback resistor in the VA32C is generally set in the neighborhood of 1000 M $\Omega$ , and a punch-through bias resistor for an AC-coupled detector has a similar value. Using these values in Eqs. (4) and (5) gives the following values for the series and parallel noise components:

$$\sqrt{\langle q_{\text{series}}^2 \rangle} = 93e^- \quad (6)$$

$$\sqrt{\langle q_{\text{leakage}}^2 \rangle} = 43 - 95e^- \quad (7)$$

$$\sqrt{\langle q_{\text{res}}^2 \rangle} = 48e^- \quad (8)$$

Combining these in quadrature gives an overall noise equivalent charge of 113–140 e<sup>−</sup>. Multiplying by 3.62 eV per electron–hole pair in silicon at 300° K and by 2.35 to convert from  $\sigma$  to FWHM gives energy resolution of 961–1200 eV FWHM. It is clear that input capacitance and detector leakage currents are dominant effects. The reader is referred to Sansen and Chang (1990) and Knoll (2000) for further discussion of these effects.

### C. Physics Effects

#### 1. Doppler Broadening

The relationship between scattering angle and recoil energy of the struck electron described by Eq. (1) assumes that the initial momentum of the struck electron is zero. In

<sup>2</sup>Integrated Detector and Electronics (IDEAS ASA), Box 1, N-1330 Foruebu, Norway, Tel: +47 6782 7159, Specification sheets for the VA32C.2 and TA32CG.

fact, the incident gamma rays interact with bound electrons in the detector and these electrons have a momentum distribution that is specific to a given material and the physical state of the material. This precollision momentum distribution imposes an angular uncertainty of the scattered photon for a given measured recoil electron energy. In addition, the maximum Compton scattered energy is  $E_{\gamma 0} - E_b$ , the electron binding energy. The importance of the Doppler effect on limiting spatial resolution for the gamma-ray energies of interest in nuclear medicine was first pointed out by Ordóñez *et al.* (1997), who showed that the FWHM of the Doppler-broadened energy spectrum corresponding to a 45° scattering of 140-keV photons from germanium is 1.39 keV and from atomic silicon is 0.93 keV. The value for germanium is 1.6 times worse than the intrinsic energy resolution of the detector used by Singh, whereas the value for silicon is close to the limit for silicon pad detectors at room temperature with currently available CMOS readout.

The electron binding energy can introduce a bias in estimating the mean energy lost by the scattered photon. However, the resultant low-energy X-rays and Auger electrons that follow the shell vacancy caused by the Compton event are very likely to be deposited in the same pixel and significant bias is not likely.

Clinthorne, Hua, *et al.* (1998) have examined Doppler broadening for a number of potential detector materials and have calculated the effects on image variance and spatial resolution. Figure 4 illustrates the angular broadening for 140-keV photons that deposit recoil electron energy corresponding to a 60° scatter from a free electron. Figure 4a shows the contributions of the various subshells in atomic silicon. The uppermost curve is the weighted sum of the

subshell contributions. Compton profiles were taken from (Namito *et al.*, 1994), and more recent results are available in (Namito *et al.*, 2000). In Figure 4b the Doppler broadening for several possible detector materials is depicted normalized to the same area. Silicon is narrower than diamond at half maximum, but diamond has substantially reduced tails. Although one might expect that neon would exhibit reduced broadening because it has a large fraction of outer shell electrons, these electrons form a closed shell with relatively high binding energy. The curves for silicon and germanium are for the crystalline form. None of the curves is Gaussian, but can be fairly well represented by a superposition of three Gaussians.

## 2. Compton Scattering Cross Section

In the simple form of Compton camera illustrated in Figure 1, one wishes to maximize the probability of a single Compton interaction in the first detector followed by an escape and total residual energy deposition in detector 2. This requires that detector 2 subtend a large solid angle at the first detector and also be thick enough to stop the scattered gamma rays. The design of the second detector requires knowing the range of primary gamma-ray energies to be imaged and the range of scattering angles to be subtended by the second detector. The probability of a single scatter followed by an escape from the first detector depends on the Compton to total cross section for the first detector, the total amount of detector material, and its distribution about the source to be imaged. Figure 5 illustrates the Compton and Compton-to-total cross sections as a function of energy for silicon, germanium, and cadmium-zinc-telluride. Also shown are Compton angular distributions at three energies of interest.

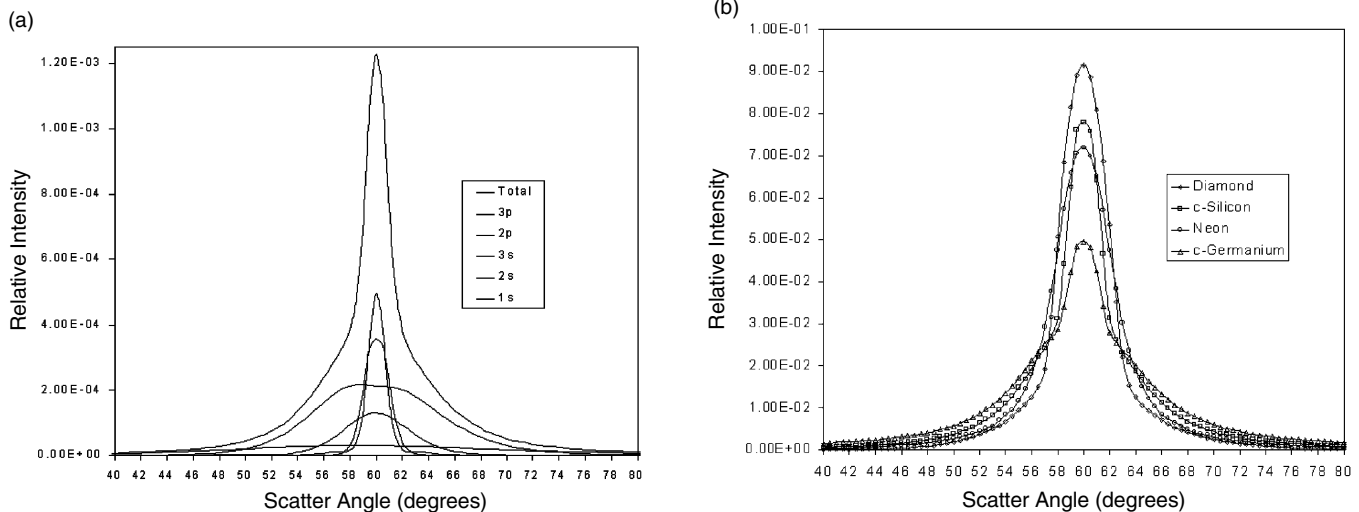


**FIGURE 4** Angular uncertainty due only to Doppler broadening for scattering 140-keV photons about 60°. (a) Contributions broken down by electron subshell for atomic silicon. (b) Doppler effect for four possible detector materials. The silicon and germanium curves are for the crystalline material. Note the increased broadening of the crystalline silicon compared to the atomic silicon at left. (Adapted from Clinthorne, Hua, *et al.*, 1998.)

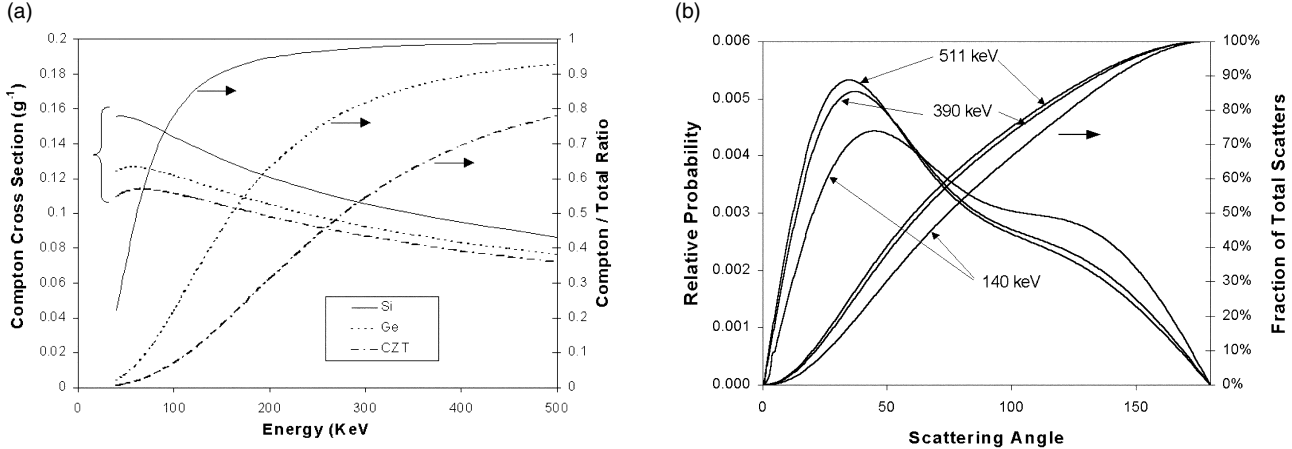


**FIGURE 5** (a) Compton cross section and Compton/Total cross section ratio for Si, Ge, and CZT. The densities of Si, Ge, and CZT are 2.33, 5.32, and 5.86 g/cc, respectively. (b) Compton angular distributions,  $d(\sigma)/d\theta$ , for three photon energies normalized to Compton total cross section. Also shown are the integrals of the angular distributions as a function of scattering angle.

It is evident from Figure 5 that the probability for a scatter and escape at 140 keV will be substantially higher for silicon than for either germanium or CZT, even out to 511 keV. However, because of the lower density of silicon, approximately twice the volume of silicon compared to germanium is required to obtain the same probability of a Compton interaction. From the angular distribution and its integral, one can estimate the relative dependence of sensitivity on the gamma-ray energy and the angular range of scattered photons accepted by the Compton imaging system. If scatters between 20° and 90° are accepted, then 54%, 59%, and 60% of the scattered photons will be accepted for 140, 390, and 511 keV respectively. However, because the probability of Compton scattering is higher at 140 keV, the relative sensitivity at these three energies is 1, 0.79, and 0.73.

### 3. Polarization

Single gamma rays emitted from a nucleus are unpolarized. That is, all orientations of the electric vector are equally likely. When an unpolarized beam undergoes Compton scattering it becomes partially linearly polarized orthogonal to the scattering plane because the scattering cross section for the perpendicular and parallel components is not the same (Klein and Nishina, 1929). The degree of polarization is a function of scattering angle and initial gamma-ray energy as illustrated by Eq. (9) (McMaster, 1961) and Figure 6:

$$P = \frac{\sin^2 \theta}{1 + \cos^2 \theta + \left( \frac{E_0 - E_1}{m_0 c^2} \right) (1 - \cos \theta)} \quad (9)$$

Moreover, a subsequent Compton scattering of this partially polarized beam will produce an azimuthally asymmetric intensity in the scattered gamma rays that depends on the angle between the incident gamma-ray polarization,  $\mathbf{e}_1$ , and the scattered gamma-ray polarization,  $\mathbf{e}_2$ . Kamae *et al.*

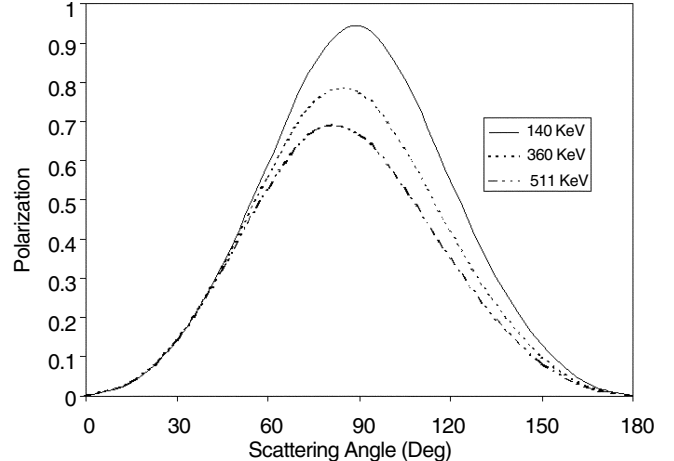


**FIGURE 6** Gamma-ray polarization as a function of scattering angle at three primary gamma-ray energies.

(1987) have described an application of this method to measuring the energy, direction, and polarization of incident gamma rays.

Polarization influences two aspects of Compton camera performance. First, gamma rays that scatter in the patient will be partially polarized. Those scattered gamma rays that cannot be rejected by energy windowing will have an asymmetric azimuthal scattering distribution in the first detector and should therefore be back-projected using a weighted azimuthal distribution. Because the initial scattering plane is unknown, there is no frame of reference for the asymmetry, so these events must be modeled using a uniform azimuthal distribution. The effects of this mismodeling have not been evaluated. Second, polarization effects can be used to reduce the conical ambiguity for gamma rays that have not been scattered in the patient. For gamma rays that undergo two or more scatters in a Compton camera, Dogan (1993; Dogan

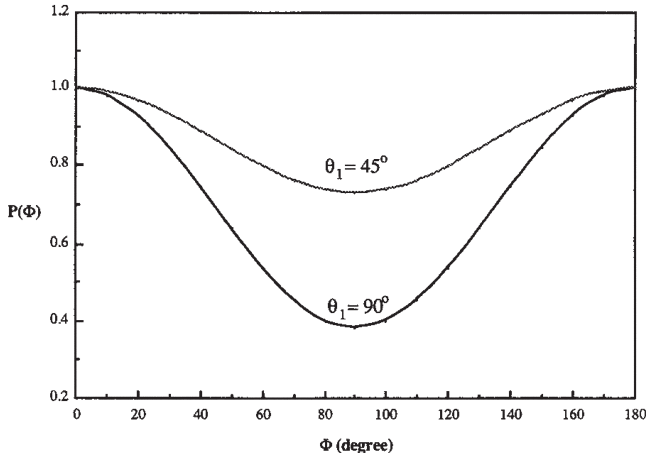


**FIGURE 7** Azimuthal probability of conical distribution derived for double Compton scattering for 150-keV incident gamma rays.  $\theta_1$  is the first scattering angle, and  $\Phi$  is the azimuthal angle around the cone measured with respect to the second scattering plane. (From Dogan *et al.*, 1992, © 1992 IEEE.)

*et al.*, 1992) has shown that it is possible to determine an azimuthal weighting function for the conical back-projection that reduces the ambiguity. One must first determine the sequence of interactions. Methods for sequencing have been described by Kamae and Hanada (1988), Dogan (1993; Dogan *et al.*, 1990, 1992), and Durkee (Durkee, Antich, Tsyganov, Constantinescu, Fernando, *et al.*, 1998; Durkee, Antich, Tsyganov, Constantinescu, Kulkarni, *et al.*, 1998) and essentially consist of determining which set of energies and scattering angles calculated for each of the postulated sequences best fits the data. For  $n$  interactions, there are  $n!$  sequences to test, so untangling more than three interactions could be very time consuming.

Figure 7 illustrates the probability of Compton double scattering as a function of azimuthal angle. Results are shown for 150-keV gamma rays and two different initial scattering angles (Dogan *et al.*, 1992). Polarization effects have been included in a system design study by Chelikani *et al.* (2004), but the effect of this added information on improving image quality for Compton imaging has not been completely investigated to our knowledge. However, it appears from Figure 7 that one can substantially reduce the ambiguity in azimuth for low-energy gamma rays for the larger scattering angles.

#### D. Combined Effects

By examining the combined effects of detector noise, Doppler broadening and gamma-ray energy as a function of scattering angle, it is possible to gain substantial insight into the relative importance of these factors and how they influence the design of a Compton camera. Figure 8 illustrates the combined effect of detector noise and Doppler broadening over a range of scattering angles for 140-keV (Hua

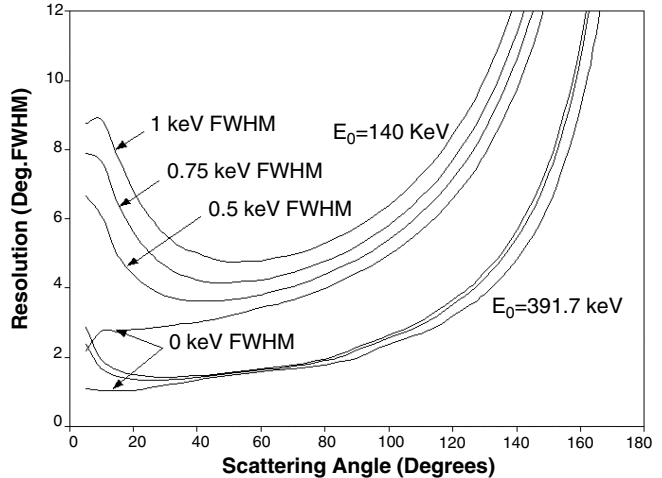


**FIGURE 8** Angular resolution for 140- and 392-keV gamma rays scattered from crystalline silicon for different values of detector energy resolution plus Doppler broadening and excluding geometric effects. Doppler effects shown for angles less than 10° are unreliable. Note that an uncertainty of 2° corresponds to a spatial resolution of 3.5 mm FWHM at 10 cm. (From Hua *et al.*, 1999, © 1999 IEEE.)

*et al.*, 1999) and 392-keV gamma rays, corresponding to  $^{99m}\text{Tc}$  and  $^{113m}\text{In}$ . The curves for 0-keV detector noise show the effects attributable to Doppler broadening alone. For  $^{99m}\text{Tc}$  this corresponds to approximately 5.5 mm at 10 cm, and for  $^{113m}\text{In}$  approximately 2.6 mm for a 45° scattering.

Several important points are illustrated by Figure 8.

1. For higher-energy gamma rays, the effect of detector noise is almost negligible except for scattering angles below 20°.
2. Doppler broadening is an important effect at both high and low energies, but is substantially smaller for small scattering angles.
3. Because Doppler effects favor small angle scattering, there remains good reason to attempt to reduce detector noise even though the Doppler and detector-noise components are comparable in the neighborhood of 60° scattering for 140-keV gamma rays.

Based on these curves it appears that one should design a camera system such that the second detector will capture all scatters from the first detector out to 90 or 120°, depending on the energy range of interest.

Not only does detector noise affect angular uncertainty, it also determines the minimum scattering angle that can be detected because the detector threshold must be set above the noise level. From Eq. (1), the mean energy deposited for a 15° scatter of a 140-keV gamma ray is 1.29 keV. If the toe of the noise distribution ( $3\sigma$ ) is 1.29 keV, then approximately one-half of the 15° scatters lie above this threshold. This corresponds to a detector energy resolution of approximately 1 keV FWHM.

Up to this point we have implicitly assumed that energy resolution in the second detector is only useful for accurately

measuring total gamma-ray energy as a means for reducing the effects of scattering in the patient or imaging multiple tracers. However, it has been pointed out by Clinthorne (2001) that if the incident gamma-ray energy is known, the best estimate of  $E_1$  is obtained from the measurement of both  $E_1$  and  $E_2$ . If detectors of unequal energy resolution are used, the uncertainty in  $\hat{E}_1$ ,  $\sigma_{\hat{E}_1}$  is

$$\sigma_{\hat{E}_1} = \sqrt{\frac{\sigma_1^2 \sigma_2^2}{\sigma_1^2 + \sigma_2^2}} \quad (10)$$

If detectors 1 and 2 have equal energy resolution, the uncertainty in scattering angle can be reduced by a factor of  $\sqrt{2}$ .

### III. ANALYTICAL PREDICTION OF SYSTEM PERFORMANCE

#### A. Noise Propagation and Lower Bound

Perhaps the most crucial question regarding the potential for Compton imaging in nuclear medicine is: How does Compton imaging compare to conventional imaging using Anger cameras with lead collimators? The comparison is complicated by the fact that projection images obtained from a collimated camera are a direct representation of the source distribution blurred by a Gaussian-like function characteristic of the system resolution. The raw image from a Compton camera is a superposition of conic sections that gives a point response function similar to a truncated  $1/r$  function. As such, these images have the poor resolution and low contrast observed in SPECT images reconstructed by simple back-projection, and a reconstruction or decoding step is required to obtain usable images. Just as is the case for SPECT, the image reconstruction process amplifies image noise so that a simple comparison of raw detection efficiency between a collimated and Compton imaging system does not predict relative imaging performance. Furthermore, for Compton imaging systems we have shown that sensitivity and resolution depend on detector material, electronic noise, detector geometry, and gamma-ray energy in a complex manner. Thus, it is important to have an analytical method to compare the performance of different Compton camera system designs.

The question of noise propagation in Compton imaging compared to mechanical collimation was addressed by Singh and colleagues (1988) by a theoretical analysis using an annulus as an approximate response function for planar imaging. The annulus corresponds to a Compton camera response function for one scattering angle and an on-axis point source. They also describe simulations and experimental measurements using inverse filtering and algebraic reconstruction technique (ART) to reconstruct images. Their results showed a factor of 3 loss in signal-to-noise ratio (SNR) for a  $^{137}\text{Cs}$

disk object as the diameter increased from 2 cm to 10 cm. For a 5-cm-diameter disk, the Compton camera image had a factor of 3 lower SNR than a pinhole image with the same number of counts. The authors conclude that for the 661-keV gamma rays of  $^{137}\text{Cs}$  the effective sensitivity of a Compton camera is reduced by approximately a factor of 3 compared to mechanical collimation. Thus, to break even, the raw sensitivity of the Compton camera must be three times that of the collimated system. In the following sections, we present more recent results based on a more accurate system model and lower bound calculations that are independent of the particular reconstruction method.

#### 1. Introduction to Lower Bound

The Cramer-Rao (CR) lower bound on estimator variance gives the lowest variance in a parameter of interest that can be achieved by any unbiased estimator. Thus, this measure of performance depends only on the object and the set of measurements and *not* on the estimator. The object must be represented by a finite set of parameters such as voxels or pixels,  $\mathbf{o} \equiv [o_1, \dots, o_m]$ , and a statistical model must exist that relates the conditional probability of object parameters to the measurements:

$$f(\mathbf{y}|\mathbf{o}), \quad (11)$$

where  $\mathbf{y} \equiv [y_1, \dots, y_N]^T$  is the vector of  $N$  measurements. The bound is defined (Blahut, 1987) as the inverse of the Fisher information matrix,  $\mathbf{F}$ .

$$\mathbf{K}_{\mathbf{o}} \geq \mathbf{F}^{-1} \equiv E[\nabla_{\mathbf{o}}^2 \log f(\mathbf{y}|\mathbf{o})]^{-1} \quad (12)$$

For conditionally Poisson distributed measurements, as well as for Gaussian measurements in which the covariance is not a function of the parameters, the Fisher information matrix becomes:

$$\mathbf{F} = (\nabla \bar{\mathbf{y}}(\mathbf{o}))^T \mathbf{K}_{\mathbf{y}}^{-1} \nabla \bar{\mathbf{y}}(\mathbf{o}) \quad (13)$$

It is important to note that the CR bound can be asymptotically achieved by the maximum-likelihood estimator. Further, Clinthorne, Ng, *et al.* (1998) have shown that the CR bound is equivalent to the more familiar propagation-of-error formula applied to the maximum-likelihood estimator. The CR bound, however, has the advantage of being estimator-independent.

#### 2. Uniform Cramer-Rao Bound

The difficulty with applying the CR bound to image reconstruction is that one can seldom use unbiased estimators because of the ill-conditioned nature of these problems. Instead one must use biased estimators that directly or indirectly impose smoothness constraints on the solution in order to reduce the mean-squared error in the images. Although one can define a CR bound for a particular biased estimator, Hero (1992; Hero *et al.*, 1996) has shown that it is possible to define a uniform CR (UCR) bound that is

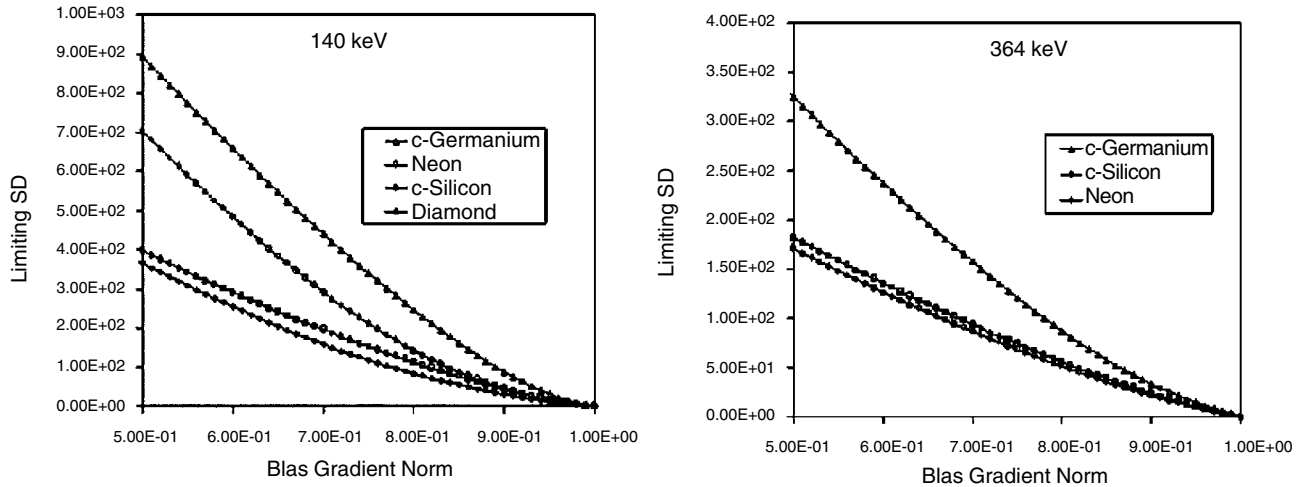


FIGURE 9 Uniform lower bounds for different detector materials, considering only the effects of Doppler broadening at 140 and 364 keV. Scattering angles from 45 to 90°. (From Clinthorne *et al.*, 1998).

estimator-independent. The UCR bound depends on the norm of the bias gradient<sup>3</sup> rather than on the bias gradient specific to a given estimator.

The bias of the  $p$ th element of the object vector is  $\bar{\delta}_p - o_p$  with gradient

$$\frac{\partial \bar{\delta}_p}{\partial o_i} - \frac{\partial o_p}{\partial o_i}, i = 1 \dots p \dots M \quad (14)$$

For the imaging problem, the second term will be 0, except when  $i = p$ , in which case, it is 1. The elements of the bias gradient are then:

$$\left[ \frac{\partial \bar{\delta}_p}{\partial o_1}, \dots, \frac{\partial \bar{\delta}_p}{\partial o_p} - 1, \dots, \frac{\partial \bar{\delta}_p}{\partial o_M} \right] \quad (15)$$

The bound calculation yields the optimal bias gradient in the sense that no other bias gradient with the same norm will give a lower variance in the estimated parameter. If the system is spatially invariant,<sup>4</sup>

$$\frac{\partial \bar{\delta}_i}{\partial o_p} = \frac{\partial \bar{\delta}_p}{\partial o_i} \quad (16)$$

By adding 1 to the  $p$ th element, one obtains the mean gradient of the estimate that is also seen to be the impulse response function. We see that the norm of the bias gradient is closely related to the norm of the impulse response function.

<sup>3</sup>Also referred to as the bias gradient length.

<sup>4</sup>More precisely this is true if  $(\mathbf{F} + \alpha \mathbf{R})^{-1} \mathbf{F} = \mathbf{F}(\mathbf{F} + \alpha \mathbf{R})^{-1}$  where  $\mathbf{F}$  is the Fisher information matrix,  $\mathbf{R}$  is the penalty function and  $\alpha$  is the strength of the penalty. If  $\mathbf{R}$  is the identity matrix (0th-order Tikhonov regularization), this is the case, and it will be approximately true for  $\mathbf{R}$  equal to a roughness penalty based on squared differences between a pixel and its nearest neighbors.

### 3. Applications of Lower Bounds

#### a. Doppler Broadening for Different Materials

Uniform bounds for estimating the center pixel in a 7.5-cm disk source have been calculated to evaluate the effects of the Doppler broadening for the detector materials illustrated in Figure 4 at 140 and 360 keV (Clinthorne *et al.*, 1998). The source was located 10 cm from a point detector and scattering angles from 45 to 90° were accepted. Electronic and statistical noise components were taken as zero, and perfect geometric resolution was assumed.

The results are illustrated in Figure 9. For lower-energy gamma rays, diamond slightly outperforms crystalline silicon, neon is substantially inferior to both diamond and silicon, and germanium is poorest. At 364 keV, the standard deviation for all detector materials decreases, but neon slightly outperforms crystalline silicon, and germanium clearly remains worst.

These curves demonstrate the importance of the tails of the line spread function relative to the width of the central peak as gamma-ray energy changes. Neon has a wider central peak compared to silicon because of the higher energy of the valence electrons in the closed shell. However, the fraction of neon valence electrons is higher than silicon. As gamma-ray energy is increased, the effect of long-range tails becomes the dominant factor limiting performance for silicon and germanium. The contribution of these tails is explicitly included in the bias gradient norm and accounts for the changes in the UCR bound with gamma-ray energy. The actual computation of these bound curves was performed on eight nodes of an IBM SP2 parallel processor, and each curve required approximately 1 week of computation.

#### b. Comparison of Compton Cameras to Collimated Systems

The UCR bound has also been used to quantify Compton camera planar imaging performance relative to conventional

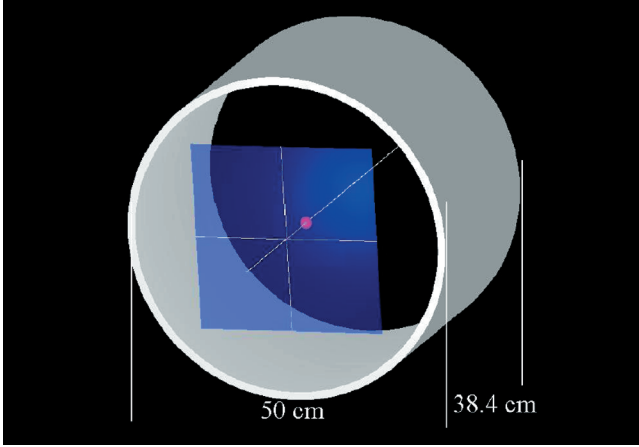


FIGURE 10 Ring Compton camera system used for UCR bound calculations. The source plane is 10 cm in front of the front edge of the cylindrical second detector. The point first detector lies on-axis 10 cm behind the object plane.

imaging systems (Clinthorne *et al.*, 1996; Hua, 2000; Hua *et al.*, 1999). Bound calculations were made for a ring geometry Compton camera illustrated in Figure 10. This is an idealized version of an experimental ring camera to be described later. The point first detector is crystalline silicon, and the second detector is quantized into 512 pixels around the circumference and 128 pixels axially to give a pixel size of approximately 3 mm. Depth of interaction effects were not modeled. The  $30\text{ cm} \times 30\text{ cm}$  source plane is represented by an array of  $64 \times 64$  pixels 4.7 mm square. Only scattering events between  $45^\circ$  and  $90^\circ$  were considered because they have the highest resolution (see Figure 8).

The system model included Doppler broadening for crystalline silicon, and bounds were calculated for first-detector electronic noise levels corresponding to energy resolution of 0.5 keV and 0.75 keV FWHM. The system parameters are optimistic and represent close to a best-case model. The collimator-camera response functions were based on measurements for pixel-sized sources. Resolution was 8.6 mm FWHM at 10 cm for the low-energy high-resolution (LEHR) collimator with  $^{99m}\text{Tc}$ , and 11.3 mm FWHM for the high-energy collimator with  $^{131}\text{I}$ . The bias gradient norms corresponding to these measured responses were 0.76 and 0.87, respectively.

Figure 11 illustrates the effect of object size on the limiting standard deviation in the estimate of the central pixel of a planar disk source. For reference, the effect of detector energy resolution for the 7.5-cm disk is also shown. The dependence on object size is a direct consequence of the fact that the signal from the central pixel is spatially multiplexed with the signals from all other pixels. As the size of the disk is increased, the variance of the added source volume is propagated to the pixel of interest. This is essentially the same sort of dependence of image noise on object diameter that

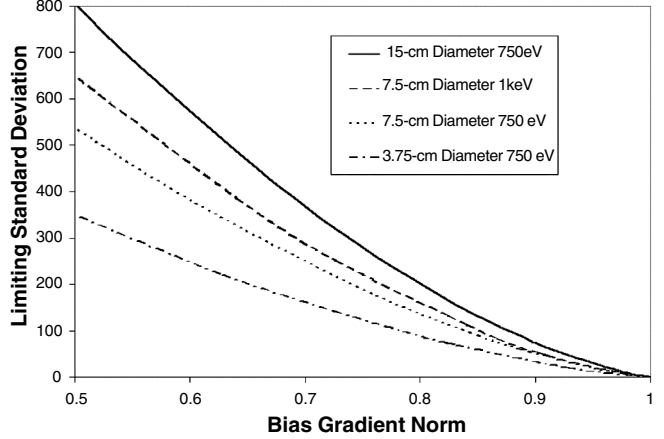


FIGURE 11 Comparison of lower-bound curves for a Compton camera as a function of object diameter normalized to the same number of detected photons per unit area. Minimum standard deviation in the estimate of the central pixel for various diameter disk sources is plotted as a function of bias gradient norm for 140-keV gamma rays. (From Hua *et al.*, 2000, © 2000 C-H Hua)

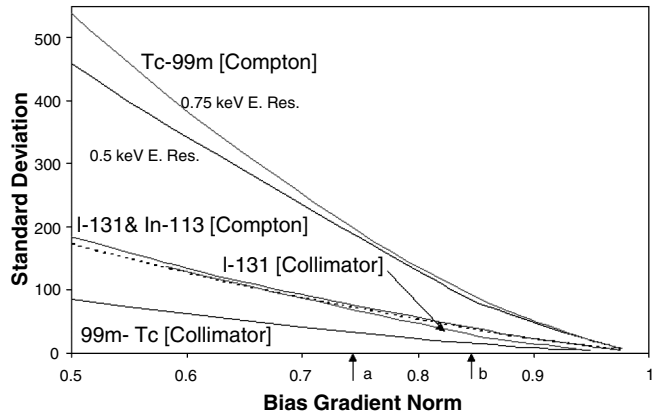


FIGURE 12 Comparison of lower-bound curves for a Compton camera and two conventional collimated camera systems normalized to the same number of detected photons. Minimum standard deviation in the estimate of the central pixel in a 7.5cm diameter disk source is plotted as a function of bias gradient norm. The bias gradient norm at point a corresponds to that for the measured camera point response function with a LEHR collimator at 10 cm. Point b is for a high-energy iodine collimator at 10 cm. (From Hua *et al.*, 1999, © 1999 IEEE.)

one observes in tomographic imaging. At a bias gradient norm of 0.74, the standard deviation increases a factor of 1.47 from 133 to 196 when the disk diameter is doubled from 3.75 to 7.5 cm. This dependence on object size is similar to that obtained by Singh *et al.* (1988) for 5.33- and 10-cm diameter disks. Based on analytical SNR calculations for a ring aperture model of a Compton camera compared to an ideal pinhole, they obtain factor of 1.74 increase in standard deviation for the 10-cm disk compared to the 5.33-cm disk.

Figure 12 shows bound curves for the Compton camera at 140 keV ( $^{99m}\text{Tc}$ ), 361 keV ( $^{131}\text{I}$ ), and 391.7 keV ( $^{113m}\text{In}$ ) (Hua *et al.*, 1999). The first-detector energy resolution is 0.75 keV,

and for Tc the effect of improving resolution to 0.5 keV is also illustrated. For the collimated camera, bounds for  $^{99m}\text{Tc}$  and  $^{131}\text{I}$  are shown. These curves are all normalized to an equal number of detected events, so they portray the relative information carried by a detected photon for each of the imaging systems. At 140 keV the collimator gives a substantially lower standard deviation than the Compton camera for the same number of detected events, whereas at 360 keV almost identical performance can be achieved.

Since the relative standard deviation for any of the systems will be inversely proportional to the square root of the number of detected events, one can estimate a noise-equivalent sensitivity for the Compton and collimated systems from these curves. We define *decoding penalty* as the variance of the Compton camera divided by the variance of the collimated system. The decoding penalty specifies how much greater sensitivity the Compton system must have in order to give relative standard deviation equal to that of the collimated system for planar imaging.

From Figure 13, the decoding penalty for imaging a 7.5-cm-diameter disk source with  $^{99m}\text{Tc}$  is approximately 40. For a 15-cm Tc disk source the decoding penalty increases to 91 (Hua, 2000; Hua *et al.*, 1999). For a 7.5-cm  $^{131}\text{I}$  disk the penalty varies from 1 to 1.5. This reflects the fact that Compton camera performance improves with increasing energy while collimator performance degrades.  $^{113m}\text{In}$ , which emits a 391.7-keV gamma ray, has a decoding penalty of approximately 5 when compared to  $^{99m}\text{Tc}$  imaged with a conventional camera system. This isotope of indium is of potential interest because it can be obtained from a  $^{113}\text{Sn}$  generator and has a 100-minute half-life. The parent half-life is 119 days. Because of differences in radiation dosimetry, LeBlanc and co-workers (LeBlanc, Clinthorne, *et al.*, 1999) conclude that the effective sensitivity increase of a Compton camera must be increased to between 5 and 8, depending on tracer distribution in the

patient, to obtain a comparable standard deviation for equal patient radiation dose.

The results shown in Figure 13 agree in spirit with the results of Singh *et al.* (1988) for the 662-keV gamma rays from  $^{137}\text{Cs}$ . Based on the SNR computed for the ring aperture relative to the ideal pinhole collimator, they predict a decoding penalty of 4 for a 5.33-cm-diameter disk source. Experimental measurements with a 4.7-cm-diameter disk and image reconstruction using ART give a decoding penalty of approximately 2.3. These are slightly more pessimistic results than the previous predictions based on a lower-bound analysis for silicon detectors at 360 keV and a 7.5-cm-diameter disk source. Nevertheless, it is clear that a Compton camera must be substantially more sensitive than mechanical collimation to yield any gain in performance, especially for lower-energy gamma rays. Some estimates of sensitivity increases that might be obtained from Compton cameras are described in a later section.

## B. Observer Performance

The lower-bound analysis of Compton cameras just given provides an assessment of relative performance of Compton imagers and collimated imagers for the task of quantification. It is of equal, or perhaps of greater, importance to examine how Compton cameras might perform relative to collimated systems for the lesion-detection task. The ideal Bayesian observer with signal known exactly and background known exactly (SKE and BKE) is one of the simplest, albeit overoptimistic, quantitative measures of lesion detectability. In this case the only noise source stems from the uncorrelated measurement noise, and the task is to determine the presence or absence of a lesion in a background distribution. Although actual human observer performance for a more complex signal and background representation is the ultimate measure of a medical imaging system performance, the ideal observer performance is readily calculated directly from the data and is appropriate for the early stages of instrumentation development when one wishes to evaluate the effects of a variety of system parameters.

### 1. Ideal Observer—Signal-to-Noise Ratio

The ideal observer makes the lesion-present–lesion-absent decision based on a function of the likelihood ratio of the lesion-present and lesion-absent raw data for a specified threshold (Fisher, 1925). The detectability index for an ideal observer is given by the SNR defined in Eq. (17).

$$\text{SNR}^2 = \frac{\left[ \bar{\lambda}_1 - \bar{\lambda}_0 \right]^2}{\frac{1}{2} \left[ \sigma_1^2 + \sigma_0^2 \right]} \quad (17)$$

where  $\bar{\lambda}_j$  and  $\sigma_j^2$  represent the mean and variance of the decision variable under signal-absent and signal-present hypotheses ( $j = 0, 1$ ). Let  $\mathbf{g}$  represent a column vector

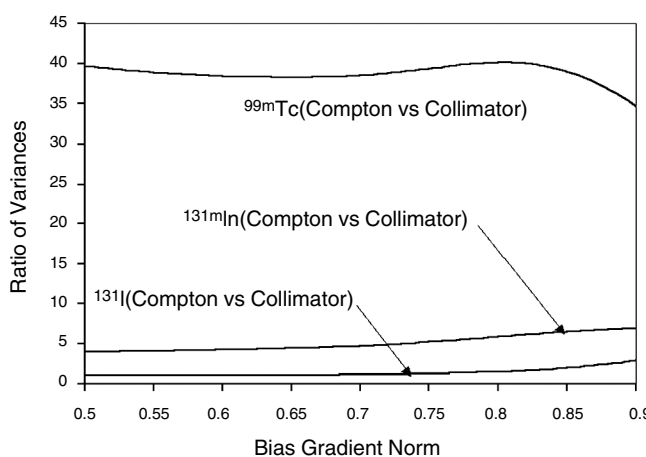


FIGURE 13 Plots of decoding penalty for the center pixel of a 7.5-cm-diameter disk source. (From Hua *et al.* 1999, © 1999 IEEE.)

of projection data from a given imaging system where  $\mathbf{g} \approx \text{Poisson}(\mathbf{Af})$ .  $\mathbf{A}$  represents the system matrix and  $\mathbf{f}$  is a column vector representing the object. The likelihood ratio of the two hypotheses is (Fukunaga, 1972):

$$\mathbf{L}(\mathbf{g}) = \frac{P(\mathbf{g}|H_1)}{P(\mathbf{g}|H_0)} \quad (18)$$

One may also use the log of the likelihood ratio as the ideal decision variable; hence:

$$\bar{\lambda}_{\text{ideal}} = \log(P(\mathbf{g}|H_1) - P(\mathbf{g}|H_0))$$

Following the methods of (Hua, 2000) for a large number of realizations,

$$\bar{\lambda}_0 = E(\lambda_{\text{ideal}}|H_0) = (\log \bar{\mathbf{g}}_1 - \log \bar{\mathbf{g}}_0)^T \bar{\mathbf{g}}_0 \quad (19)$$

$$\bar{\lambda}_1 = E(\lambda_{\text{ideal}}|H_1) = (\log \bar{\mathbf{g}}_1 - \log \bar{\mathbf{g}}_0)^T \bar{\mathbf{g}}_1 \quad (20)$$

$$\sigma_1^2 = (\log \bar{\mathbf{g}}_1 - \log \bar{\mathbf{g}}_0)^T \text{diag}(\bar{\mathbf{g}}_1) (\log \bar{\mathbf{g}}_1 - \log \bar{\mathbf{g}}_0) \quad (21)$$

$$\sigma_0^2 = (\log \bar{\mathbf{g}}_1 - \log \bar{\mathbf{g}}_0)^T \text{diag}(\bar{\mathbf{g}}_0) (\log \bar{\mathbf{g}}_1 - \log \bar{\mathbf{g}}_0) \quad (22)$$

and the SNR, Eq. (17), for an imaging system may be calculated for the two hypotheses.

## 2. Signal-to-Noise Ratios for Compton Cameras and Collimated Imaging Systems

Using the same system matrices for the Compton Camera and collimated camera described for the uniform-bound calculations,  $\text{SNR}^2$  was calculated for the task of detecting Gaussian-shaped lesions centered on a larger-diameter Gaussian-shaped background (Hua, 2000). Effects of lesion and background diameter, lesion contrast, and gamma-ray energy were studied for both imaging systems under the constraint that both systems detect an equal number of photons. The  $\text{SNR}^2$  depends linearly on the total number of counts and increases essentially linearly with lesion contrast over the range 0–0.5. Thus, the ratio of  $\text{SNR}^2$  for the collimated camera to the Compton camera as a function of lesion contrast is almost constant and for the same total counts gives an estimate of how much more sensitive the Compton camera must be to give  $\text{SNR}^2$  equal to the collimated camera for equal imaging time. These results are summarized in Table 1. These values have an interpretation for the detection task similar to the decoding penalty derived from the uniform bound for the quantification task, but for Gaussian-shaped lesions on a Gaussian-shaped background. The values of  $\text{SNR}^2$  in brackets are for the same single pixel on a uniform disk used for the estimation task. It is of note that the relative performance of the Compton camera improves slightly for the single-pixel detection task. The same general trends are observed for the detection task and quantification task: (1) Relative Compton camera performance improves with higher gamma-ray energy and (2) relative Compton camera

TABLE 1 Ratio of  $\text{SNR}^2$  for Collimators with Respect to Compton Camera for Equal Counts

Lesion Diameter (mm)	$^{99m}\text{Tc}$ at 140 keV, Background Diameter (cm)			$^{131}\text{I}$ at 364 keV, Background Diameter (cm)		
	3.75	7.5	15	3.75	7.5	15
5	4.2	10.1 [9.3] <sup>a</sup>	30.0	1.9	4.0 [3.25] <sup>a</sup>	11.5
10	2.8	6.6	19.5	1.8	3.7	10.4
15	2.0	4.6	13.5	1.5	3.2	9.0
20	1.6	3.5	10.5	1.3	2.7	7.5

<sup>a</sup>From Hua (2000).

Numbers in brackets are  $\text{SNR}^2$  for detecting a single 4.7-mm pixel on a 7.5-cm-diameter uniform disk. This is to enable comparison to the decoding penalty derived from uniform bound. All other values of  $\text{SNR}^2$  are for Gaussian lesions on a Gaussian background.

performance decreases with object size. The decrease in relative performance between a 3.75-cm-diameter object and a 7.5-cm object is 2.4 using lower bounds and 2.2 using the ideal observer. However, the actual ratios derived for the detection task are more favorable to the Compton camera at 140 keV and, surprisingly, less favorable at 360 keV. Based on bound calculations, the decoding penalty is approximately 40 for  $^{99m}\text{Tc}$  and 1.5–2.0 for  $^{131}\text{I}$  for single-pixel estimation on a 7.5-cm disk. The detection task for the same object gives corresponding values of 9.3 and 3.25 for Tc and I, respectively. This is clearly a point requiring further investigation.

## 3. Ideal Observer—Area under Receiver Operating Curves

If the decision variable,  $\lambda$ , is Gaussian distributed, the area under the receiver operating curve (ROC) is given by (Barrett *et al.*, 1998):

$$\text{Area} = \frac{1}{2} + \frac{1}{2} \text{erf}\left(\frac{\text{SNR}}{2}\right), \quad (23)$$

where erf is the error function. This mapping of the SNR is illustrated in Figure 14. These curves quantify the lesion detectability for the two imaging systems. As expected, collimator performance is independent of object size and, in terms of lesion size, the collimator performance for a 5-mm lesion is almost the same as that of the Compton system for a 10-mm lesion for an equal number of detected photons.

## C. Predicted Efficiency Gains for Various Geometries

It is abundantly evident from both the lower bound and observer comparisons of Compton cameras to collimated cameras that Compton imaging systems must have a raw gamma-ray detection sensitivity that exceeds that of the collimated system by a factor of 2 up to 100 or more

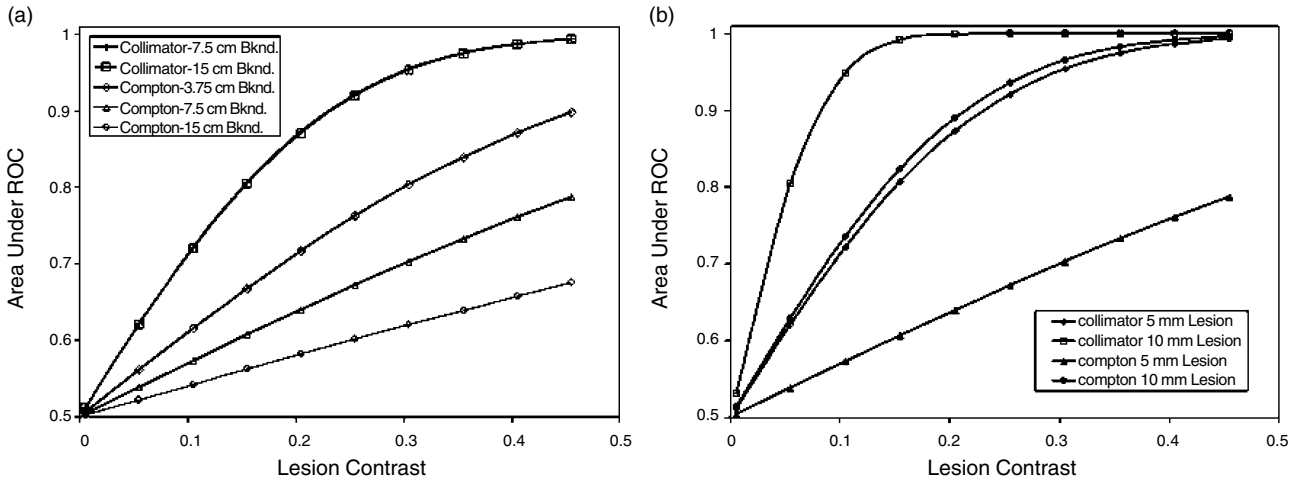


**FIGURE 14** Area under the ROC as a function of lesion contrast for 140-keV gamma rays. (a) Comparison of Compton camera to collimated cameras for 5 mm FWHM Gaussian lesion and various diameter Gaussian backgrounds. (b) Relative camera performance for different lesion diameters and a 7.5-cm-diameter background. The Compton and collimated imaging systems each detected the same number of events. (From Hua, 2000, ©2000 C. H. Hua.)

depending on object size and gamma-ray energy (and the metric employed). In this section we examine the sensitivity gains that might be expected for two system geometries. The data are restricted to single scattering in the first detector followed by an escape and detection in the second detector.

### 1. Ring Compton Camera

The ring Compton camera, as portrayed in Figure 10, is hardly optimal, but it is a useful geometry for obtaining preliminary experimental data to verify the theoretical predictions. In particular, it is possible to shield the second detector from direct radiation by the source so that high activity sources may be used to obtain data from small first detector prototypes without saturating the second detector. It is also possible to vary the axial position of the first detector to investigate the dependence on scattering angles accepted and to restrict data to that with the highest resolution at a particular energy. To determine the sensitivity limits of the ring Compton camera geometry, Monte Carlo calculations using the SKEPTIC code (Wilderman, 1990) were carried out considering different size silicon detectors as a function of silicon thickness (Cinthorne *et al.*, 1996) for both 140 and 360 keV. Point sources were located on-axis 10 cm from the silicon detector. Sensitivities relative to low- and high-energy collimators were computed using a measured efficiency of  $1.3 \times 10^{-4}$  for the LEHR collimator and manufacturer-specified sensitivity of  $1 \times 10^{-4}$  for the high-energy collimator. For the Compton camera, only events that underwent a single scattering followed by detection in the ring detector were counted. The second detector is 1-cm-thick NaI, except for one case for  $^{131}\text{I}$  in which the thickness was increased to 2.54 cm to illustrate the system sensitivity dependence on second detector thickness at higher energies. These results are plotted in Figure 15.

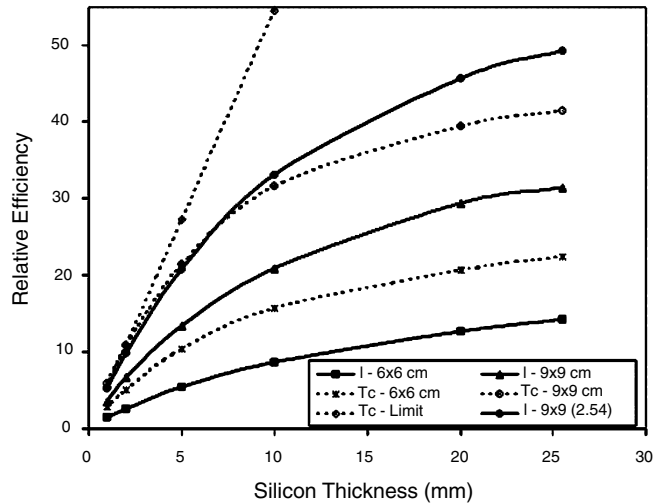


**FIGURE 15** Relative efficiency of a Compton camera compared to a collimated camera for  $^{99\text{m}}\text{Tc}$  and  $^{131}\text{I}$  as a function of silicon thickness and area. The system geometry is the same as for Figure 10. The solid curves are for  $^{131}\text{I}$ , and the increase in efficiency for the upper curve for the  $9 \times 9$  cm silicon detector illustrates the effect of increasing the second-detector thickness from 1 cm to 2.54 cm of NaI. (From Clinthorne *et al.* 1996, © 1996 IEEE.)

At 140 keV, a sensitivity gain of approximately 40 can be realized for a 25-mm-thick stack of  $9 \times 9$  cm arrays of silicon detectors, whereas at 365 keV a factor of 30 can be attained for a 1-cm-thick second detector. Increasing the second-detector thickness to 2.54 cm gives a sensitivity gain of almost 50 for iodine. The nonlinearity of the curves with thickness is due to the increased probability of absorption prior to the initial scattering or a second scattering or absorption following the initial scattering. Increasing first-detector size from  $6 \times 6$  cm to  $9 \times 9$  cm increases the area

by a factor of 2.25 and increases the relative Tc sensitivity by a factor of 2.01 for 10-mm thickness, whereas increasing the  $6 \times 6$  cm array from a thickness of 10 to 20 mm only increases the sensitivity by a factor of 1.3. This strongly suggests that one should consider distributing the same volume of first detector over a larger area with reduced thickness. The linear curve projects limiting gains that could be achieved by eliminating self-shielding and a second scattering or absorption following the initial scattering. In this case, one might achieve a sensitivity gain of 55 for  $^{99m}\text{Tc}$  with a volume of 81 cc of silicon rather than a gain of 30.

## 2. Double-Ring Geometry

A double-ring geometry comprising a cylindrical first detector surrounded by a cylindrical or tire-shaped second detector has been described by several investigators (Ichihara, 1987; Rohe and Valentine, 1995, 1996; Valentine *et al.*, 1996; Bolozdynya, Ordonez, *et al.*, 1997). This geometry has several advantages. First, the scattering detector is distributed over a large area, and the problems of self-shielding and multiple scattering previously alluded to for large first-detector volume are greatly reduced and substantial sensitivity increases might be expected. Second, complete angular sampling of a source distribution is possible with no camera rotation. The major disadvantage is that the second detector directly views the source so that it must have very high count rate capability to avoid pile-up, dead time, and high accidental coincidence rates. The count rate will also be higher because the second detector views more small-angle scatters that do not carry high-resolution information and that will fall below the noise threshold of the first detector.

The system geometry illustrated in Figure 16 is configured such that up to  $90^\circ$  scatters from the mid-plane of the silicon ring will be intercepted. Again, the SKEPTIC Monte Carlo code was used for the simulation. Events were biased to intercept the silicon ring and were restricted to scattering events that deposited full energy in the system and whose scattering angles were between 20 and  $90^\circ$ . Calculations were performed for  $^{99m}\text{Tc}$  and  $^{131}\text{I}$  and were sorted into the following categories:

1. Single scattering in the silicon ring followed by absorption in the BGO ring.
2. Multiple scattering in the silicon ring followed by absorption in the BGO ring.
3. Single or multiple scattering in silicon followed by absorption in silicon.
4. The sum of 1 through 3.

Two points are evident from Figure 17. First, most of the sensitivity gain is reached for both Tc and I at a silicon thickness of approximately 16 mm if one restricts the events to single scattering in silicon. Second, at this thickness, one could achieve a further 50% sensitivity increase by including the second category of interaction, and appre-

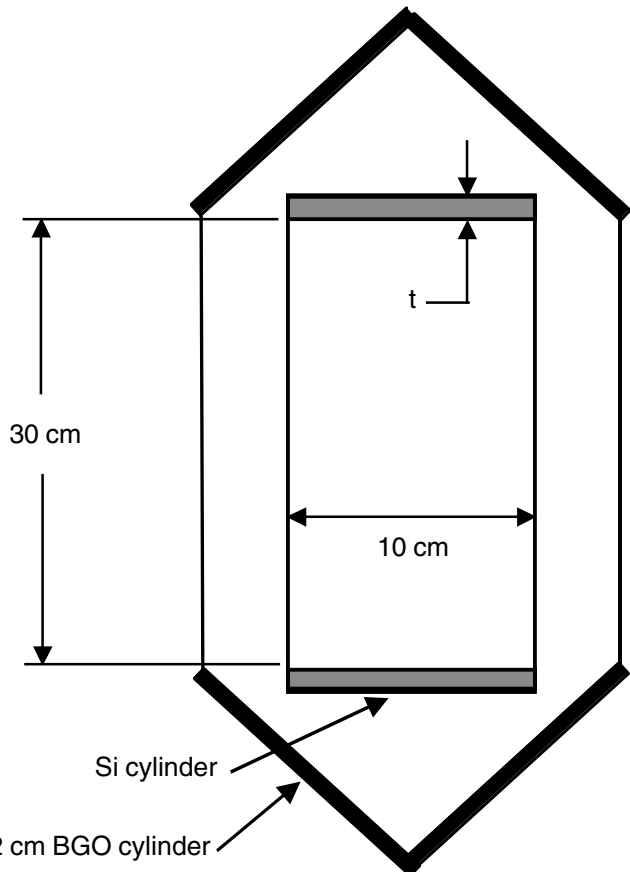


FIGURE 16 Cross section of a double-ring-geometry Compton camera used for Monte Carlo simulations of system sensitivity for a point source located on-axis.

ciable gains can then be achieved by further increasing silicon thickness.

In Figure 18, detection sensitivities for Tc and I are compared to those for the respective collimators. The data from Figure 17 were normalized to the fractional solid angle subtended by the silicon ring and divided by the appropriate collimator sensitivity. Considering single scattering in silicon followed by capture in the BGO ring we see that even for a 4-mm-thick Si ring, sensitivity gains of 153 and 133 for Tc and I, respectively, are predicted. Increasing the thickness to 16 mm increases these ratios to 298 and 420. These sensitivity gains are substantially greater than the decoding penalties calculated earlier, especially for the higher energy of  $^{131}\text{I}$ . Although these relative sensitivities may be further increased by using multiple scattering events, this can only be realized at the expense of more complex data processing. Not only must one calculate the sequence of interactions by analyzing the kinematics, but one must also consider the effects of polarization, especially at lower energies. This is further complicated by the fact that accurate computation of the scattering angle between successive scattering events in

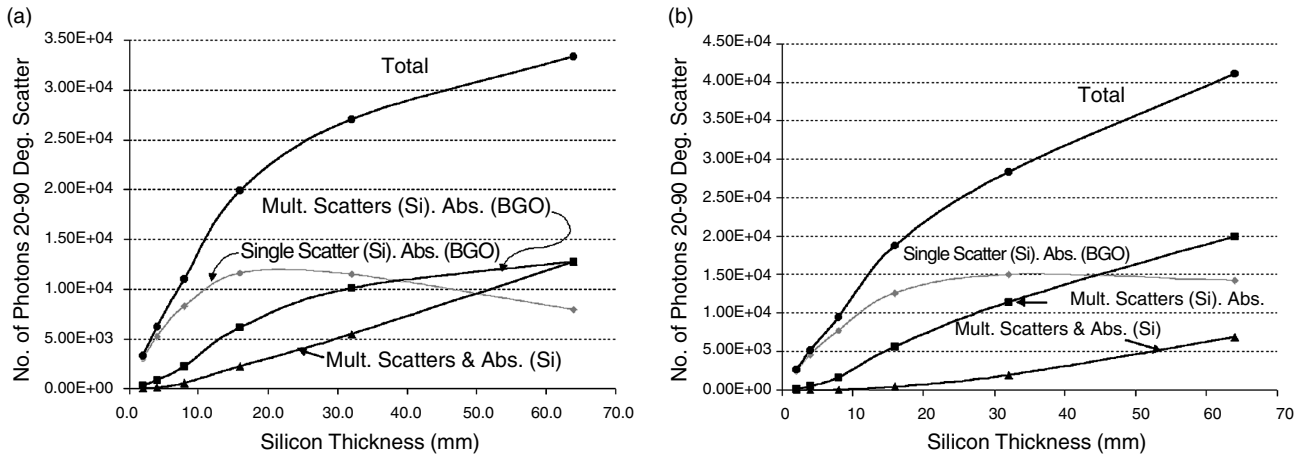


FIGURE 17 Number of photons per 100,000 incident on a silicon ring sorted into the three labeled interaction sequences. (a)  $^{99m}\text{Tc}$ . (b)  $^{131}\text{I}$ .

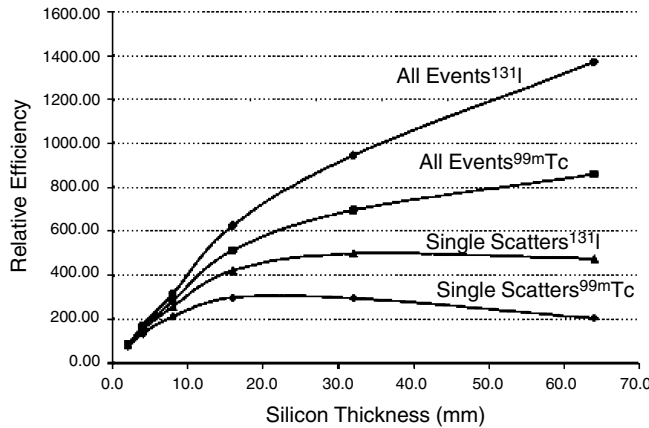


FIGURE 18 Relative sensitivities of the double ring Compton camera geometry and parallel hole collimators for  $^{99m}\text{Tc}$  and  $^{131}\text{I}$ .

silicon depends both on the silicon voxel size and the distance between the successive events. Reducing the pixel voxel dimensions by a factor of 2 increases the system matrix a factor of 8, and for discrete pixel detectors one predicts a factor of 8 increase in price as depicted in Figure 19. On the plus side, using the polarization information is expected to reduce the conical ambiguity and thereby reduce the decoding penalty. A careful analysis will be required to quantify the trade-off.

The relation between cost and pixels shown in Figure 19 is based on the large-scale production of silicon detector arrays such as used in high-energy physics experiments. We have assumed detectors with discrete pixels rather than orthogonal strip detectors because they have lower noise due to their lower input capacitance and, as we have seen, this is of primary importance for imaging  $^{99m}\text{Tc}$ . For applications to  $^{131}\text{I}$  or higher-energy gamma rays, double-sided strip detectors might prove to be a good choice.

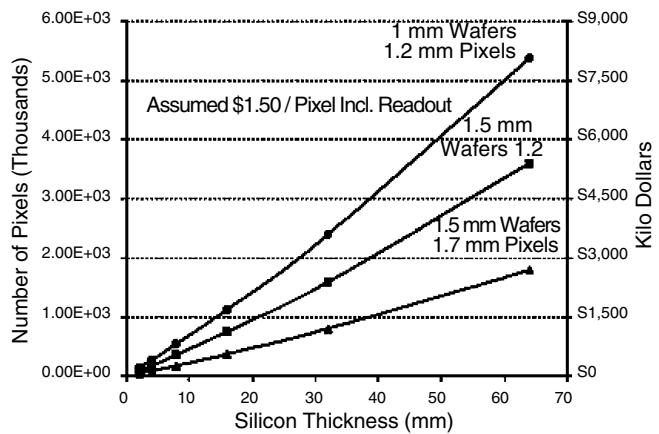


FIGURE 19 Number of  $1.4 \times 1.4$  mm silicon pixels as a function of ring thickness for different silicon wafer thickness for pixel- voxel-type silicon scatter detectors. Estimated cost per pixel includes the readout electronics.

#### IV. IMAGE RECONSTRUCTION FOR COMPTON CAMERAS

##### A. Background

Ever since the Compton camera was proposed for medical applications by Todd, Nightingale, and Everett (1974), image reconstruction has been an issue. As in X-ray telescopes, the first image reconstruction methods proposed consisted simply of backprojecting event circles corresponding to the data uncertainty into a discretized image space with no additional filtering or processing. Such backprojection, while it may serve as a useful demonstration for point source reconstruction, is just as inappropriate for Compton camera reconstruction as it is for conventional SPECT or PET imaging. The tails of the each event circle, being positive, do not cancel and the result is a significantly blurred estimate of

the radiotracer distribution in the object. More modern reconstruction methods have attempted to eliminate this blur using common techniques to solve the inverse problem more correctly. In this sense, the problem of reconstructing images from Compton camera data is no more difficult than for more conventional emission tomography—the main differences arise in the details of the implementation and in the sheer amount of computation. Rather than providing an exhaustive description of the various methods proposed for Compton camera reconstruction, this section embeds the reconstruction problem into the relevant mathematical framework in a non-rigorous manner. In this way, the relationship among the various reconstruction methods from analytic inverses to iterative statistical methods is evident. However, while we have attempted to keep things simple, it is hardly possible to draw the various reconstruction methods together without introducing some Hilbert space concepts. The second disclaimer is that many shortcuts have been taken in order to tie the widely different reconstruction techniques together. As an example, while a Compton camera measures energy as opposed to scattering angle, the reconstructions presented in section E assume that scattering angle is the measured parameter.

## B. The Forward Problem

Assuming that  $\mathbf{x} = [x, y, z]$  describes a 3D location in a continuous source distribution  $f(\mathbf{x})$  and that  $\mathbf{y} = [\mathbf{d}_1, \mathbf{d}_2, E_1, E_2]$  is a vector describing event detection locations and energies in the first and second detectors, the following formulation relates the expected value  $g(\mathbf{y})$  of the projection measurements to the source distribution

$$g(\mathbf{y}) = (\mathcal{H}f)(\mathbf{y}) = \int_{\mathcal{X}} h(\mathbf{y}, \mathbf{x}) f(\mathbf{x}) d\mathbf{x}, \quad (24)$$

where the kernel of the integral equation  $h(\mathbf{y}, \mathbf{x})$  represents the conditional probability of detecting an event at location  $\mathbf{y}$  given that it was emitted at location  $\mathbf{x}$  in the source. This conditional probability density models the effect of scattering-angle uncertainty due to electronic noise and Doppler-broadening as well as any spatial resolution limitations of the first or second detector. Non-linear aspects of the problem such as object-dependent  $\gamma$ -ray attenuation, are incorporated into the definition of  $h(\mathbf{x}, \mathbf{y})$  or, as in the case of system deadtime, often ignored. The source and projection functions  $f$  and  $g$  are assumed to be elements of the Hilbert spaces of square-integrable functions  $L_2(\mathcal{X})$  and  $L_2(\mathcal{Y})$  (i.e.,  $\int_{\mathcal{Y}} g^2(\mathbf{y}) d\mathbf{y} < \infty$ ) over finite regions of space (Keener, 1988).

Because of the finite regions of support  $\mathcal{X}$  and  $\mathcal{Y}$  and the fact that  $h(\mathbf{y}, \mathbf{x})$  is bounded for all  $\mathbf{x}$  and  $\mathbf{y}$

$$\int_{\mathcal{X}} \int_{\mathcal{Y}} h^2(\mathbf{y}, \mathbf{x}) d\mathbf{y} d\mathbf{x} < \infty. \quad (25)$$

Equivalently,  $\mathcal{H}$  is a *Hilbert-Schmidt* operator and is therefore *compact*.<sup>5</sup>

Compact linear operators have many desirable properties. In particular, even though they are infinite-dimensional, they have an almost finite-dimensional quality and can be approximated to arbitrary accuracy by an appropriate sequence of degenerate linear operators or matrices. This justifies approximating the true, infinite-dimensional imaging problem by the matrix-vector approximation

$$\mathbf{g} = \mathbf{H}\mathbf{f} \quad (26)$$

where  $\mathbf{H}$  is a  $D \times B$  matrix approximating the operator  $\mathcal{H}$ ,  $\mathbf{f} = [f_1, \dots, f_B]^T$  represents a discrete approximation (e.g., pixel values) to the source distribution  $f$ , and  $\mathbf{g} = [g_1, \dots, g_D]^T$  is the expected number of events in each of  $D$  discrete detector channels. In spite of the desirable properties of compact linear operators, there are undesirable side-effects, which will become evident in the following sections.

In developing inversion methods to recover  $f$  from  $g$ , it is often useful to consider alternative representations. Note that equation (24) can also be represented by the following

$$g(\mathbf{y}) = \int_{\mathcal{Z} \times \mathcal{X}} h_2(\mathbf{y}, \mathbf{z}) h_1(\mathbf{z}, \mathbf{x}) f(\mathbf{x}) d\mathbf{x} d\mathbf{z} \quad (27)$$

where the intermediate decomposition is often convenient from the viewpoint of solving the inverse problem (e.g., the decomposition may break the forward problem into two problems whose solutions are known). Along the same lines, a transformation can also be applied to the projection data in order to *adapt* the measurements into a system of equations that can be solved more easily

$$r(\mathbf{z}) = \int_{\mathcal{Y}} \int_{\mathcal{X}} h_3(\mathbf{z}, \mathbf{y}) h_1(\mathbf{y}, \mathbf{x}) f(\mathbf{x}) d\mathbf{x} d\mathbf{y}, \quad (28)$$

where  $r(\mathbf{z})$  is the expected value of projection in the adapted geometry. Both techniques have been used extensively in developing Compton camera reconstructions.

Note that the above equations only represent the *expected value* of observing an event at a particular detector location. Quantum noise is significant in emission computed tomography and the primary reason for developing the Compton camera as an alternative to conventional SPECT where performance is limited by low efficiency. Unless the Compton advantage is overwhelming, one desires to use the measured data to estimate the source in a manner that is as statistically efficient as possible. In emission tomography, noise is dominated by counting statistics and it is common to embed the estimation problem within the framework of maximum-likelihood estimation using the conditionally Poisson likelihood function.

<sup>5</sup>More appropriately  $g$  and  $f$  should be restricted to the set of non-negative functions consistent with the fact that intensities must be non-negative; however, this would preclude the analytic solutions presented in Section E.

For continuous source and detector coordinates, the likelihood of observing a sequence of interactions with detector coordinates  $\tilde{\mathbf{y}}_n$  (as above  $\tilde{\mathbf{y}}$  includes the first and second detector locations and energies of the event) conditioned on the source distribution is given by

$$f(\{\tilde{\mathbf{y}}_n\}_{n=1}^{N_T} | f, T) = \prod_{n=1}^{N_T} g(\tilde{\mathbf{y}}_n) \exp \left[ - \int_{\mathbf{y}} g(\mathbf{y}) d\mathbf{y} \right], \quad (29)$$

where  $N_T$  is a Poisson distributed random variable denoting the total number of events observed in the time interval  $[0, T]$  and  $g(\mathbf{y})$ , the expected intensity of the projection data during the observation interval is a function of the source distribution  $f(\mathbf{x})$  as given by equation (1). Note that despite the fact that the source distribution may be a continuous function of location, there is never more than a finite number of measurements,  $N_T$ . Without restrictive conditions on the function space to which  $f$  belongs,  $f$  can never be recovered exactly from the measurements.

Somewhat more convenient to deal with from the viewpoint of image reconstruction is the likelihood function for the discrete formulation given by equation (26)

$$f(\tilde{\mathbf{g}}|\mathbf{f}) = \prod_{d=1}^D \frac{\left( \sum_{b=1}^B h_{db} f_b \right)^{\tilde{g}_d}}{\tilde{g}_d!} \exp \left( - \sum_{b=1}^B h_{db} f_b \right) \quad (30)$$

where  $\tilde{\mathbf{g}} = [\tilde{g}_1, \dots, \tilde{g}_D]^T$  represents the measured data  $\{\tilde{\mathbf{y}}_n\}_{n=1}^{N_T}$  binned into  $D$  detector channels.

Note that because the adapted geometries specified by equation (28) in practice apply a transformation to the measured projection data, they also change the likelihood function—introducing correlations among the adapted measurements.

### C. The Inverse Problem

Numerous techniques exist for developing inverses—or perhaps more appropriately, *pseudoinverses*—to the above integral equations. We first discuss a solution that has high relevance to both the continuous and discrete formulations of the problem.

Typically the expected value of the projections contain significant redundant information regarding the object—and this is certainly the case for the Compton camera. Without noise, the projection function  $g$  lies within the range of the system operator  $\mathcal{H}$  and therefore has unique corresponding source distribution  $f$ . However, the presence of noise will almost surely result in the measured projections  $\tilde{\mathbf{g}}$  being *inconsistent* or not lying entirely within the range of  $\mathcal{H}$ . Assuming the measurement variance is the same at each point in  $\tilde{\mathbf{g}}$ , for at least the finite-dimensional ( $\mathcal{H} = \mathbf{H}$ ) reconstruction problem, the Gauss-Markov theorem (Rao and Toutenburg, 1999) states that the linear, unbiased estimator having the lowest variance is given by

the least-squares solution, which can be written as (Keener, 1988)

$$\hat{f}_{LS} = (\mathcal{H}^* \mathcal{H})^{-1} \mathcal{H}^* \tilde{\mathbf{g}}, \quad (31)$$

where

$$(\mathcal{H}^* \tilde{\mathbf{g}})(\mathbf{x}) = \int_{\mathbf{y}} h(\mathbf{y}, \mathbf{x}) \tilde{g}(\mathbf{y}) d\mathbf{y} \quad (32)$$

is the adjoint or “backprojection” operation and  $(\mathcal{H}^* \mathcal{H})^{-1}$  is a self-adjoint operator that provides the “filtering” operation (no different than conventional filtered backprojection reconstruction in emission tomography).

Since the projection data are Poisson-distributed conditioned on the source distribution, the measurement noise in the measurement space is likely not equal at each point. For the situation in which this variance at each point in  $\tilde{\mathbf{g}}$  is known, the weighted least-squares solution is the best linear unbiased estimator for  $\hat{f}$

$$\hat{f}_{WLS} = (\mathcal{H}^* \mathcal{W} \mathcal{H})^{-1} \mathcal{H}^* \mathcal{W} \tilde{\mathbf{g}} \quad (33)$$

Here the appropriate weighting operator  $\mathcal{W}$  is given by the inverse of the covariance operator at each point in the projection data. For conditionally Poisson data, the kernel of  $\mathcal{W}$  would be

$$w(\mathbf{y}, \mathbf{y}') = \begin{cases} g^{-1}(\mathbf{y}) \delta(\mathbf{y} - \mathbf{y}') & g(\mathbf{y}) \neq 0 \\ 0 & \text{otherwise} \end{cases} \quad (34)$$

The weighted least-squares estimator essentially weights redundant data inversely with its uncertainty relative to the signal transfer characteristics  $\mathcal{H}$  and then applies an appropriately modified filter  $(\mathcal{H}^* \mathcal{W} \mathcal{H})^{-1}$  for deblurring.

Even though equations (31) and (33) are formal solutions of the forward problem, they have significant practical issues. As will be seen below, the stability of these solutions is poor, the finite set of measurements  $\{\tilde{\mathbf{y}}_n\}_{n=1}^{N_T}$  cannot completely specify  $f$ , and the estimates  $\hat{f}$  are not restricted to be non-negative. Nevertheless, these linear least-squares estimators have strong relationship to virtually all practical reconstruction methods as will be seen.

### D. Overview of Compton Reconstruction Methods

With the above background, it is convenient at this point to provide a brief history of Compton image reconstruction for the near-field or 3D medical imaging application. In the sections that follow, recent developments are examined in more detail.

In the early 1980's Singh and Doria explored the idea of a two-stage reconstruction (the forward problem represented symbolically by equation (27) (Singh and Doria, 1983). In their approach, each first detector element was considered as a “virtual pinhole” aperture. In the absence of the Compton encoding (equivalently, at scattering angle zero), the projection of the object onto the second detector through

each first detector element behaves as a pinhole projection of the object—albeit with different vignetting properties than a physical pinhole. For each first detector element their reconstruction recovered these pinhole projections using various iterative methods. The second stage reconstructed the 3D object distribution from the decoded pinhole projections.

Brechner and Singh (1990), and Hebert, *et al.* (1990) extended this work by noting that hemispherical second detectors centered on each first detector element could greatly simplify the reconstruction problem (the adapted geometry of equation [28]). The intersection of the cone ambiguity with a spherical second detector has a constant circular shape regardless of the cone direction. Equivalently, the “pinhole” projection of the object on this spherical surface is convolved with a rotationally-invariant function corresponding to the Compton ambiguity along with additional uncertainties in the scattering angle due to noise. This allowed use of the fast fourier transform (FFT) to improve the computational efficiency of part of the reconstruction through the use of its fast formula for circular convolutions. Hebert, *et al.* (1990), recognized the statistical inefficiency of the two-stage reconstruction and formulated the problem as one of maximum-likelihood estimation in which the 3D source distribution was estimated *directly* from the projection data.

The most significant issue in Compton camera reconstruction has proven to be computation, and more recently, several investigators have attempted to develop computationally efficient reconstructions. In particular, Rohe *et al.* (1997) has examined the point spread function (PSF) of the 3D backprojection of the coded data from a Compton camera consisting of concentric spherical first and second detectors. To the extent the backprojected PSF is spatially-invariant, the FFT and its corresponding fast convolution property for shift-invariant systems can be used to remove the blur in the backprojection. Sauve, *et al.* (1999) employed a multi-stage factorization of the system matrix  $\mathbf{H}$ —again using the idea of hemispherical second detectors—and proposed several iterative reconstruction methods based on this factorization. Wilderman (1999, 2001) has developed a list-mode maximum-likelihood reconstruction method, which as shown below, results in a significant computational advantage over approaches using binned projection data.

Finally, considerable progress has been made in the effort to develop analytic reconstruction methods (Cree and Bones, 1994; Basko *et al.*, 1998; Parra, 2000). While analytic methods generally have several disadvantages in comparison with their more general iterative counterparts, they are nevertheless important for the insight they bring to the Compton imaging problem and because they may provide practical reconstruction for specialized Compton imaging geometries.

## E. Direct or “Analytic” Solutions

A common method for finding an inverse operator for the above integral equations is to expand the forward operator in a set of orthogonal functions that separates or “diagonalizes” it (analogous to the matrix case). For example, complex exponentials are a complete set of orthonormal functions that diagonalize shift-invariant operators in Cartesian coordinates to provide the familiar fast convolution formula. Once the operator has been diagonalized, solution is straightforward, although practical application often requires finding a computationally efficient method for computing the appropriate transforms.

Any compact linear operator—and in particular the emission tomography problem—can be represented by the following expansion (Naylor and Sell, 1982)

$$\begin{aligned} g(\mathbf{y}) = (\mathcal{H}f)(\mathbf{y}) &= \int \sum_{\mathbf{x}, n=0}^{\infty} H_n u_n(\mathbf{y}) v_n^*(\mathbf{x}) f(\mathbf{x}) d\mathbf{x} \\ &= \sum_{n=0}^{\infty} H_n F_n u_n(\mathbf{y}), \end{aligned} \quad (35)$$

where

$$F_n = \int \sum_{\mathbf{x}} v_n^*(\mathbf{x}) f(\mathbf{x}) d\mathbf{x}. \quad (36)$$

with  $\{u_n(\mathbf{y})\}$  and  $\{v_n(\mathbf{x})\}$  sets of orthonormal functions that span the range and domain of the operator  $\mathcal{H}$ , respectively ( $v^*$  being the complex conjugate of  $v$ ). As noted in the previous section, compact linear operators are “nearly” finite-dimensional and the above decomposition is closely related to singular-value decomposition of the corresponding discrete approximation  $\mathbf{H}$  to the imaging system

$$\mathbf{H} = \sum_{n=1}^D H_n \mathbf{u}_n \mathbf{v}_n^T \quad (37)$$

where  $\{\mathbf{u}_n\}$  and  $\{\mathbf{v}_n\}$  are orthonormal sets of vectors playing the same role as functions  $u$  and  $v$ . In both cases the set of coefficients  $\{H_n\}$  is known as the *spectrum* of the operator.

Using the above expansion, and the orthonormality of  $\{u_n(\mathbf{y})\}$  and  $\{v_n(\mathbf{x})\}$ , i.e.

$$\int v_n^*(\mathbf{x}) v_m(\mathbf{x}) d\mathbf{x} = \begin{cases} 1 & n = m \\ 0 & \text{otherwise} \end{cases} \quad (38)$$

it is a simple matter to show that the inverse to the reconstruction problem can be approximated to arbitrary accuracy by the following series expansion

$$f(\mathbf{x}) \approx \sum_{n=0}^N H_n^{-1} G_n v_n(\mathbf{x}) \quad (39)$$

where

$$G_n = \int g(\mathbf{y}) u_n^*(\mathbf{y}) d\mathbf{y} \quad (40)$$

A most unfortunate property of compact linear operators—the one that essentially provides their close link

with finite-dimensional matrices—is that as  $N \rightarrow \infty$ , the spectral coefficients  $H_n \rightarrow 0$ . It is immediately evident from equation (38) that small changes in  $\mathbf{g}$  will induce arbitrarily large changes in the estimate of  $f$  for large enough  $N$ .<sup>6</sup> A common method of stabilizing the estimate, however, is to truncate the expansion at a value of  $N$  that provides an acceptable noise-fidelity tradeoff.

Several investigators have developed analytic reconstructions by finding decompositions of the form of equation (35) for specific adapted geometries. Three of these techniques are described in general terms below; refer to the corresponding articles to appreciate the details.

Cree and Bones (1994) develop a solution of the 3D source reconstruction problem from an adapted geometry consisting of parallel, planar first- and second-detectors with a parallel-hole collimator interposed between the two such that only scattered photons travelling orthogonal to detector plane are recorded.<sup>7</sup> Using the fact that the Fourier transform can be used to diagonalize a spatially-invariant convolution, in conjunction with the Hankel transform, they develop an inversion formula which shows that by collecting all scattering angles, the 3D source distribution can be recovered as the spatial extent of the detectors increases without limit. Practically, however, only limited-angle tomography is achievable with detectors of finite extent and the use of a parallel-hole collimator (either virtual or real) between the detectors results in an unacceptable loss of efficiency. Nevertheless, they suggest techniques for circumventing these limitations.

The methods of Parra and of Basko *et al.* are similar in two significant ways. First, as in the work of Singh and Doria, they adapt the geometry of the problem to consider each first detector element to be at the center of a spherical second detector. The second similarity, is that spherical harmonics are used as the sets of orthogonal functions to diagonalize the operator. Noting that when projected onto such a spherical second detector, the convolution kernel is rotationally-invariant depending only on the angle between the incident and scattered photon, the following expansion can be used

$$\begin{aligned} g(\theta, \Omega_2) &= \sum_{n=0}^{\infty} H_n(\theta) \sum_{m=-n}^n Y_{nm}(\Omega_2) P_{nm}, \\ P_{nm} &= \int_{\Omega} p(\Omega_1) Y_{nm}^*(\Omega_1) d\Omega_1, \end{aligned} \quad (41)$$

where  $\Omega = (\omega, \phi)$  is a direction vector with  $\omega \in [0, 2\pi]$  azimuth and  $\phi \in [0, \pi]$  elevation,  $p(\Omega)$  is the projection of the unscattered object distribution through the virtual pinhole,  $Y_{nm}(\Omega)$  are spherical harmonics of degree  $n$  and order  $m$ , and the spectral coefficients  $H_n(\theta)$  depend on the

<sup>6</sup>Consider the effect of the ramp filter for conventional emission tomography as the spatial frequency becomes large.

<sup>7</sup>For a Compton camera consisting of parallel first- and second-detectors, the kernel  $h_3(z, y)$  in this case simply eliminates events in which the scattered photon does not travel perpendicularly to the detectors.

scattering angle  $\theta$ . The above decomposition allow the expansion coefficients  $P_{nm}$  of the pinhole projections  $p(\Omega)$  to be related to the expansion coefficients of the projection data at each scattering angle

$$P_{mn} H_n(\theta) = G_{mn}(\theta). \quad (42)$$

Using these ideas, Basko *et al.* propose the following reconstruction procedure:

1. Transform Compton camera data at each scattering angle into corresponding projections on a spherical detector concentric with each first detector element.
2. Calculate expansion coefficients  $G_{nm}(\theta)$ .
3. Compute the coefficients

$$G_{nm}\left(\frac{\pi}{2}\right) = \frac{H_n\left(\frac{\pi}{2}\right)}{H_n(\theta)} G_{nm}(\theta) \quad (43)$$

and then

$$g\left(\frac{\pi}{2}, \Omega_1\right) \approx \sum_{n=0}^N \sum_{m=-n}^n G_{nm}\left(\frac{\pi}{2}\right) Y_{nm}^*(\Omega_1). \quad (44)$$

4. Noting that the  $g(\pi/2, \Omega_1)$  form a set of (nearly) plane integrals through the 3D source distribution, the image can be reconstructed using the inverse 3D Radon transform (Natterer, 1986) with the assumption that the set of first detector locations or “cone-beam vertices” appropriately sample the Radon domain.<sup>8</sup>

Parra proposes several methods based loosely on the following procedure:

1. “Backproject” the data at each scattering angle onto a single spherical detector; i.e.

$$r(\Omega_1) = \int g(\theta, \Omega_2) h(\Omega_2, \Omega_1, \theta) d\Omega_2 d\theta. \quad (45)$$

Alternatively, the spherical harmonic expansion coefficients of the backprojected data can be expressed as

$$R_{nm} = \int_0^\pi H_n(\theta) G_{nm}(\theta) d\theta. \quad (46)$$

2. Apply the appropriate inverse filter to the backprojected data in order to recover the corresponding pinhole projections. This can be written in the following way in the transform domain

$$P_{nm} = R_{nm} / \int_0^\pi H_n^2(\theta) d\theta. \quad (47)$$

The operation can either be applied in the spherical harmonic domain or the transformed filter can be used for spherical deconvolution in the spatial domain.

3. From the  $P_{nm}$ , the pinhole projections  $p(\Omega)$  can be recovered and used in a cone-beam image reconstruction technique in order to estimate the 3D source distribution.

<sup>8</sup>Note that for the case of the real Compton camera,  $g(\pi/2, \Omega)$  actually form weighted plane integrals through the object with the weight decreasing approximately as the square of the distance of the source location from the scattering detector.

Just as in filtered backprojection for reconstruction of conventional emission tomography images, there are numerous variations of the above approaches that differ mainly in the order and the domain in which the operations are performed.

Both Parra and Basko note the redundancy in the Compton projection data and Parra notes that different weighting of the angular information can lead to reconstructions having different invertibility or noise properties. Generally, a wide variety of non-negative weight functions  $w(\theta)$  can be used

$$P_{nm} = \frac{\int_0^\pi w(\theta) G_{nm}(\theta) d\theta}{\int_0^\pi w(\theta) H_n(\theta) d\theta} \quad (48)$$

with the following choice being, perhaps especially significant for handling the fact that projection information at different scattering angles has different intrinsic uncertainties

$$P_{nm} = \frac{\int_0^\pi H_n(\theta) k(\theta) G_{nm}(\theta) d\theta}{\int_0^\pi H_n^2(\theta) k(\theta) d\theta} \quad (49)$$

where  $k(\theta)$  is a function that weights the quality of the data at each scattering angle based on the inverse of its uncertainty and  $H_n(\theta)$  quantifies how much “signal” is present in the projections. This has an obvious relationship with the weighted least-squares estimate of equation (10) but the class of admissible weighting functions is smaller and the estimator not as statistically efficient.

In spite of the aesthetics of analytic inversion methods, they have significant limitations:

1. It is difficult to handle  $\gamma$ -ray attenuation (especially non-uniform attenuation) because the operator  $\mathcal{H}$ , and therefore the orthogonal function expansion that diagonalizes it, becomes object-dependent.
2. Although some statistical weighting of redundant measurements can be done, it is typically less adequate than that provided by readily available alternatives such as maximum likelihood estimators.
3. Existence of an analytic inverse does not imply computational efficiency. Operations done in the spectral domain require the existence of a fast transform to be practical.
4. Analytic inverses typically depend on geometric adaptations of the imaging geometry for which the measurements often do not provide complete data (consider the case of a truncated second detector where measurements are not collected over  $4\pi$  steradians as required for the above expansions). While iterative procedures can often be used to fill in this “missing” information, one of the reasons direct solutions are sought is to *avoid* iterative methods.
5. It is difficult to constrain the reconstruction to lie within a function space appropriate to source distributions (i.e., the set of *non-negative*, square-integrable functions on

$\mathcal{X}$ ) other than by applying a trivial “clipping” operation (if  $f(\mathbf{x}) < 0$  then set  $f(\mathbf{x}) = 0$ ). Such estimates are in general not constrained solutions of the desired problem (e.g., a solution to the weighted least-squares problem subject to  $\hat{f}$  being non-negative)

## F. Statistically Motivated Solutions

By using an iterative reconstruction procedure virtually all of the aforementioned limitations can be eliminated. Iterative methods allow simple incorporation of object attenuation, do not require restrictive system geometries, and can incorporate measurement uncertainty and constraints on the source distribution in a straightforward manner. In recent years, maximum likelihood (ML) estimation and the related *penalized* likelihood estimation have found widespread use in emission tomography for these reasons.

Recalling the discrete version of the likelihood function given by equation (30), the maximum likelihood (ML) estimator chooses the unknown source distribution  $\hat{\mathbf{f}}$  that maximizes this function

$$\hat{\mathbf{f}} = \arg \max_{\mathbf{f}} f(\mathbf{g}|\mathbf{f}). \quad (50)$$

The ML estimate is typically found by differentiating the log-likelihood and solving the following system of equations subject to the condition  $f_b \geq 0$  for  $b = 1, \dots, B$

$$\sum_{d=1}^D \frac{g_d h_{db}}{\sum_b h_{db} f_b} - \sum_{d=1}^D h_{db} = 0, \quad (51)$$

that must be done iteratively.

With certain restrictions (e.g., inverses must exist), the ML estimate  $\hat{\mathbf{f}}$  satisfies

$$\hat{\mathbf{f}} = (\mathbf{H}^T \mathbf{W} \mathbf{H})^{-1} \mathbf{H}^T \mathbf{W} \mathbf{g} \quad (52)$$

subject to the constraint that all elements of the vector  $\hat{\mathbf{f}}$  are non-negative. The weighting matrix  $\mathbf{W}$  is given by the inverse of the *estimate* of the measurement covariance, i.e.,

$$\mathbf{W} = \text{diag}^{-1}(\hat{\mathbf{H}}\hat{\mathbf{f}}). \quad (53)$$

While it proves to be difficult to calculate the ML estimate using these equations (due to non-negativity constraints and existence of the inverses) its relation with the weighted least-squares estimate given by equation (33) should be clear. The significant difference is that the estimated data covariance is used because the actual covariance is unknown.

It would be difficult to develop a direct reconstruction method based on expansion of either equation (33) or (52) because the orthogonal functions necessary for diagonalization depend on the object or the measurements. Moreover, for the ML estimator, the estimate  $\hat{\mathbf{f}}$  appears on both sides of the equation. Fortunately, numerous iterative solution methods can be employed. The iterative expectation-maximization or EM-algorithm with the “usual” complete

data space for emission tomography (Shepp and Vardi, 1982; Fessler et al., 1993) is convenient—if not particularly fast—for this problem

$$\hat{f}_b^{(k+1)} = \frac{\hat{f}_b^{(k)}}{\sum_d h_{db}} \sum_{d=1}^D \frac{g_d h_{db}}{\sum_b h_{db} \hat{f}_b^{(k)}} \quad (54)$$

with the superscript  $k$  representing the iteration number.

Besides its relatively slow convergence rate, the above formulation of the algorithm suffers from an immediate problem:  $D$ , the number of possible detector elements in the vector  $\mathbf{g}$  can be enormous—which, by the way, is also a significant problem for the analytic methods. A practical Compton camera might have  $2^{16}$  first-detector elements, an equal number of second-detector elements, and  $2^8$  energy channels, resulting in approximately  $10^{12}$  possible detector bins.

A typical dataset for this camera might likely have only  $10^8$  or so events. Obviously, most of the possible detector bins will contain zero, and for this case, an alternative formulation of the likelihood—the list-mode likelihood function—offers significant computational advantages (Barrett et al., 1997; Wilderman et al., 1999; Wilderman et al., 2001). While the EM algorithm can be rederived using equation (29) as a starting point, the computational advantage is immediately evident if, as above, we assume a very large number of possible detector channels  $D$ , most of them containing zero. Note that the above iteration can also be written as

$$\hat{f}_b^{(k+1)} = \frac{\hat{f}_b^{(k)}}{\sum_d h_{db}} \sum_{\{d: g_d \neq 0\}} \frac{g_d h_{db}}{\sum_b h_{db} \hat{f}_b^{(k)}} \quad (55)$$

with the result that only the elements of the matrix  $\mathbf{H}$  corresponding to nonzero  $g_d$  are needed and the sum ranges only over the number of events rather than all possible detector elements. The disadvantage of list-mode likelihood is that its complexity increases with the number of collected events. Nevertheless, it currently represents one of the more practical techniques for reconstructing Compton camera data and it incorporates the statistical uncertainties in the data in a way that will asymptotically achieve the performance predicted by Cramér-Rao lower bound.

### G. Regularization

Although, the scope of this section does not allow detailed treatment, the imaging problem is ill-posed. For the continuous formulation, small changes in the data can have an arbitrarily large effect on the reconstructions. Even in the finite-dimensional approximation, the matrix  $\mathbf{H}$  is typically very poorly conditioned and the reconstruction problem *practically ill-posed*. In all cases, unbiased estimation is not possible and some bias needs to be incorporated into the reconstruction in order to reduce variance to acceptable levels (see Section III).

In conventional filtered backprojection, this biasing is accomplished by applying a window function to the ramp

filter. Variance in reconstructed images is reduced with the undesirable side effect of increased image blur. Similar methods can be used in the linear least-squares estimators presented above as well as for the methods of Cree, Basko, and Parra. Other methods of reducing variance are to truncate the series expansion in equation (38) at a value of  $N$  that gives an acceptable resolution-noise tradeoff or by stopping an iterative reconstruction technique before convergence. The latter method is very often used to regularize maximum likelihood reconstructions.

The maximum likelihood estimator presented in the previous section has an additional advantage over the linear least-squares solutions of equations (31) and (33). The solutions are automatically constrained to be non-negative at each point in the reconstructed image. This constraint actually introduces a bias that significantly reduces variance in regions of the reconstructed image corresponding to low activity regions of the source.

Penalized likelihood estimation is becoming an increasingly popular method for regularization. A penalized maximum likelihood estimator is obtained by augmenting the likelihood with a penalty function

$$\hat{\mathbf{f}} = \arg \max_{\mathbf{f}} f(\mathbf{g}|\mathbf{f}) - \alpha R(\mathbf{f}), \quad (56)$$

where  $R$  is a function penalizing undesirable characteristics of the reconstructed image such as large pixel-to-pixel intensity variations (or roughness) and the parameter  $\alpha$  controls the degree to which the estimate corresponds to the measurements or to the penalty. Because its gradient is a linear function of  $\mathbf{f}$ , a common choice for  $R$  in emission tomography problems is a quadratic roughness penalty

$$R(\mathbf{f}) = \mathbf{f}^T \mathbf{R} \mathbf{f} \quad (57)$$

where  $\mathbf{R}$  is a matrix that forms the difference of each pixel with its nearest neighbors. Although penalized likelihood estimation is becoming popular—and is a close parallel to Bayesian estimation using the maximum *a posteriori* (MAP) estimator—spatial resolution properties at each point in the reconstructed object can vary (Stayman and Fessler, 2002).

For more detailed treatments on regularization and the noise-resolution tradeoff, refer to (Demoment, 1989; Hero et al., 1996; Fessler and Rogers, 1996; and Qi and Huesman, 2001).

## V. HARDWARE AND EXPERIMENTAL RESULTS

### A. Silicon Pad Detectors

As described at the beginning of this chapter, the work of Singh and his colleagues was based on a pixelated germanium scattering detector. This selection was made primarily on the very high energy resolution that could be

obtained (850 eV FWHM) combined with the fact that the sizable effects of Doppler broadening were not appreciated at that time. More recently, Du (Du *et al.*, 2001) has reported design of a Compton camera for high energies based on 3D CZT detectors, and the group at the Naval Research Laboratories (Kroeger *et al.*, 1999; Wulf *et al.*, 2002) has described germanium strip detectors for the Advanced Compton Telescope application. Because of the large uncertainties in scattering angle related to Doppler broadening for germanium, the cost and cooling requirements associated with germanium detectors, and the desire to maximize the probability of single scattering followed by escape from the first detector, current hardware development at the University of Michigan has focused on the development of low-noise silicon pad detectors (Weilhammer *et al.*, 1996). The most recent version of this detector and its readout electronics is shown in Figure 20 and fully described by Meier *et al.* (2000). The detector itself is 300- $\mu\text{m}$  thick and consists of 256 1.4  $\times$  1.4 mm pixels in an 8  $\times$  32 array. The total sensitive area of the detector is 11.2 mm  $\times$  44.8 mm. The detector is AC coupled, and the pixel connections to wire bond pads on the long edges are accomplished by means of a fan-out structure in a second metal layer. The front-end readout is composed of eight 32-channel VA/TA chip sets manufactured by IDEAS<sup>2</sup>.

The VA preamplifier is set to a 2- $\mu\text{s}$  shaping time, whereas the TA has a short shaping time and generates a fast readout trigger pulse for events above a computer-set threshold. Each chip set reads out 32 channels for a valid trigger event. This detector and readout is identical to that described by LeBlanc (1999; LeBlanc *et al.*, 1998) and Hua (2000), except that detector and electronics are mounted on 10- $\mu\text{m}$ -thick kapton foil and an improved version of the TA trigger generator is used in which the threshold values for all pads can be aligned to the same gamma-ray energy. The kapton foil printed circuit represents an attempt to mini-

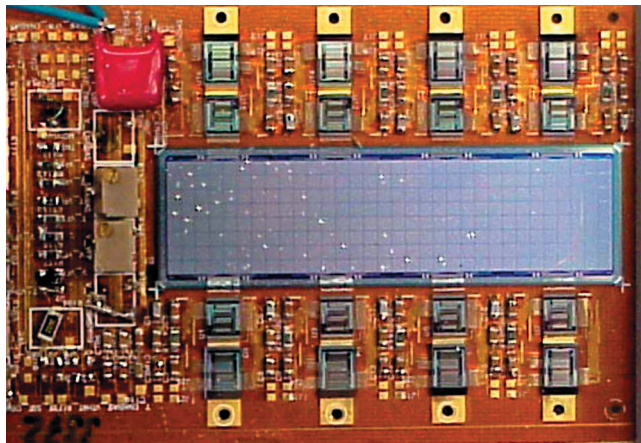


FIGURE 20 Silicon pad sensor and VA/TA 32-channel readout chips mounted on 10- $\mu\text{m}$ -thick kapton foil hybrid board (From Meier *et al.*, 2000, © 2000 IEEE.)

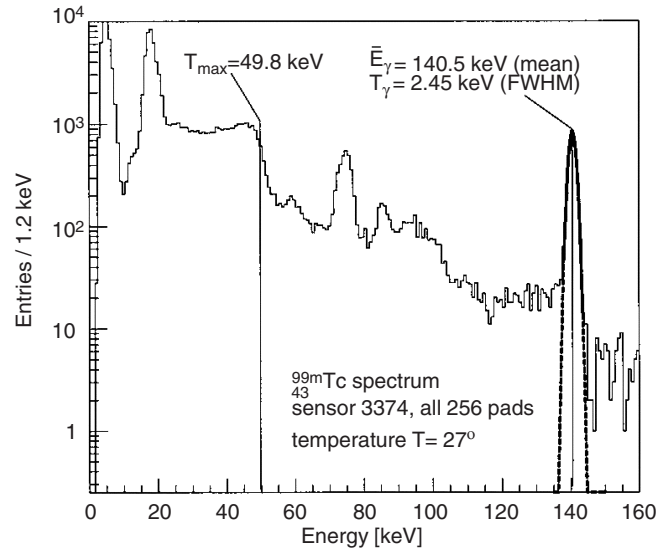


FIGURE 21 Energy spectrum for  $^{99\text{m}}\text{Tc}$  summed over all pads. A 15-keV threshold was set just above the noise level. (From Meier *et al.*, 2000, ©2000 IEEE.)

mize nondetector mass in the first-detector assembly. Trigger times for all pads have a Gaussian distribution with a width of 17 ns FWHM without any compensation for differences in mean channel delay times or pulse height variation. A composite  $^{99\text{m}}\text{Tc}$  spectrum for all pads is shown in Figure 21. A 15-keV trigger threshold could be set above the noise, and this permits triggering on 56° scattering events for  $^{99\text{m}}\text{Tc}$  and 20° events for  $^{131}\text{I}$ .

The energy resolution averaged over all pads was 2.45 keV for  $^{99\text{m}}\text{Tc}$ . These detectors depleted at 55 V and exhibited a room-temperature leakage current averaging approximately 225 nA/256 pads at a bias of 60V. This resolution is less than desired; however, these detectors are certainly adequate for investigating Compton imaging in a prototype device. Measurements on a variation of this detector yielded noise values approaching 900 eV with the same readout chips.

### B. C-Sprint

It is absolutely essential to confirm lower-bound and observer predictions of Compton camera performance experimentally. This is necessary to validate the system model used for performance calculation and for the image reconstruction. For this purpose, a silicon detector similar to that described has been combined with a single-photon ring tomograph (SPRINT) (Rogers *et al.*, 1982) to form a prototype Compton camera, referred to as C-SPRINT (LeBlanc, Bai, *et al.*, 1999).

SPRINT is composed of 11 modular NaI(Tl) scintillation cameras arranged in a 50-cm-diameter ring. Scintillator thickness is 13 mm, and the useful width of the detector ring is approximately 11 cm. The spatial resolution of the cameras

is 3 mm FWHM. The silicon pad detector is located on-axis and is mounted on an optical bench to permit adjusting its axial position, as illustrated in Figure 22. The principal advantage of this ring geometry is that with appropriate shielding of the second detector ring one can use high activity sources with only a single silicon detector to obtain statistically significant data in reasonable collection times without

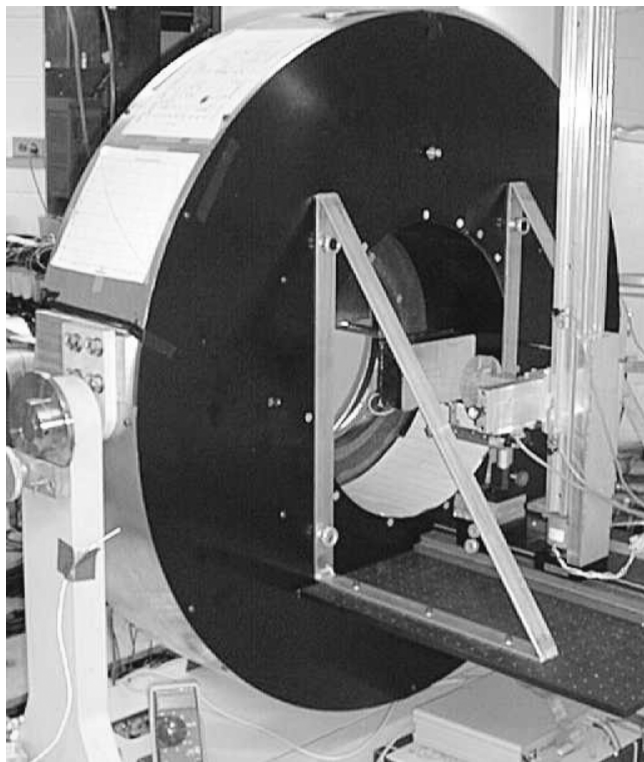


FIGURE 22 C-SPRINT. Si pad detector is on axis at the front edge of the NaI detector ring and disk phantom is 11 cm in front of the pad detector. (From LeBlanc, Bai *et al.*, 1999, ©1999 IEEE.)

TABLE 2 Key system Parameters for C-SPRINT

Parameter	$^{99m}\text{Tc}$	$^{131}\text{I}$
Resolution for summed energy (FWHM)	17 keV (12%)	43 keV (12%)
Coincidence resolving time (ns, FWHM)	140	70
Coincidence window (ns) <sup>a</sup>	90	90
Measured detection sensitivity <sup>b</sup>	$1.8 \times 10^{-7}$	$1.2 \times 10^{-6}$

<sup>a</sup>The maximum coincidence window is hardware-limited at present to 90 ns. From Le Blanc (1999).

<sup>b</sup>Sensitivity is for an on-axis point source at 11 cm.

saturating the second detector. The key system parameters are summarized in Table 2, and details of system calibration and performance can be found in Le Blanc (1999).

The energy and timing resolution in Table 2 are primarily determined by the scintillation detector. Although detection sensitivity is substantially less than the expected sensitivity after correcting for known problems, including dead time, nonuniform silicon detector thresholds, and narrow coincidence window, it was sufficient to acquire image data as described next.

### 1. Planar Images

Images of isolated point sources of  $^{99m}\text{Tc}$  and  $^{131}\text{I}$  from C-SPRINT are shown in Figure 23. Images were reconstructed using 200 iterations of unregularized list-mode likelihood (Wilderman *et al.*, 2001). These two point source images clearly demonstrate the effect of gamma-ray energy on spatial resolution. The small side-lobe in the Tc image is unexplained. Because the list-mode likelihood algorithm enforces a positivity constraint, an isolated point source image is an overoptimistic measure of imaging performance. For this reason  $^{99m}\text{Tc}$  and  $^{131}\text{I}$  images for point sources superimposed on a 7.5-cm-diameter uniform disk source and

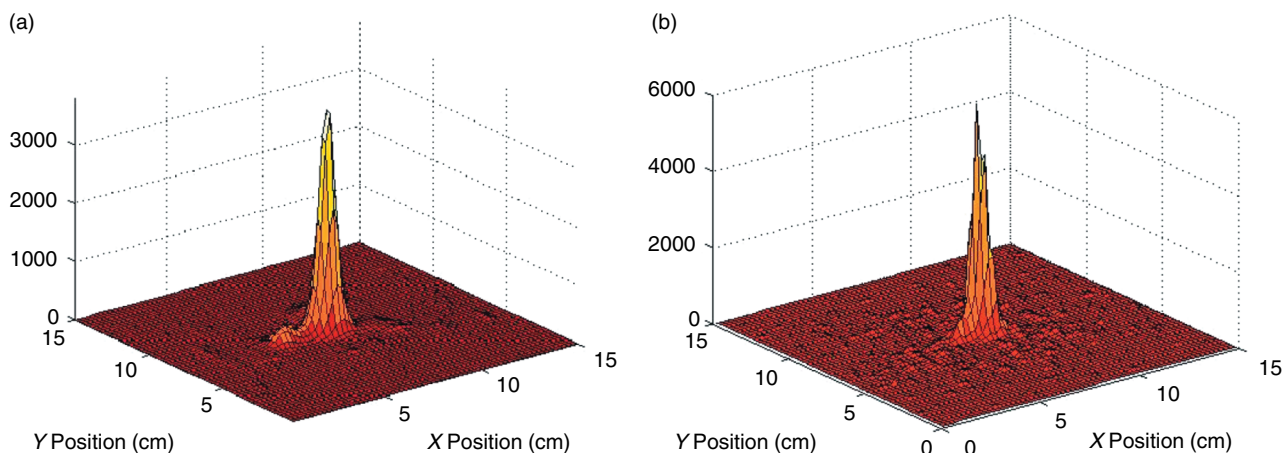


FIGURE 23 (a)  $^{99m}\text{Tc}$  point source at 11 cm, 8.2 mm FWHM. (b)  $^{131}\text{I}$  point source at 11 cm, 6.5 mm FWHM. 100 K counts each. (From LeBlanc, 1999, ©1999 JW LeBlanc.)

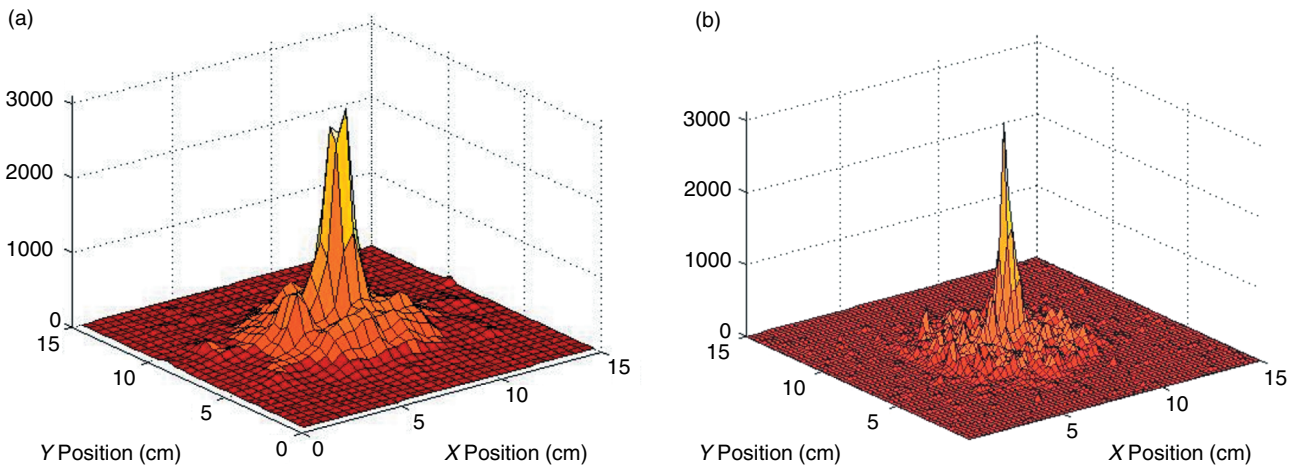


FIGURE 24 (a)  $^{99\text{m}}\text{Tc}$  point source superimposed on a 7.5-cm-diameter uniform disk at 11 cm, FWHM = 11.7 mm.  
 (b)  $^{131}\text{I}$  point source superimposed on Monte Carlo-generated disk background at 11 cm, FWHM = 5.9 mm.  
 (From LeBlanc, 1999, ©1999 J. W. LeBlanc.)

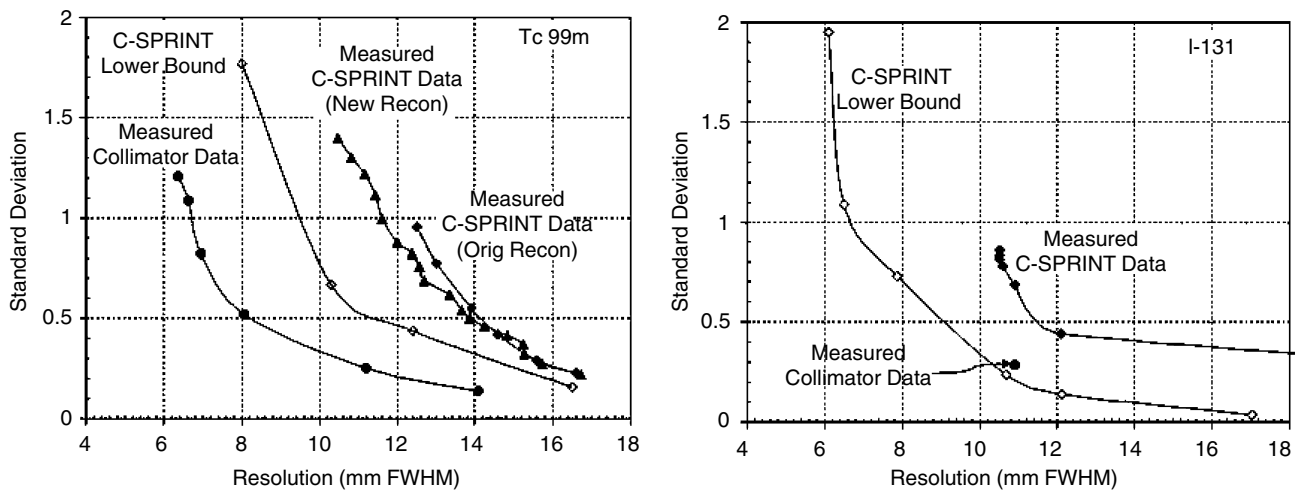


FIGURE 25 Standard deviation in center pixel normalized to the total number of detected photons versus FWHM spatial resolution for  $^{99\text{m}}\text{Tc}$  and  $^{131}\text{I}$  point sources on a uniform 7.5 cm diameter disk background. (Adapted from LeBlanc, 1999; LeBlanc, Bai, *et al.*, 1999; ©1999 JW LeBlanc & IEEE.)

reconstructed with 200 iterations are shown in Figure 24. For  $^{99\text{m}}\text{Tc}$ , 77,590 counts came from the 2.5-mm-diameter point source and 30,356 counts came from the disk. The data sets were acquired separately and then combined. In the case of  $^{131}\text{I}$ , 50,000 counts were acquired from the point source and combined with 100,000 counts from a simulated disk source. The spatial resolution for all images was estimated from a 2D least squares fit to a Gaussian plus background.

## 2. Variance/Resolution Results

In order to compare the experimental results with predictions derived from the uniform bound calculations (see Section III A), variance in the central pixel computed

from 10 realizations of experimental data is plotted in Figures 25 and 26 as a function of spatial resolution for C-SPRINT and a collimated Anger camera. This was done for both  $^{99\text{m}}\text{Tc}$  and  $^{131}\text{I}$  point sources on a 7.5-cm-diameter disk background spaced 11 cm from the first detector. FWHM and spectral resolution are both used as measures of resolution. Spectral resolution is defined in Eq. (58) (Lecomte *et al.*, 1984) where  $f(x)$  is the point response function. It is a useful additional measure of resolution because it is sensitive to the overall shape of the response function including the tails. Spectral resolution and FWHM for the uniform bound calculations are calculated from the mean gradient image (Section IIIA2).

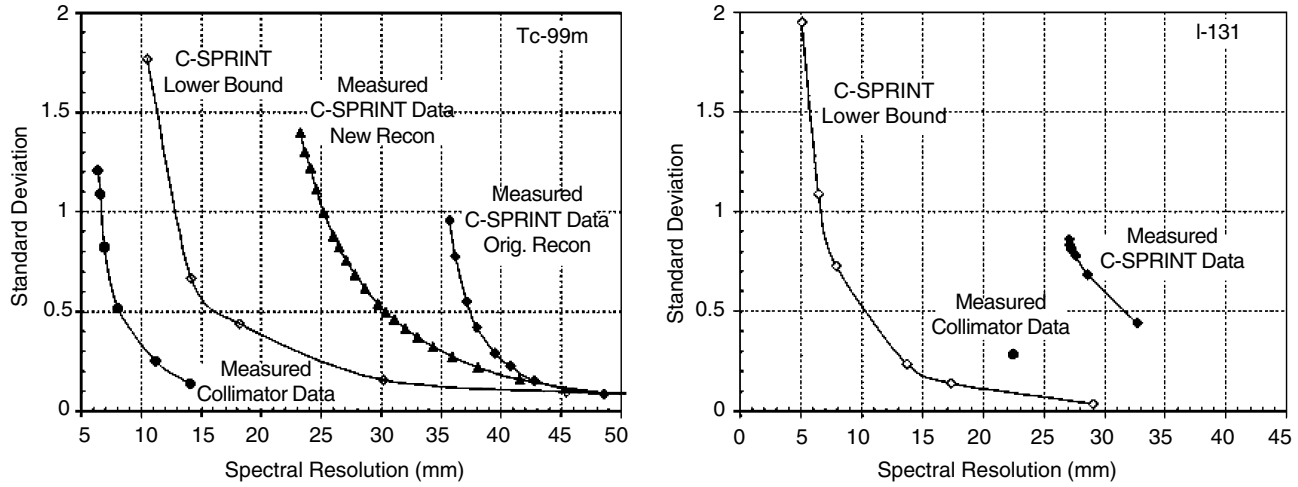


**FIGURE 26** Same as Figure 25 except plotted as a function of spectral resolution to emphasize the effect of the tails of the point response function. (Adapted from LeBlanc, 1999; LeBlanc, Bai, *et al.*, 1999; ©1999 JW LeBlanc & IEEE.)

$$R_s = \frac{\left[ \int_x f(x) dx \right]^2}{\int_x [f(x)]^2 dx} \quad (58)$$

Recall that the uniform lower bound on variance is the variance in a given object parameter predicted for the maximum-likelihood estimator for a specified imaging system. Spatial resolution for the bound curve is implicitly governed by an identity matrix penalty function. Bound computation used measured system parameters for C-SPRINT, including actual system geometry, first-detector noise and Doppler broadening, and spatial resolution for first and second detectors excluding depth of interaction. For the Anger camera and collimator, measured point source responses were used.

The spatial resolution for the experimental data was varied by varying the number of iterations of the list-mode ML algorithm. For <sup>99m</sup>Tc, the variance in the C-SPRINT image is computed from 10 realizations consisting of 10,000 events from the point source and 7759 events from the disk source. The variance for the collimator is computed from 20 realizations, and spatial resolution was varied by varying the number of iterations of a maximum likelihood-expectation maximum (ML-EM) deconvolution algorithm. For the <sup>131</sup>I curves each realization consisted of 10,000 events from a measured point source and 10,000 events from a Monte Carlo-simulated disk source. Again, 10 realizations were used for the C-SPRINT data and 20 realizations for the iodine collimator. No attempt was made to deconvolve the iodine point source data because of the structure in the tails of the response function arising from septal penetration.

Two versions of the list-mode likelihood algorithm were used to reconstruct the <sup>99m</sup>Tc images. The first, (Original Recon) was that described by Wilderman *et al.* (2001) in

which effects of finite resolution were approximated by back-projecting a central cone for the mean scattering angle and two neighboring cones with Gaussian-weighted amplitude at  $\pm \Delta\theta_s$ . The newer reconstruction weights the back-projected central cone with the sum of two Gaussians that approximates the true angular uncertainty. This function is truncated at approximately 5% of peak amplitude.

Figures 25 and 26 must be interpreted with caution because, in general, the shapes of the mean gradient image obtained from the bound calculation and the reconstructed point response functions will be different. Sensitivity to shape is particularly evident when comparing the new and original reconstructions of the Tc response function. When resolution is measured by FWHM, a relatively minor improvement is indicated. However, when spectral resolution is used as the metric, the new algorithm gives substantial improvement that is consistent with substantial reduction in the tails of the response function. Both the bound and experimental data for <sup>131</sup>I demonstrate the improved Compton camera performance at higher energy, both in the absolute sense and in comparison to the iodine collimator. Finally, it is quite evident that the experimental results differ substantially from the lower bound and that this difference is greater when spectral resolution, as opposed to FWHM, is used as a metric. This difference may arise from either the image reconstruction algorithm or from using an incorrect system model for the bound calculation. It is clearly important to resolve this question in order to be able to predict Compton camera performance and its dependence on system design parameters.

### C. Scintillation Drift Chambers as Compton Cameras

Up to this point we have focused on the use of solid-state detectors, and in particular silicon pixel detectors, for the

Compton camera application. However, in one of the first pioneering efforts devoted to the subject, Todd, Nightingale, and Everett (1977) mention gas detectors as a possible alternative for medical Compton imaging. Later, Fujieda and Perez-Mendez (1987) conclude that noble gas electroluminescence drift chambers have an advantage over scintillators and semi-conductor detectors in Compton camera design due to their combination of fine position resolution, good energy resolution, and large field of view. Since these first publications, several noble gas detector designs for Compton imaging have been proposed, including a liquid-xenon drift chamber, two-phase emission camera, and high-pressure xenon electroluminescence detector (Chen and Bolozdynya, 1995). The idea to use liquid xenon (LXe) for SPECT Compton cameras has been rejected because of the relatively poor energy resolution provided by LXe at the lower energies of interest in nuclear medicine. Large fluctuations in the small number of  $\delta$ -electrons created along tracks of ionization particles in LXe determine the intrinsic resolution of these detectors. For energies  $>1$  MeV, the energy resolution of LXe ionization detectors is approximately 5% FWHM, and the idea of a LXe Compton telescope proposed by Alvarez (Alvarez *et al.*, 1973) can be realized for astrophysics gamma-ray imaging (Aprile *et al.*, 1998).

Compton-scattered 140-keV gamma rays generate small signals with a maximum energy of 50 keV and average energy of approximately 30 keV. For this reason low-threshold electroluminescence noble gas detectors attract attention. The product of approximately 20 years of research, a scintillation drift chamber (SDC) with 3D position sensitivity has been developed (Bolozdynya, Egorov, *et al.*, 1997b). The SDC is triggered by fast scintillation signals arising at the moment of gamma-ray interaction with pressurized xenon. The readout system of this detector is able to determine 3D coordinates and deposited energy of several point-like ionization clusters occurring in the sensitive volume. The design of the SDC is described in detail in Bolozdynya (Chapter 18 in this volume), where it is shown that electroluminescence (EL) detectors benefit from the intrinsic signal amplification at low energy deposition. Because of this gain, the energy resolution of EL detectors is not limited by the input capacitance at the preamplifier, as is the case for solid-state detectors (see Section II B) or ionization chambers in which microphonic noise poses an additional problem. For this reason, the energy resolution of EL detectors of approximately  $1000\text{ cm}^2$  in area is comparable to the energy resolution of room-temperature semiconductor detectors with an area of approximately  $1\text{ cm}^2$ .

A schematic design of an SDC working as a Compton camera is shown in Figure 27. A single gamma quantum absorbed in noble gas may produce a few ionization clusters (vertices) resulting from photoabsorption of the gamma quantum, photoabsorption of the 29.7- and 33.8-keV fluorescent photons emitted by excited xenon atoms, Compton

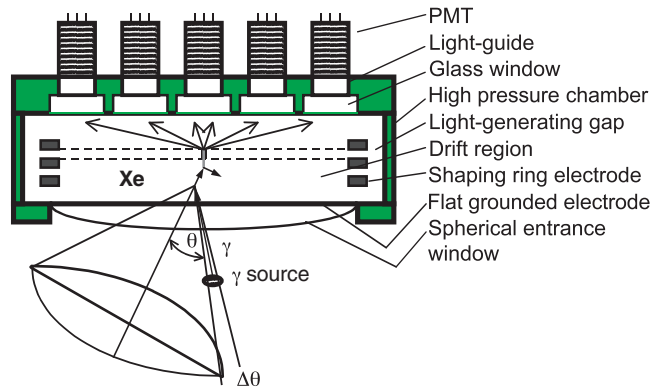


FIGURE 27 Schematic diagram of a scintillation drift chamber. (From Bolozdynya *et al.*, 1997b, © 1997 IEEE.)

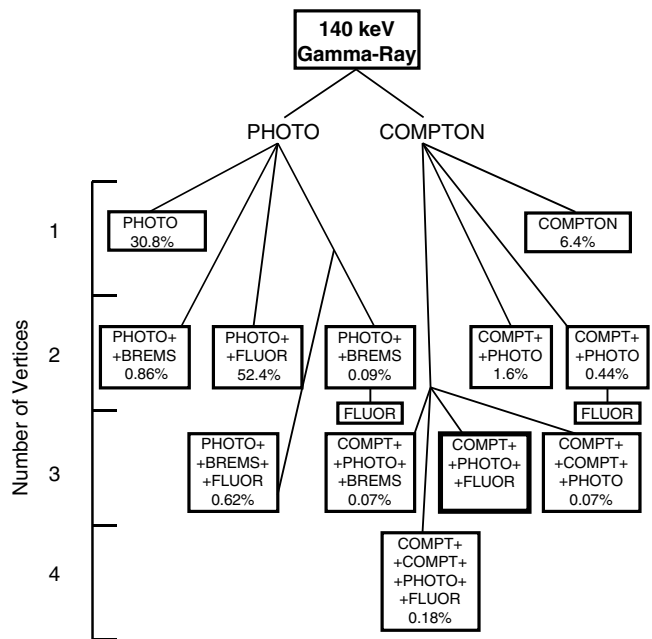
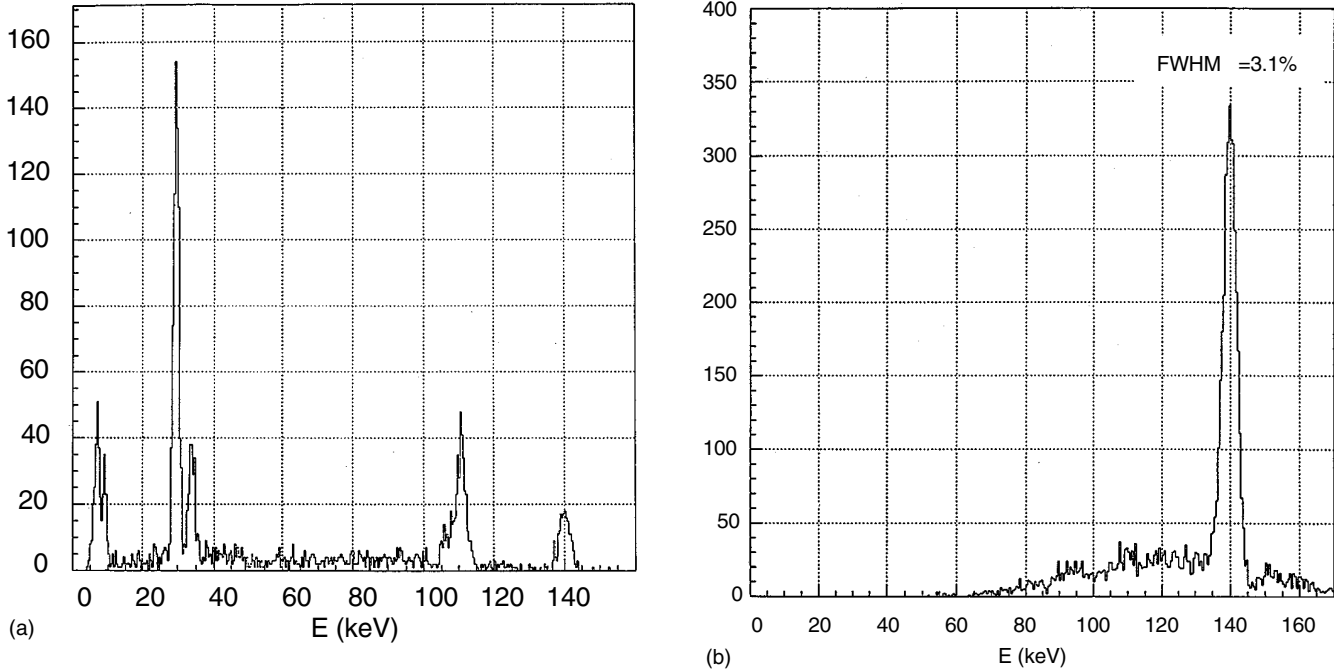


FIGURE 28 Probability of different interaction sequences for  $^{99m}\text{Tc}$  in a 20-bar xenon chamber.

scattering of the gamma quantum, and photoabsorption of the Compton scattered or Bremsstrahlung photons.

Possible scenarios of 140-keV gamma-ray interactions with a 20-bar xenon SDC filling are illustrated in Figure 28. The probability of each process is shown as a percentage of the number of incident gamma rays entering the SDC along the axis of the device. One can see that three-vertex events contain the dominant portion of Compton interactions.

Figure 29a illustrates the energy spectrum of single-vertex events (pure photoabsorption) when the camera is exposed to a  $^{99m}\text{Tc}$  pointlike source without collimator and triggered by the scintillation signals. The energy spectrum of the single-vertex events includes a 140-keV photoabsorption peak unaccompanied by a fluorescent emission, two approximately



**FIGURE 29** (a) Energy spectrum for single-vertex events for  $^{99m}\text{Tc}$ . (b) Summed energies of three-vertex events for  $^{99m}\text{Tc}$ . (From Bolozdynya *et al.*, 1997b, © 1997 IEEE.)

110-keV overlapping escape peaks with energies of  $E_0 - E_f$ , and xenon fluorescent peaks in the neighborhood of  $E_f = 30$  and 8 keV.

A significant fraction of two-vertex events contains a photoabsorption vertex of the primary photon and a photoabsorption vertex of the fluorescent photon emitted by the xenon atom. Because the energy of the Xe K-shell fluorescent photons is known, a fluorescent-gated energy spectrum can be acquired for two-vertex events using the well-determined energy of the fluorescent photon (Bolozdynya, Chapter 18).

Among three-vertex events, there are the Compton scatter events that can be recognized by the following selection criteria.

1. The total energy deposition for all three vertices should be equal to the energy of the incident gamma rays emitted by the known radioactive source.
2. One of the vertices should have energy deposition of approximately 30 keV (fluorescent photon signature).
3. The energy of the two other vertices should lie in the energy regions allowed by Compton kinematics:

$$\cos \theta_s = 1 - m_e c^2 \frac{E_1}{(E_0 E_2)} \quad (59)$$

where  $\theta_s$  is the angle between the line connecting two conversion points and the direction of incoming gamma ray,  $m_e$  is the mass of the electron,  $E_1$  is the energy deposition at the point of the Compton scattering,  $E_2$  is the energy deposition at the point of the photoabsorption of the scattered gamma ray, and  $E_0 = E_1 + E_2$  is the energy of the incident gamma ray.

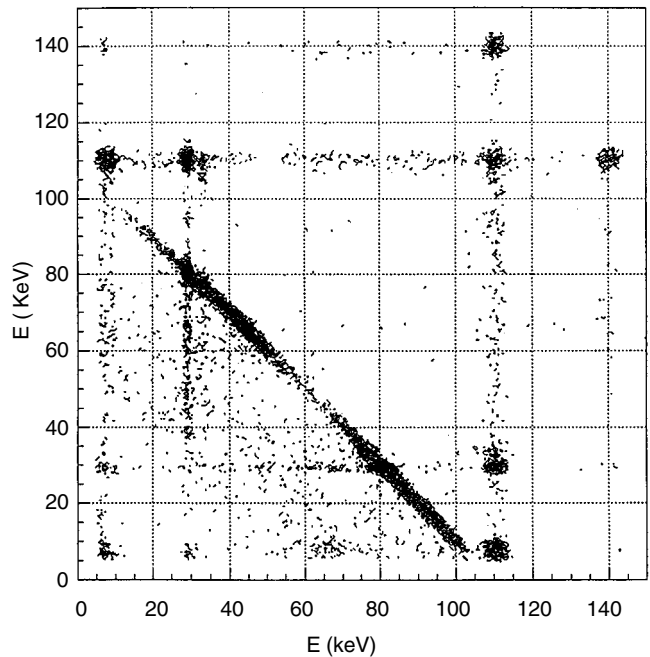


**FIGURE 30** Two-dimensional plot of  $E_a$  versus  $E_b$  for three-vertex events, where  $a$  and  $b$  correspond to the two vertices that are not 30 keV. (From Bolozdynya *et al.*, 1997b, © 1997 IEEE.)

A dual-energy plot of three-vertex events in which one of the vertices is an approximately 30-keV fluorescent event appears in Figure 30. The remaining two vertices,  $a$  and  $b$ , correspond to the recoil electron and photoabsorption of the scattered gamma ray. The photoabsorption is

usually the source of the fluorescent photon. In this plot,  $a$  and  $b$  cannot be uniquely identified with these two events, but events containing a Compton scattering will be localized along the line of  $E_a + E_b = E_0 - E_f$  and form a triangle with the  $E_a$  and  $E_0$  coordinate axes. Three-vertex events, containing nonrelated vertices or combined one- and two-vertex events are localized in spots and along the lines with fixed deposited energy. To demonstrate the effectiveness of the selection criteria, compare the energy spectrum of random single-vertex events in Figure 29a with the spectrum of total energy deposited in the selected three-vertex Compton events Figure 29b. The three-vertex event spectrum has only one dominant peak corresponding to the incident photon energy. The tails correspond to misclassified three-vertex events such as those listed in Figure 28.

Using off-line processing, events from the Compton line in Figure 30 have been selected and Compton scatter angles have been calculated using Eq. (59). The angular distribution in Figure 31 shows an angular resolution of 15° FWHM. This unexpectedly poor angular resolution is largely due to Doppler broadening of the energy of gamma rays scattered from bound electrons in xenon (Ordonez *et al.*, 1997; see also Section IIC1). Note that Doppler broadening has no influence on the total energy deposited in detectors, and this is why the peak of the spectrum in Figure 29b has a width close to the energy resolution of the SDC.

The following procedure was used to evaluate the spatial resolution of the SDC. For each three-vertex event that has been identified as a true Compton event, the 3D parameters of the conic surface determined by the direction of the incoming

gamma ray have been calculated. The half-angle of the cone,  $\theta$  in Figure 27, is calculated using Eq. (25), from the measured energies deposited in the Compton and scattered gamma-ray photoabsorption vertices. The apex of the cone is defined by the measured 3D position of the Compton vertex. The axis of the cone is determined by a line connecting the measured 3D positions of the Compton and photoabsorption vertices. This defines the 3D Compton cone for each selected three-vertex event. Knowing the coordinates of the source located 10.5 cm in front of the center of the grounded electrode, the shortest distance between the reconstructed 3D cone surface and the real position of the source is calculated. The statistical distribution of these distances is 25 mm FWHM, which is a measure of the 3D position accuracy of the SDC in the Compton camera mode (Bolozdynya, Egorov, *et al.*, 1997a). This value, obtained with a 19-channel SDC, compares favorably to the 29-mm resolution calculated for a hypothetical Compton camera with a 1024-channel germanium scatter detector in a comparable configuration (Solomon and Ott, 1988). This clearly demonstrates the advantages of noble gas EL detectors.

This first experience with SDC clarified the high potential of EL noble gas detectors for the development of a practical Compton camera. It is now evident that it is impossible to provide low Doppler broadening of the scattered gamma-ray energy spectrum and high effective photoabsorption after scattering in the same medium. A Compton camera should consist of two separated detectors filled with different substances. Light noble gasses such as He, Ne, and Ar have a dominant Compton cross section for 140-keV gamma rays, exhibit low Doppler broadening for medium-energy gamma rays (see Figures 4 and 9 for Ne), and could be used as the scatter detector. Xenon provides the most effective photoabsorption of gamma rays and is an excellent candidate for the absorption detector.

Further progress in EL imaging cameras is expected with development of a multilayer camera with fiber optic readout and sub-millimeter 3D position resolution—the multilayer electroluminescent camera (MELC; Bolozdynya and Morgunov, 1998). The working gas, gas pressure, number of layers, and total thickness of the detector can be chosen to achieve the required detection efficiency for certain interactions. For example, a 20-cm-thick MELC consisting of 20 layers, each 1 cm deep, and filled with 20-bar Xe will have an 85% photoabsorption efficiency for 140-keV gamma rays. This is comparable to the detection efficiency of 3/8-in-thick NaI(Tl) scintillators usually used in gamma cameras. The MELC filled with 20-bar Ar will be 8% efficient for Compton scattering 140-keV gamma rays and practically transparent for photoabsorbing 140-keV gamma rays. The same efficiency for Compton scattering could be achieved with a 3-mm-thick Si detector. A high-sensitivity Compton camera can be built with a silicon or an argon-filled cylindrical scatter detector surrounded

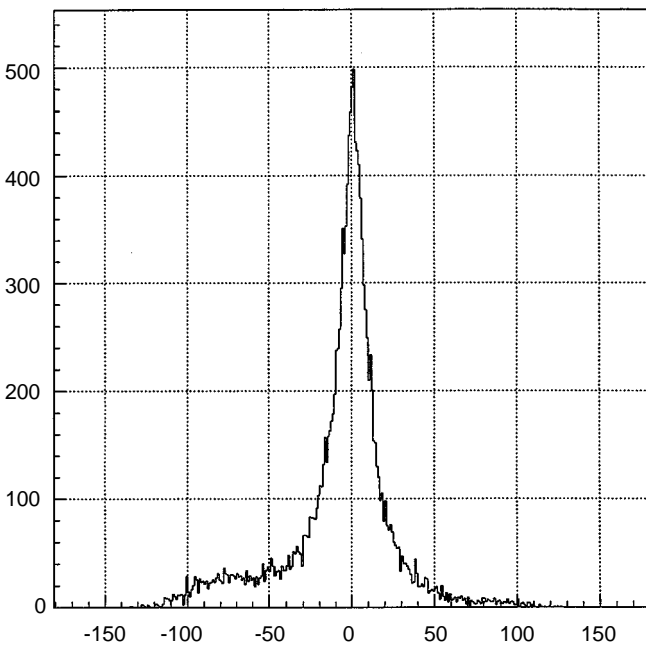


FIGURE 31 Angular resolution of the scintillation drift chamber in Compton camera mode. (© 1997 IEEE.)

by a xenon-filled cylindrical MELC (Bolozdynya, Ordóñez, *et al.*, 1997).

## VI. FUTURE PROSPECTS FOR COMPTON IMAGING

We have seen that the physics underlying Compton scattering fixes the minimum angular uncertainty at 1–2° FWHM at 391 keV and 3–4° at 140 keV for silicon detectors. This corresponds to 1.75–3.5 mm and 5.25–7 mm at 10 cm, respectively, at these two energies. At 140 keV this resolution is further degraded by detector noise. A value of 1 keV FWHM adds an uncertainty between 5 and 5.5° over a scattering angle range of 30–85°. Raw sensitivity gains compared to the corresponding collimator for a single-scatter, double-ring Compton camera, as pictured in Figure 16, range from 300 at 140 keV to 400 at 360 keV for a 16-mm-thick silicon ring, and these figures could double if multiple scatter events were used along with thicker silicon. Using 1.5-mm-thick silicon pad detectors, the ring would contain about 750,000 channels with a current cost estimated to be in the vicinity of \$1.25 million. The gains in raw sensitivity are reduced by a decoding penalty that is object-dependent and that is different depending on whether it is computed using the uniform CR bound or the ideal observer. At 140 keV, considering a 7.5-cm-diameter disk, the penalty is 10 for the ideal observer and 40 for the uniform bound. At 360 keV, the decoding penalty is approximately 1.5–2 according to the bound calculation and 3.25 for the ideal observer. Finally, preliminary noise measurements on a new silicon pad detector give noise values less than 1 keV FWHM. Given this state of affairs, what can we conjecture concerning the future of Compton imaging in nuclear medicine?

Certainly, before one would advocate the general-purpose application of Compton cameras for imaging  $^{99m}\text{Tc}$ , it would be necessary to accomplish the following.

1. Performance predictions based on lower-bound or ideal observer analysis must be met experimentally, and the relationship of these two measures must be better understood.
2. Silicon imaging detectors of some type must be reliably fabricated with 500-eV energy resolution or better at a reasonable price.
3. Technical problems of detector packaging and heat removal for million pixel arrays must be solved.
4. Image reconstruction must be accomplished in acceptable times.
5. Three-dimensional images obtained using these detectors must be of high quality as verified by human observer studies and predicted sensitivity gains must be demonstrated.

It is evident that this is a long-term task requiring substantial research, and for the near term it seems reasonable

to investigate other applications of Compton imaging that would help achieve some of these objectives and also offer more immediate gains with less uncertainty and reduced cost. In the next sections we look at special-purpose imaging tasks and techniques that appear particularly suited to Compton imaging and also discuss some ideas that can only be undertaken using the Compton technique.

### A. Compton Probes

The underlying idea here is to consider imaging tasks in which the imaging instrument can be placed close to the object of interest so that a given angular uncertainty does not translate into an unacceptable spatial uncertainty. Furthermore, these are often situations in which the bulk and mass of a collimator proves a hindrance, and a large field of view can be an asset. A specific example is that of a transrectal prostate probe described by Zhang, Clinthorne *et al.* (2000) and Zhang, Wilderman *et al.* (2000). The probe, illustrated in Figure 32, serves as the first detector of a Compton camera, while the second detector is placed outside of the body, and could easily be a pair of coincidence cameras. Relative locations and orientations of the probe and coincidence cameras may be determined with six-degree-of-freedom motion trackers.

Monte Carlo simulations were run for a Compton imaging system composed of a  $1 \times 1 \times 4 \text{ cm}^3$  stack of silicon detector with  $1\text{-mm}^3$  voxels, and two  $40\text{-cm}^2$  second detectors placed 5 cm above and below a  $40 \text{ cm} \times 40 \text{ cm} \times 20 \text{ cm}$  thick model of a human body. A Y-shaped array of point sources with 5-mm spacing was placed at the location of the prostate 1 cm from the first detector. All effects of scattering, attenuation, detector penetration, and Doppler broadening were included in the simulation. Figure 33 illustrates planar images reconstructed by list mode likelihood for gamma-ray energies of 140, 364, and 511 keV. A 10% energy window on total deposited energy was used. Best performance was obtained at 364 keV for which the resolution was 2 mm FWHM and sensitivity was  $1.2 \times 10^{-3}$ . At 140 keV, resolution degraded to 2.5 mm.

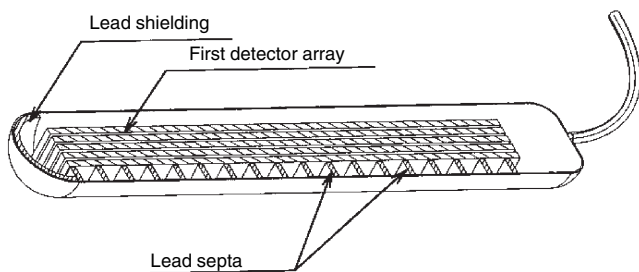


**FIGURE 32** Section view of one possible prostate probe configuration. The first detector is composed of a stack of 1-cm-wide by 4-cm-long silicon pad detectors. Lead septa and shielding can be configured to limit sensitivity to body background.

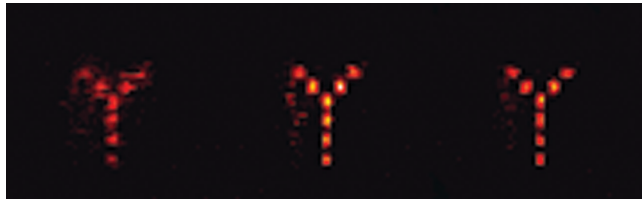


FIGURE 33 Reconstructed images of point source arrays 1 cm from silicon detector: 140, 364, and 511 keV. Point source separation is 5 mm, and each point represents approximately 12,000 photons.

Based on these simulations, it appears that this probe could be used to image  $^{111}\text{In}$ -labeled prostascint to monitor response to therapy or to detect recurrent prostatic disease. Similar small devices might find application in breast imaging (Zhang *et al.*, 2004) or intraoperative tumor localization.

### B. Combined PET-SPECT Imaging

Modern position emission tomography (PET) detectors have four important characteristics that make them almost ideal as second detectors for a Compton camera.

1. They accommodate high count rates, as required by the double ring geometry of Figure 16, and are capable of excellent coincidence timing.
2. Detectors have high stopping power for high-energy gamma rays.
3. Intrinsic spatial resolution can be 2–3 mm or better.
4. Methods have been developed for estimating depth of interaction in PET detectors (see Figure 3 for relevance to Compton imaging).

This suggests that a PET detector could be combined with a silicon ring detector for high-energy SPECT imaging. In addition, such a configuration could serve to augment the PET data by imaging a single annihilation photon when the second one has been absorbed or scattered outside the PET energy window. Furthermore, as described next, annihilation photons that interact with the silicon ring can add a very high resolution-data component to augment the standard PET data. At the moment, this is highly speculative but certainly deserving of future study.

### C. Very High Resolution Animal PET

Another possible application related to Compton imaging and also to PET-SPECT imaging is that of high resolution positron imaging in small animals as described by Park *et al.* (2004). The physical resolution limit for small-diameter PET detector rings is imposed by the positron range in tissue. For  $^{18}\text{F}$ , the range distribution is sharply peaked with a width of 200  $\mu\text{m}$  FWHM. Current animal PET instruments, however, have resolution on the order of 1.5–2 mm FWHM. Although scintillation crystals can be

reduced in size, spatial resolution will remain limited by the greater probability that the photon will scatter in the scintillator rather than be photoabsorbed. The maximum photoelectric efficiencies of BGO, LSO, and NaI at 511 keV are 41%, 33%, and 18%, respectively. The spatial resolution thus becomes limited by the scintillator volume over which the energy is deposited. Park *et al.* (2004) propose using a stack of silicon detectors with 0.5-mm<sup>3</sup> voxels or smaller to encourage Compton scattering followed by escape to a scintillation detector ring. In this manner, the initial interaction point of the photon can be fixed in three dimensions and resolution is limited only by recoil electron range (< 50  $\mu\text{m}$  in Si at the most likely scattering angle of ~35°; < 250  $\mu\text{m}$  at 90°). Figure 34 illustrates one possible configuration for a high resolution positron imager based on this principle.

In this arrangement, there are three basic initial interaction combinations for the two annihilation photons that carry useful information: (1) Si–Si coincidences, (2) Si–scintillator coincidences, and (3) scintillator–scintillator coincidences. The silicon interactions may be split further into photoabsorptions and single or multiple Compton interactions. The highest spatial resolution events will be Si–Si coincidences because both ends of the coincidence line are fixed within the silicon voxel size. In a 4-cm-diameter ring, position uncertainty arising from non-co-linearity of the annihilation photons is less than 100  $\mu\text{m}$ , so this effect becomes important only toward the lower limit on voxel size as determined by recoil electron escape. For Si–scintillator events, resolution will degrade because the scintillator resolution will be 2–3 mm. However, resolution loss is small because the

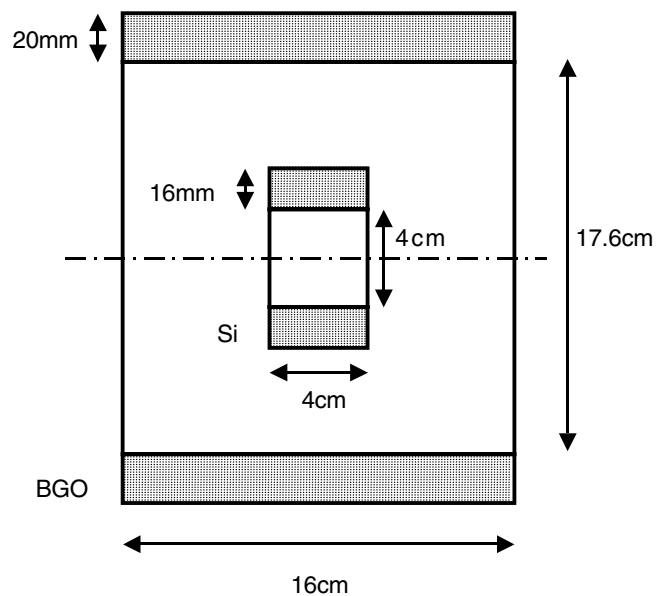


FIGURE 34 Section view of a very high resolution animal PET model used for Monte Carlo simulations. The silicon ring first detector has 0.3  $\times$  0.3  $\times$  1 mm pixels, and the BGO ring is modeled as 3  $\times$  3  $\times$  20 mm discrete elements.

high-resolution silicon interaction is closer to the field of view than the lower-resolution scintillator interaction. If the ratio of distances from the source point to the two detectors is 2:1, the position uncertainty due to scintillator resolution is reduced by a factor of 3. The scintillator–scintillator interactions correspond to the conventional interaction and have the lowest resolution.

Monte Carlo simulations of the system depicted in Figure 34 were used to determine the positron detection efficiency for point sources at different radial positions in the central plane and to generate data sets for a disc phantom consisting of six disks with diameters ranging from 1 mm to 10 mm (Park *et al.*, 2001). Table 3 lists detection efficiencies for three subsets of the many possible combinations of interaction sequences. Single–single corresponds to a single interaction of each photon in the silicon detector. The interaction may be a photoabsorption or a Compton scatter followed by absorption in the BGO detector. In a Single–BGO, one photon has a single interaction in silicon while the other is absorbed by the BGO detector. BGO–BGO corresponds to the conventional PET event with no silicon interaction. The total efficiency is approximately 30%, and this increases significantly if multiple scatter events in silicon are included.

TABLE 3 Efficiency of Very High Resolution Animal PET System of Figure 3<sup>a</sup>

Radial Position (mm)	Detection Efficiency (%)		
	Single-single	Single–BGO	BGO–BGO
0	1.05	8.83	20.84
6	0.96	8.96	20.69
12	1.04	8.94	19.70
18	1.19	9.06	18.17

<sup>a</sup>Calculated for point source in center plane. Only single scattering or absorption interactions in the silicon detector are included. Back-scattered photons from BGO and events without full energy deposition are excluded.

The on-axis geometric resolution for a single–single event with 300-μm pixels is 150 μm FWHM without accounting for positron range, whereas the single–BGO events and BGO–BGO have a corresponding geometric resolution of 400 μm FWHM and 1500 μm FWHM, respectively, with 3-mm BGO elements if one knows which BGO element was struck first. Point source reconstructions by filtered back-projection gave 190 μm, 610 μm, and 1850 μm FWHM for cases when the BGO crystal with the first interaction was assumed to be the one with maximum deposited energy. Figure 35 shows three filtered back-projection images corresponding to the three interaction sequences described. It is important to note that each event defines an actual coincidence chord and there is no conical ambiguity. The image pixels are 156 μm, and a Hamming filter with cutoff of 0.5 pixels was used. The location of the BGO interaction is chosen as the crystal with maximum energy deposition and no correction is made for depth of interaction.

The 1-mm-diameter disk is clearly seen in only the single–single image. There is a hint of it in the Si–BGO image but it would be difficult to distinguish it from noise. Of the 100,000 events, only 450 counts come from this disk. In order to properly combine the data from the three types of interactions, a maximum likelihood algorithm will be required to appropriately weight the different data. It appears that this approach is capable of excellent spatial resolution with very satisfactory sensitivity. Actual implementation, however, will pose a number of challenges in hardware design and real-time data processing in order to identify the correct event sequences.

#### D. Coincidence SPECT

There are a number of radioisotopes that emit two or more cascade gamma rays per decay. These photons are, in effect, emitted simultaneously and depending on the level structure may be correlated in angle. For instance <sup>111</sup>In, with a 2.8-day half-life, emits two photons, 171 keV (90%) and 245 keV (94%); and <sup>130</sup>I, with a 12.4-hr. half-life emits three photons, 731.5 keV (90%), 668.5keV (90%), and 536.1 keV (90%).

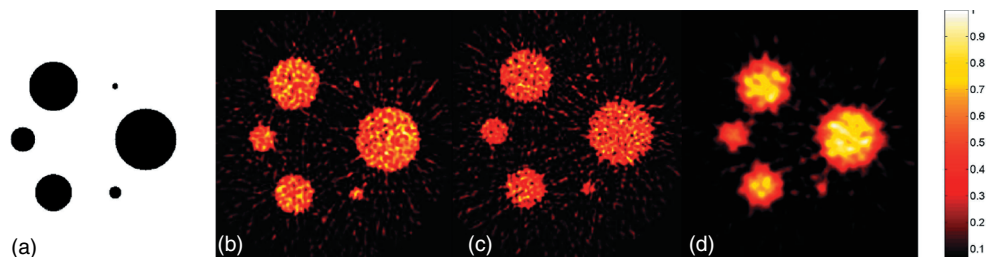
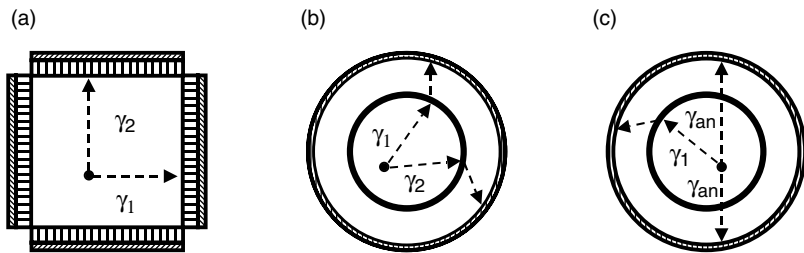


FIGURE 35 Filtered back-projection images of a phantom that consists of six disc sources: 1, 2, 4, 6, 8, and 10 mm in diameter. (a) object. (b) single–single interactions. (c) single–BGO interactions (d) BGO–BGO interactions. Each image contains 100,000 events. (From Park *et al.*, 2001, © 2001 IEEE.)



**FIGURE 36** Three possibilities for imaging radionuclides that simultaneously emit multiple photons. (a) Collimated cameras imaging a pair of cascade gamma rays in coincidence. (b) A double ring Compton camera imaging a pair of cascade gamma rays. (c) A double ring Compton camera imaging a nuclide that emits a positron accompanied by one or more gamma rays in addition to the annihilation photons.

Several authors have pointed out that coincidence imaging of these photons could offer some advantages for nuclear medical imaging (Hart and Rudin, 1977; Boetticher *et al.*, 1980; Liang and Jaszczak, 1990). In addition to cascade gamma rays, Liang and Jaszczak (1990) discuss the case for positron emitters that also emit one or more prompt gamma rays. They list nine such isotopes including  $^{52}\text{Fe}$ , which has an 8.27-hour half-life. Figure 36 illustrates three possibilities for imaging these radionuclides.

In Figure 36a, if  $\gamma_1$  and  $\gamma_2$  are detected in coincidence, the source point can be located in three-dimensions without the need for image reconstruction. The problem is that the efficiency of these collimators is on the order of  $10^{-4}$ , so the coincidence efficiency will be  $10^{-8}$  if there is no angular correlation between the photons. This sensitivity is far too low, even though the image reconstruction step with its attendant noise amplification is eliminated.

In Figure 36b, the collimator is replaced by a double-ring-geometry Compton camera, such as the one illustrated in Figure 16. In this case, a fourfold coincidence restricts the source location to one or two lines in space as defined by the intersection of two cones and the known field of view. Because for single scatter events the Compton camera pictured in Figure 16 can have 300–400 times the sensitivity of a collimator, it might be expected to have a coincidence efficiency approaching  $10^{-3}$ . It would now be necessary to compute the decoding penalty corresponding to the intersection of two cones and compare the image variance to that of an image reconstructed from standard projection data in order to determine how much real sensitivity gain is possible for this scheme.

Finally, Figure 36c illustrates the case for positron emission accompanied by a prompt gamma ray. In this example, the annihilation photons are detected in the second detector, but all the combinations and permutations described for the high-resolution animal PET application are possible. Nevertheless, in Figure 36c the source location is now constrained to lie on the intersection of a cone and line. This reduces to at most two points except for the unlikely case in which the line of the annihilation pair lies along the surface of the cone. This reduction of source location from a line to one or

two points in space represents a large effective gain in SNR. As pointed out in Liang and Jaszczak (1990), it will substantially outperform time-of-flight PET. Although this illustration appears simple, in practice it will be necessary to consider all the possible interaction sequences and be able to uniquely identify which interactions correspond to the annihilation photons and which correspond to the prompt gamma ray. Again, it is necessary to compute the probabilities of the various interaction sequences and determine the magnitude of the effective sensitivity gain. Although some of these radionuclides might well offer improved imaging, a major drawback to their use is the need to develop new radiotracers. Indeed, the image improvements would need to be compelling to spark such a development effort.

### E. Imaging of High Energy Radiotracers

More than 90% of clinical planar and SPECT imaging studies use  $^{99m}\text{Tc}$ . It is inexpensive, is readily available from  $^{99}\text{Mo}$  generators, is easily collimated, and may be imaged by Anger cameras. Furthermore, there is more than a quarter century of radioligand development aimed at addressing a number of specific clinical questions. On the other hand, we have seen that Compton imaging improves rapidly with energies above 140 keV. Furthermore, as energy increases from 140 keV to 360 keV and 511 keV, attenuation and scatter in the patient are reduced and the unscattered flux for 10 cm of water increases by 50% and 70%, respectively. It is thus reasonable to at least consider the applications for high-energy imaging and the possibility of developing new tracers based on high-energy gamma emitters.

Currently, the high-energy single-photon tracers are pretty much limited to the first three entries in Table 4. These isotopes are used both because they have unique chemical properties and also because their longer half-lives are necessary for labeling entities such as antibodies and liposomes that may require days to achieve high specific localization.  $^{131}\text{I}$  is used for radiotherapy, and iodine has a number of properties that make it desirable as a label. It would be extremely valuable to be able to image it at high resolution and good sensitivity at diagnostic doses to evaluate tumor

**TABLE 4** High Energy Radionuclides Used for Single Photon Imaging

Isotope	Half-Life	Percentage	Energy (keV)
<sup>131</sup> I	8.04 days	81	364
		7	636
<sup>111</sup> In	2.83 days	90	171
		94	245
		35	93
<sup>67</sup> Ga	3.26 days	20	184
		16	300
		65	392
<sup>113m</sup> In	1.66 h		

uptake and number and location of tumors, and after therapeutic treatment to evaluate tumor response. <sup>113m</sup>In was used for nuclear medical imaging before the widespread availability of <sup>99m</sup>Tc, and, as mentioned earlier, it is generator-produced from <sup>113</sup>Sn, which has a 119-day half-life. In parts of the world where <sup>99m</sup>Tc is not readily available, <sup>113m</sup>In is still used because the long parent half-life limits the need for generator replacement to approximately two per year. Because both of the indium isotopes can be well imaged with Compton cameras, the possibility exists for developing radiopharmaceuticals for applications requiring either long or short half-lives based on indium. Although the thought of developing a number of new radiolabeled compounds using something other than technetium is certainly daunting, there is active research on using star-burst dendrimers as chelating agents that might enable the coupling of various radioactive metals to tumor-targeting agents (Balogh *et al.*, 2000; Roberts *et al.*, 1990; Kobayashi *et al.*, 1999).

Other applications in which efficient imaging of high energy gamma-emitters would be highly desirable have been raised in discussions with A. B. Brill. He writes:

The imaging of normal physiology remains an important goal, despite the current emphasis nuclear medicine places on the early detection of disease when abnormalities can best be treated successfully. Gamma emitting tracers such as <sup>99m</sup>Tc, <sup>111</sup>In and <sup>123</sup>I are the most important of the gamma emitters in current use. The imaging of beta emitters, including 511 keV positron emitters is limited by the higher dose they deposit in the body, and the use of electronic collimation and short-half life tracers makes PET imaging of <sup>11</sup>C, <sup>15</sup>O, <sup>13</sup>N, and <sup>18</sup>F feasible. Nature has not been kind to us in that many of the naturally occurring elements of interest in the body are long-lived beta/gamma emitters, examples of which are tabulated below [see Table 5]. Much of the effort in the past has been to determine body composition rather than biodistribution for many

**TABLE 5** Isotopes of Interest in the Study of Human Metabolism<sup>a</sup>

Element	Half-Life	Gamma Energy (MeV)	Beta Energy (MeV)
<sup>22</sup> Na	2.6 years	1.27 (99.9)	0.2 (90)
<sup>24</sup> Na	15 h	2.75 (99.9)	0.55 (99.9)
<sup>42</sup> K	12.36 h	1.5 (18)	1.56 (82)
<sup>28</sup> Mg	20.9 h	1.34 (53)	0.16 (94)
<sup>59</sup> Fe	44.5 days	1.29 (43)	0.15 (53)
<sup>58</sup> Co	70.9 days	0.81 (99.5)	0.20 (15)
<sup>65</sup> Zn	244 days	1.1 (51)	0.14 (1.4)
<sup>47</sup> Ca	4.5 days	1.30 (74)	0.24 (81)

<sup>a</sup>Values in parentheses are percentage abundance.

of these essential elements. However, there is good reason to know the distribution of functional bone marrow for example, and <sup>59</sup>Fe (or <sup>52</sup>Fe if it were available) would be very useful in determining regional distribution, rather than sub vertebral distribution. The same could be said for <sup>28</sup>Mg distribution in the heart. Changes in <sup>24</sup>Na distribution associated with anti hypertensive therapy would also be potentially useful. All of these questions could only be studied in man if there were a device without a collimator, such as the Compton Coincidence measurement system, which could image the small amounts of high energy gamma emitters that could be administered.<sup>9</sup>

## VII. DISCUSSION AND SUMMARY

The history of new imaging developments in nuclear medicine demonstrates that there is a long road to general acceptance. SPECT, which has its roots in the early 1960s, required more than a quarter century to attain widespread acceptance, and the development of PET has followed a similar time course. Compton cameras make it possible to image a whole new range of radiotracers with higher resolution and higher sensitivity than collimated cameras. In addition they offer a method for improving the spatial resolution of PET close to the limits fixed by positron range. Further, the method permits investigating methods of direct 3D imaging of radionuclides without an image reconstruction step.

Compton cameras place a high demand on both detector technology and sophisticated methods of data acquisition that permit online sorting and processing of multiple coincidence events. Both of these areas have benefited enormously from

<sup>9</sup>Personal communication from A.B. Brill, M.D., Ph.D., Research Professor Radiology/Physics/BME, Vanderbilt University Medical School, Radiology Dept. MCN R-1302, December 2000.

high-energy physics research and gamma-ray astronomy, and this cross-fertilization will continue to assist the development of Compton imaging devices.

The emphasis in this chapter has been on PIN silicon pad detectors, but position-sensitive silicon drift detectors offer the potential for large-area, low-noise, position-sensitive detectors and have already been suggested for Compton imaging (Kuykens and Audet, 1988). Sizes up to 5 cm × 5 cm have been fabricated on a single wafer, and spatial resolution can be as good as 5 μm (Hall, 1988). At liquid-nitrogen temperatures, noise levels as low as 40 electrons have been demonstrated. Excellent energy resolution has also been obtained by Pullia and co-workers (1988) at Brookhaven for silicon pixel detectors. By bonding individual FET preamplifiers to each pad, they were able to reduce capacitance and obtain energy resolution of 380 eV at room temperature. These developments have the greatest importance for systems intended for use with technetium. Whether devices such as these can be commercially produced is not known, but they would certainly play an important role in establishing Compton camera feasibility. At higher gamma-ray energies, alternative selections such as neon gas detectors or CZT become worthy of consideration.

Projected cost is certainly an important factor, and it is difficult to predict. If one looks at PET, approximately 15 years ago the cost of a PET tomograph was approximately \$4000 a channel. A couple of years ago one could purchase a block detector for approximately \$6500, or approximately \$100 a channel. Some educated guesses for large-scale production of silicon pad detectors place the cost at \$1.50 per channel. Because of the low density of silicon and the limited thickness of undoped wafers, the total cost of a silicon ring, constructed of PIN silicon pad detectors would probably exceed \$1 million. On the other hand, lithium-drifted silicon detectors, which can be much thicker, will reduce the number of channels and might offer a lower-cost alternative. At higher energies, double-sided silicon strip detectors or even neon gas detectors can be considered to reduce cost. It does not seem reasonable to consider cost as a primary stumbling block given the early stage of Compton camera investigations.

It seems fair to conclude that Compton imaging should be viewed as an enabling technology that will permit the investigation of a wide range of new tracers and imaging techniques for application to nuclear medicine. Cost does not appear prohibitive, and the various engineering challenges are stimulating but tractable.

### Acknowledgments

The authors acknowledge the support by U.S. DHHS under NIH grants R01 CA32846 and CA54362 for much of the work described herein. In addition, computing services were provided by the University of Michigan Center for Parallel Computing, which is partially funded by NSF grant CDA-92-14296. We especially wish to credit Jim LeBlanc and Chia-ho Hua for our extensive use of their research results and Scott Wilderman for

the numerous Monte Carlo simulations and image reconstructions. Finally we note that work at the University of Michigan related to Compton cameras involves a long-standing collaboration among the Division of Nuclear Medicine (Les Rogers, Neal Clinthorne, and Dirk Meier), Nuclear Engineering (Glenn Knoll, David Wehe, and Scott Wilderman), EECS (Alfred Hero III and Jeffrey Fessler), CERN (Peter Weilhamer), LEPSI (Wojciech Dulinski), and Integrated Detector Electronics in Oslo, Norway (Einar Nygård), with support of the Norwegian Research Council.

### References

- Alvarez, L. W., Bauber, P. M., Smith, L. H., *et al.* (1973). The liquid xenon Compton telescope: A new technique for gamma-astronomy. Preprint Space Science Laboratory, Ser. 14, Issue 17, University of California, Berkeley.
- Aprile, E., *et al.* (1998). XENA—a liquid xenon Compton telescope for gamma-ray astrophysics in the MeV regime. *Proc. SPIE* **3446**: 88.
- Balogh, L., Tomalia, D. A., and Hagnauer, G. L. (2000). A revolution of nanoscale proportions. *Chem. Inn.* Vol. 30, No. 3. March 19–26.
- Barrett, H. H., Abbey, C. K., and Clarkson, E. (1998). Objective assessment of image quality III: ROC metrics, ideal observers, and likelihood generating functions. *J. Opt. Soc. Am. A* **15**(6): 1520–1535.
- Barrett, H. H., White, T., and Parra L. C. (1997). List-mode likelihood. *J. Opt. Soc. Am. A* **14**(11): 2914–2923.
- Basko, R., Zeng, G. S. L., and Gullberg, G. T. (1998). Application of spherical harmonics to image reconstruction for the compton camera. *Phys. Med. Biol.* **43**(4): 887–894.
- Bhattacharya, D., Dixon, D. D., Kong, V., O'Neill, T. J., White, R. S., Zych, A. D., Ryan, J., McConnell, M., Macri, J., Samimi, J., Akyüz, A., Mahoney, W., and Varnell, L. (1999). A Tracking and Imaging Gamma-Ray Telescope (TIGRE) for energies of 0.3–100 MeV. In “Proceedings of the 26th International Cosmic Ray Conference” (D. Kieda, M. Salamon, and B. Dingus, eds.), Vol. 5, pp. 72–75. American Institute of Physics, Melville, NY.
- Blahut, R. (1987). “Principles and Practice of Information Theory.” Addison-Wesley, Reading, MA.
- Boetticher, H., Helmers, H., *et al.* (1980). Gamma-camera coincidence scintigraphy: Tomography without computerized image reconstruction. In “Medical Radionuclide Imaging,” Vol. 1, pp. 147–148. IAEA, Vienna.
- Bolozdynya, A., Egorov, V., Koutchenkov, A., Safronov, G., Smirnov, G., Medved, S., and Morgunov, V. (1997a). High pressure xenon electronically collimated camera for low energy gamma ray imaging. *IEEE Trans. Nucl. Sci.* **44**(6): 2408–2413.
- Bolozdynya, A., Egorov, V., Koutchenkov, A., Safronov, G., Smirnov, G., Medved, S., and Morgunov, V. (1997b). High pressure xenon self-triggered scintillation drift chamber with 3-D sensitivity in the range of 20–140 keV deposited energy. *Nucl. Instrum. Meth. Phys. Res. A* **385**: 225–238.
- Bolozdynya, A. I., and Morgunov, V. L. (1988). Multilayer electroluminescence camera: Concept and Monte Carlo study. *IEEE Trans. Nucl. Sci.* **45**(3): 1646–1655.
- Bolozdynya, A., Ordonez, C. E., and Chang, W. (1997). A concept of cylindrical Compton camera for SPECT. *1997 IEEE Nucl. Sci. Sym. Conf. Rec.* **2**: 1047–1051.
- Brechner, R., and Singh, M. (1988). Comparison of an electronically collimated system and a mechanical cone-beam system for imaging single photons. *IEEE Trans. Nucl. Sci.* **35**(1): 649–653.
- Brechner, R. R., and Singh, M. (1990). Iterative reconstruction of electronically collimated spect images. *IEEE Trans. Nucl. Sci.* **37**(3): 1328–1332.
- Chelikani, S., Gore, J. C., Zubal, I. G. (2004). Optimizing Compton camera geometries. *Phys. Med. Biol.* **49**(8): 1387–1408.
- Chen, M., and Bolozdynya, A. (1995). Radiation detection and tomography. U.S. Patent 5,665,971, August 8.

- Clinthorne, N. H. (2001). A method for improving the spatial resolution of a Compton camera. U.S. Patent 6,323,492, Nov. 27.
- Clinthorne, N. H., Hua, C.-H., LeBlanc, J. W., Wilderman, S. J., and Rogers, W. L. (1998). Choice of scattering detector for Compton scatter cameras. *J. Nucl. Med. Supp.* **5**: 51P.
- Clinthorne, N. H., Meier, D., Hua, C., Weilhammer, P., Nygård, E., Wilderman, S. J., and Rogers, W. L. (2000). Very high resolution animal PET (abs). *J. Nucl. Med.* **41**(5) (Suppl S): 20P.
- Clinthorne, N. H., Ng, C.-Y., Hua, C.-H., Gormley, J. G., LeBlanc, J. W., Wehe, D. K., Wilderman, S. J., and Rogers, W. L. (1996). Theoretical performance comparison of a Compton scatter aperture and a parallel-hole collimator. *1996 IEEE Nucl. Sci. Sym. and Med. Imag. Conf. Rec.* **2**: 788–792.
- Clinthorne, N. H., Ng, C.-Y., Strobel, J., Hua, C.-H., LeBlanc, J. W., Wilderman, S. J., and Rogers, W. L. (1998). Determining detector requirements for medical imaging applications. *Nucl. Instru. Meth. Phys. Res. A* **409**: 501–507.
- Clinthorne, N. H., Wilderman, S. J., Hua, C., LeBlanc, J. W., and Rogers, W. L. (1998). Choice of scattering detector for Compton scatter cameras. (abs). *J. Nucl. Med.* **39**: 51p.
- Colombetti, L. G., Goodwin, D. A., and Hermanson, R. (1969).  $^{113m}$ In labeled compound for liver and spleen studies. *J. Nucl. Med.* **10**(9): 597–602.
- Cree M. J., and Bones, P. J. (1994). Towards direct reconstruction from a gamma camera based on compton scattering. *IEEE Trans. Med. Imag.* **13**(2): 398–407.
- Dement, G. (1989). Image reconstruction and restoration: overview of common estimation structures and problems. *IEEE Trans. Acous. Sp. Sig. Proc.* **37**(12): 2024–2036.
- Dogan, N. (1993). Multiple Compton scatter camera for gamma-ray imaging. Ph.D. dissertation, University of Michigan.
- Dogan, N., Wehe, D. K., and Akcasu, A. K. (1992). A source reconstruction method for multiple scatter Compton cameras. *IEEE Trans. Nuc. Sci.* **39**(5): 1427–1430.
- Dogan, N., Wehe, D. K., and Knoll, G. F. (1990). Multiple Compton scattering gamma ray imaging camera. *Nucl. Instru. Meth. Phys. Res. A* **299**: 501–506.
- Doria, D., and Singh, M. (1982). Comparison of reconstruction algorithms for an electronically collimated gamma camera. *IEEE Trans. Nucl. Sci.* **29**(1): 447–451.
- Du, Y., He, Z., Knoll, G. F., Wehe, D. K., and Li, W. (2001). Evaluation of a Compton scattering camera using 3-D Position-sensitive CdZnTe detectors. *Nucl. Instru. Meth. Phys. Res. A* **457**: 203–211.
- Durkee, J. W., Antich, P. P., Tsyganov, E. N., Constantinescu, A., Fernando, J. L., Kulkarni, P. V., Smith, B. J., Arbique, G. M., Lewis, M. A., Nguyen, T., Raheja, A., Thambi, G., and Parkey, R. W. (1998). SPECT electronic collimation resolution enhancement using chi square minimization. *Phys. Med. Biol.* **43**: 2949–2974.
- Durkee, J. W., Antich, P. P., Tsyganov, E. N., Constantinescu, A., Kulkarni, P. V., Smith, B., Arbique, G. M., Lewis, M. A., Nguyen, T., Raheja, A., Thambi, G., and Parkey, R. W. (1998). Analytic treatment of resolution precision in electronically collimated SPECT imaging involving multiple-interaction gammas. *Phys. Med. Biol.* **43**: 2975–2990.
- Everett, D. B., Flemming, J. S., Todd, R. W., and Nightingale, J. M. (1976). A gamma-ray camera based on Compton scattering. In “Proceedings 7<sup>th</sup> L. H. Gray Conference,” p. 89. John Wiley, New York.
- Everett, D. B., Todd, R. W., and Nightingale, J. M. (1977). Gamma-radiation imaging system based on the Compton effect. *Proc. IEEE* **124**(11): 995–1000.
- Fessler, J. A., Clinthorne, N. H., and Rogers, W. L. (1993). On complete data spaces for pet reconstruction algorithms. *IEEE Trans. Nuc. Sci.* **40**(4): 1055–1061.
- Fessler, J. A. and Rogers, W. L. (1996). Spatial resolution properties of penalized likelihood image reconstruction methods: Space-invariant tomographs. *IEEE Trans. Imag. Proc.* **5**(9): 1346–1358.
- Fisher, R. A. (1925). “Statistical Methods for Research Workers.” Oliver & Boyd, Edinburgh.
- Fujida, I., and Perez-Mendez, V. (1987). Theoretical considerations of a new electronically collimated gamma camera utilising gas scintillation. *Proc. SPIE* **767**: 84–89.
- Fukunaga, K. (1972). “Introduction to Statistical Pattern Recognition.” Academic Press, New York.
- Gormley, J. E. (1997). Experimental comparison of mechanical and electronic gamma-ray collimation. Ph.D. dissertation, University of Michigan.
- Gormley, J. E., Rogers, W. L., Clinthorne, N. H., Wehe, D. K., and Knoll, G. F. (1997). Experimental comparison of mechanical and electronic gamma-ray collimation. *Nucl. Instru. Meth. Phys. Res. A* **397**: 440–447.
- Hall, G. (1988). Silicon drift chambers. *Nucl. Instru. Meth. Phys. Res. A* **273**: 559–564.
- Hart, H., and Rudin, S. (1977). Three dimensional imaging of multi-millimeter sized cold lesions by focusing collimator coincidence scanning (FCCS). *IEEE Trans. Biomed. Eng.* **24**: 169–177.
- Hebert, T., Leahy, R., and Singh, M. (1987). Maximum likelihood reconstruction for a prototype electronically collimated single photon emission system. *Proc. SPIE* **767**: 77–83.
- Hebert, T., Leahy, R., and Singh, M. (1988). Fast MLE for SPECT using an intermediate polar representation and a stopping criterion. *IEEE Trans. Nucl. Sci.* **35**(1): 615–619.
- Hebert, T., Leahy, R., and Singh, M. (1990). Three-dimensional maximum likelihood reconstruction for an electronically collimated single-photon-emission imaging system. *J. Opt. Soc. Am. A* **7**(7): 1305–1313.
- Hero, A. O. (1992). A Cramèr-Rao type lower bound for essentially unbiased parameter estimation. Technical Report 890, M.I.T. Lincoln Laboratory, Lexington, MA, DYIC AD-A246666.
- Hero, A. O., Fessler, J. A., and Usman, M. (1996). Exploring estimator bias-variance tradeoffs using the uniform cr bound. *IEEE Trans. Sig. Proc.* **44**(8): 2026–2041.
- Hua, C.-H. (2000). Compton imaging system development and performance assessment. Ph.D. dissertation, University of Michigan.
- Hua, C.-H., Clinthorne, N. H., Wilderman, S. J., LeBlanc, J. W., and Rogers, W. L. (1999). Quantitative evaluation of information loss for Compton cameras. *IEEE Trans. Nucl. Sci.* **46**(3): 587–593.
- Ichihara, T. (1987). Ring type single photon emission CT imaging device. U.S. Patent 4,639,599, Jan. 27.
- Kamae, T., Enomoto, R., and Hanada, N. (1987). A new method to measure energy, direction, and polarization of gamma-rays. *Nucl. Instru. Meth. Phys. Res. A* **260**: 254–257.
- Kamae, T., and Hanada, N. (1988). Prototype design of multiple Compton camera. *IEEE Trans. Nucl. Sci.* **35**(1): 352–355.
- Keener, J. P. (1988). “Principles of Applied Mathematics: Transformation and Approximation.” Addison-Wesley, New York.
- Klein, O., and Nishina, Y. (1929). Über de Streung von Strahlung durch freie Elektronen nach derneuen relativistischen Quantendynamik von Dirac. *Z. Physik.* **52**: 853.
- Knoll, G. F. (2000). “Radiation Detection and Measurement,” 3rd ed., chap. 11. John Wiley & Sons, New York.
- Kobayashi, H., Wu, C., Kim, M.-K., Paik, C. H., Carrasquillo, J. A., and Brechbiel, M. W. (1999). Evaluation of the *in vivo* biodistribution of indium-111 and yttrium-88 labeled dendrimer-1B4M-DTPA and its conjugation with Anti-Tac monoclonal antibody. *Bioconjugate Chem.* **10**: 103–111.
- Kroeger, R. A., Johnson, W. N., Kurfess, J. D., Phlips, B. F., Luke, P. N., Momayez, M., and Warburton, W. K. (1999). Position Sensitive Germanium Detectors for the Advanced Compton Telescope. In “AIP Conference Proceedings of the 5th Compton Symposium,” (McConnell, M. L., and Ryan, J. M., eds.), Vol. 510, pp. 794–798. American Institute of Physics, Melville, NY.
- Kroeger, R. A., Johnson, W. N., Kurfess, J. D., Phlips, B. F., Wulf, E. A. (2000). Gamma ray energy measurement using the multiple Compton technique. *2000 IEEE Nucl. Sci. Symp. Med. Imag. Conf. Rec.* **1**: 8-7–8-11.

- Kuykens, H. J. P., and Audet, S. A. (1988). A 3×3 silicon drift chamber array for application in an electronic collimator. *Nucl. Instru. Meth. Phys. Res. A* **273**: 570–574.
- LeBlanc, J. W. (1999). A Compton camera for low energy gamma-ray imaging in nuclear medicine applications. Ph.D. dissertation, University of Michigan.
- LeBlanc, J. W., Bai, X., Clinthorne, N. H., Hua, C., Meier, D., Rogers, W. L., Wehe, D. K., Weilhammer, P., and Wilderman, S. J. (1999). 99mTc imaging performance of the C-SPRINT Compton camera. *1999 IEEE Nucl. Sci. Sym. Med. Imag. Conf. Rec.* **1**: 545–552.
- LeBlanc, J. W., Clinthorne, N. H., Hua, C.-H., Nygård, E., Rogers, W. L. (1998). C-SPRINT: A prototype Compton camera system for low energy gamma-ray imaging. *IEEE Trans. Nucl. Sci.* **45**(3): 943–949.
- LeBlanc, J. W., Clinthorne, N. H., Hua, C., Rogers, W. L., Wehe, D. K., and Wilderman, S. J. (1999). A Compton camera for nuclear medicine applications using <sup>113m</sup>In. *Nucl. Instru. Meth. Phys. Res. A* **422**: 735–739.
- Lecomte, R., Schmitt, D., and Lamoureux, G. (1984). Geometry study of a high resolution PET detection system using small detectors. *IEEE Trans. Nucl. Sci.* **31**(1): 556–561.
- Liang, Z., and Jaszcak, R. (1990). Comparisons of multiple photon imaging techniques. *IEEE Trans. Nucl. Sci.* **37**(3): 1282–1292.
- Martin, J. B. (1994). A compton scatter camera for SPECT imaging of 0.5 to 3.0 MeV gamma-rays. Ph.D. dissertation, University of Michigan.
- Martin, J. B., Dogan, N., Gormley, J. E., Knoll, G. F., O'Donnell, M., and Wehe, D. K. (1994). Imaging multi-energy gamma-ray fields with a Compton scatter camera. *IEEE Trans. Nucl. Sci.* **41**(4): 1019–1025.
- Martin, J. B., Knoll, G. F., Wehe, D. K., Dogan, N., Jordanov, V., Petrick, N., and Singh, M. (1993). A ring Compton scatter camera for imaging medium energy gamma-rays. *IEEE Trans. Nucl. Sci.* **40**(4): 972–978.
- McMaster, W. H. (1961). Matrix representation of polarization. *Rev. Mod. Phys.* **33**(1): 8–28.
- Meier, D., Czermak, A., Jalocha, P., Sowicki, B., Kowal, M., Dulinski, W., Mæhlum, G., Nygård, E., Yoshioka, K., Fuster, J., Lacasta, C., Mikuz, M., Roe, S., Weilhammer, P., Hua, C.-H., Park, S.-J., Wilderman, S. J., Zhang, L., Clinthorne, N. H., and Rogers, W. L. (2000). Silicon detector for a Compton camera in nuclear medical imaging. *2000 IEEE Nucl. Sci. Sym. Med. Imag. Conf. Rec.*
- Namito, Y., Ban, S., and Hirayama, H. (1994). Implementation of the Doppler Broadening of a Compton-scattered photon into the EGS4 code. *Nucl. Instru. Meth. Phys. Res. A* **349**: 489–494.
- Namito, Y., Ban, S., and Hirayama, H. (1995). LSCAT: Low-energy photon scattering expansion for the EGS4 code. KEK International 95–10, August, Ibaraki-ken, Japan.
- Namito, Y., Ban, S., and Hirayama, H. (2000). LSCAT: Low-energy photon-scattering expansion for the EGS4 code (inclusion of electron impact ionization). KEK International 2000–4, May, Ibaraki-ken, Japan.
- Natterer, F. (1986). “The Mathematics of Computerized Tomography.” Wiley, New York.
- Naylor, A. W., and Sell, G. R. (1982). “Linear Operator Theory in Engineering and Science, volume 40 of Applied Mathematical Sciences.” Springer-Verlag, New York.
- O’Mara, R. E., Subramanian, McAfee, J. G., and Burgher, C. L. (1969). Comparison of <sup>113m</sup>In and other short-lived agents for cerebral scanning. *J. Nucl. Med.* **10**(1): 18–27.
- O’Neill, T. J., Akyuz, A., Bhattacharya, D., Case, G. L., Dixon, D., Samimi, J., Tumer, O. T., White, R. S., and Zych, A. D. (1996). Tracking, imaging and polarimeter properties of the TIGRE instrument. *Astron. Astrophys. Supp. Series* **120**(4): C661–4.
- Ordonez, C. E., Bolozdynya, A., and Chang, W. (1997). Doppler broadening of energy spectra in Compton scatter cameras. *1997 IEEE Nucl. Sci. Sym. Med. Imag. Conf. Rec.* **2**: 1361–1365.
- Ordonez, C. E., Chang, W., and Bolozdynya, A. (1999). Angular uncertainties due to geometry and spatial resolution in Compton cameras. *IEEE Trans. Nucl. Sci.* **46**(4): 1142–1147.
- Park, S., Han, L., Wilderman, S. J., Sukovic, P., Czermak, A., Jalocha, B., Kowal, M., Dulinski, W., Maehlum, G., Nygård, E., Yoshioka, K., Fuster, J., Lacasta, C., Mikuz, M., Roe, S., Weilhammer, P., Meier, D., Rogers, W. L., and Clinthorne, N. H. (2001). Experimental setup for a very high resolution animal PET based on solidstate detector. *2001 IEEE Nucl. Sci. Sym. Med. Imag. Conf. Rec.*
- Park, S. J., Rogers, W. L., and Clinthorne, N. H. (2004). Design of a very high resolution small animal PET based on the Compton PET concept. *IEEE Trans. Med. Imaging* (Submitted).
- Park, S., Rogers, W. L., Wilderman, S. J., Sukovic, P., Han, L., Meier, D., Nygård, E., Weilhammer, P., and Clinthorne, N. H. (2001). Design of a very high resolution animal PET (abs). *J. Nucl. Med. Suppl.* **42**: 102.
- Parra, L. C. (2000). Reconstruction of cone-beam projections from compton scattered data. *IEEE Trans. Nucl. Sci.* **47**(4): 1543–1550.
- Pehl, R. H., Madden, N. W., Landis, D. A., Malone, D. F., Cork, C. P. (1985). Cryostat and electronic development associated with multi-detector spectrometer system. *IEEE Trans. Nucl. Sci.* **32**(1): 22–28.
- Pinkau, K. (1960). Die messung solarer und atmosphärischer neutonen. *Z. Naturforschung A* **21a**(12): 2100–.
- Pullia, A., Kraner, H. W., Siddons, D. P., Furenlid, L. R., and Bertuccio, G. (1995). Silicon detector system for high rate EXAFS applications. *IEEE Trans. Nucl. Sci.* **42**: 585–589.
- Qi, J., and Huesman, R. H. (2001). Theoretical study of lesion detectability of MAP reconstruction using computer observers. *IEEE Trans. Med. Imag.* **20**(8): 815–822.
- Rao, C. R. and Toutenburg, H. (1999). “Linear Models: Least Squares and Alternatives” Second Edition. Springer Series in Statistics. Springer, New York.
- Roberts, J. C., Adams, Y. E., Tomalia, D., Mercer-Smith, J. A., and Lavalee, D. K. (1990). Using starburst dendrimers as linker molecules to radiolabel antibodies. *Bioconjugate Chem.* **2**: 305–308.
- Rogers, W. L., and Ackermann, R. J. (1992). SPECT instrumentation. *Am. J. Physiol. Imag.* **7**(3/4): 105–120.
- Rogers, W. L., Clinthorne N. H., Stamos J., Koral K. F., Mayans R., Keyes J. W., Jr, Williams, J. J. (1982). SPRINT: A stationary detector single photon ring tomograph for brain imaging. *IEEE Trans. Med. Imag.* **MI-1**: 63–68.
- Rohe, R. C., Sharfi, M. M., Kecevar, K. A., Valentine, J. D., and Bonnerave, C. (1997). Spatially-variant backprojection point kernel function of an energy-subtraction compton scatter camera for medical imaging. *IEEE Trans. Nucl. Sci.* **44**(6): 2477–2482.
- Rohe, R., and Valentine, J. D. (1995). A novel Compton scatter camera design for *in-vivo* medical imaging of radiopharmaceuticals. *1995 IEEE Nucl. Sci. Sym. Med. Imag. Conf. Rec.* **3**: 1579–1583.
- Rohe, R. C., and Valentine, J. D. (1996). Compton camera for *in vivo* medical imaging of radiopharmaceuticals. U.S. Patent 5,567,944, Oct. 22.
- Sansen, W. M., and Chang, Z. Y. (1990). Limits of low electron noise performance of detector readout front ends in CMOS technology. *IEEE Trans. Circuits Sys.* **37**(11): 1375–1382.
- Sauve, A. C., Hero, A. O., Rogers, W. L., Wilderman, S. J., and Clinthorne. N. H. (1999). 3d image reconstruction for a compton spect camera model. *IEEE Trans. Nucl. Sci.* **46**(6): 2075–2084.
- Shepp, L. A. and Vardi, Y. (1982). Maximum likelihood reconstruction for emission tomography. *IEEE Trans. Med. Imag.* **1**(2): 113–122.
- Schönfelder, V., Diehl, R., Lichti, G. G., Steinle, H., Swanenburg, B. N., Deerenberg, A. J. M., Aarts, H., Lockwood, J., Webber, W., Macri, J., Ryan, J., Simpson, G., Taylor, B. G., Bennett, K., and Snelling, M. (1984). The imaging COMPTEL telescope, COMPTEL on the gamma ray observatory. *IEEE Trans. Nucl. Sci.* **31**(1): 766–770.
- Schönfelder, V., Hirner, A., and Schneider, K. (1973). A telescope for soft gamma ray astronomy. *Nucl. Instru. Meth. Phys. Res.* **107**: 385.
- Schopper, F., Andritschke, R., Kanbach, G., Kemmer, J., Lampert, M.-O., Lechner, P., Richter, R., Rohr, P., Schönfelder, V., Strüder, L., and

- Zoglauer, A. (2000). Development of silicon strip detectors for a medium energy gamma-ray telescope. *IEEE Nucl. Sci. Symp. Med. Imag. Conf. Rec.* **1**: 3-122-3-126.
- Schopper F., Andritschke R., Shaw H., Nefzger C., Zoglauer A., and Schonfelder V. (2000). CsI calorimeter with 3-D position resolution. *Nucl. Instru. Meth. Phys. Res. A* **442**: 394–399.
- Singh, M., and Doria, D. (1983). An electronically collimated gamma camera for single photon emission computed tomography. part II: Image reconstruction and preliminary experimental measurements. *Medical Physics*, **10**(4): 428–35.
- Singh, M. (1983). An electronically collimated gamma camera for single photon computed tomography. Part I: Theoretical considerations and design criteria. *Med. Phys.* **10**(4): 421–427.
- Singh, M., Brechner, R. R., and Horne, C. (1986). Single photon imaging at high energies with electronic collimation. *Proc. SPIE* **671**: 184–188.
- Singh, M., and Doria, D. (1981). Computer simulation of image reconstruction with a new electronically collimated gamma tomography system. *Proc. SPIE* **273**: 192–200.
- Singh, M., and Doria, D. (1983). An electronically collimated gamma camera for single photon emission computed tomography. Part II: Image reconstruction and preliminary experimental measurements. *Med. Phys.* **10**(4): 428–435.
- Singh, M., and Doria, D. (1985). Single photon imaging with electronic collimation. *IEEE Trans. Nucl. Sci.* **32**(1): 843–847.
- Singh, M., Leahy, R., Brechner, R., and Hebert, T. (1988). Noise propagation in electronically collimated single photon imaging. *IEEE Trans. Nucl. Sci.* **35**(1): 772–777.
- Solomon, C. J., and Ott, R. J. (1988). Gamma ray imaging with silicon detectors—a Compton camera for radionuclide imaging in medicine. *Nucl. Instru. Meth. Phys. Res. A* **273**: 787–792.
- Stayman, J. W., and Fessler, J. A. (2002). Compensation for nonuniform resolution using penalized-likelihood reconstruction in space-variant imaging systems. *IEEE Trans. Med. Imag.* Submitted.
- Todd, R. W. (1975). Methods and apparatus for determining the spatial distribution of a radioactive material. U.S. Patent 3,876,882, April.
- Todd, R. W., Nightingale, J. M., and Everett, D. B. (1974). A proposed  $\gamma$ -camera. *Nature* **25**: 132.
- Valentine, J. D., Bonnerave, C., and Rohe, R. C. (1996). Energy-subtraction Compton scatter camera design considerations: A Monte Carlo study of timing and energy resolution effects. *1996 IEEE Nucl. Sci. Sym. Conf. Rec.* **2**: 1039–1043.
- Weilhamer, P., Nygård, E., Dulinski, W., Czermak, A., Djama, F., Gadomski, S., Roe, S., Rudge, A., Schopper, F., and Strobel, J. (1996). Si pad detectors. *Nucl. Instru. Meth. Phys. Res. A* **383**: 89–97.
- White, R. S. (1968). An experiment to measure neutrons from the sun *Bull. Am. Phys. Soc. Ser. II* **13**(4): 714.
- Wilderman, S. J. (1990). Vectorized algorithms for Monte Carlo simulation of kilovolt electron and photon transport (electron transport). Ph.D. dissertation, University of Michigan. Available at <http://www.lib.uni.com/cr/umich/fullcit?p9116324>.
- Wilderman, S. J., Clinthorne, N. H., Fessler, J. A., and Rogers, W. L. (1999). List-mode maximum likelihood reconstruction of compton scatter camera images in nuclear medicine. *IEEE Nucl. Sci. Sym. Med. Imag. Conf.* **3**: 1716–1720.
- Wilderman, S. J., Fessler, J. A., Clinthorne, N. H., and Rogers, W. L. (2001). Improved modeling of system response in list mode em reconstruction of compton scatter camera images. *IEEE Trans. Nucl. Sci.* **48**(1): 111–116.
- Winkler, C., Bennett, K., Bloemen, H., Collmar, W., Connors, A., Diehl, R., van-Dordrecht, A., den-Herder, J. W., Hermsen, W., Kippen, M., Kuiper, L., Lichti, G., Lockwood, J., McConnell, M., Morris, D., Ryan, J., Schonfelder, V., Stacy, G., Steinle, H., Strong, A., Swanenburg, B., Taylor, B. G., Varendorff, M., and de-Vries, C. (1992). The gamma-ray burst of 3 May 1991 observed by COMPTEL on board GRO. *Astron. Astrophys.* **255**(1–2): L9–12.
- Wulf, E. A., Johnson, W. N., Kroeger, R. A., Kurfess, J. D., and Philips, B. F. (2002). Germanium strip detector Compton telescope using three dimensional readout. *IEEE Nucl. Sci. Sym. Med. Imag. Conf. Rec.* **1**: 57–61.
- Zhang, L., Clinthorne, N. H., Wilderman, S. J., Hua, C., Kragh, T. J., and Rogers, W. L. (2000). An innovative high efficiency and high resolution probe for prostate imaging (abs). *J. Nucl. Med.* **41**(5) (Suppl. S): 18P.
- Zhang, L., Rogers, W. L., and Clinthorne, N. H. (2004). Potential of a Compton camera for high performance scintimammography. *Phys. Med. Biol.* **49**: 617–638.
- Zhang, L., Wilderman, S. J., Clinthorne, N. H., and Rogers, W. L. (2000). An anthropomorphic phantom integrated EGS4 Monte Carlo code and its application in Compton probe. *Proc. 2000 IEEE Nucl. Sci. Sym. Med. Imag. Conf.* **3**: 119–122.